NOVEL ACTIVE MAGNETIC BEARING CONTROL FOR A

HIGH-SPEED FLYWHEEL

A Thesis

by

COLBY FOSTER LEWALLEN

Submitted to the Office of Graduate and Professional Studies of
Texas A&M University
in partial fulfillment of the requirement for the degree of

MASTER OF SCIENCE

Chair of Committee,	C. Steve Suh
Committee Members,	Bruce Tai
	Jyhwen Wang
Head of Department,	Andreas Polycarpou

August 2016

Major Subject: Mechanical Engineering

ABSTRACT

Flywheel energy storage (FES) systems have recently gained momentum in the energy storage industry as a viable alternative to conventional lithium-ion and lead-acid batteries because they have superior energy density, faster charge rates, lack harmful chemicals, and are easy to repair. Contemporary FES research is focused on increasing the maximum operating speed of the rotor and reducing the power consumed by the active magnetic bearings. Therefore, the objective of this research was to implement a novel nonlinear controller called 'wavelet-based time-frequency control' (WFXLMS) in a computer simulation of a FES system with five degrees-of-freedom and compare its dynamic stability and active power consumption with a proportional-integral-derivative (PID) and fuzzy-logic controller scheme. Specifically, all three controllers were applied to a FES system operating at a high rate of speed and the amplitude of vibration, rate of convergence, and current draw were compared.

The results show that the ideal choice for a FES system is the WFXLMS controller. While it did draw the largest maximum current of any system, it used significantly less (half of PID and a quarter of fuzzy-logic's) steady state current. This would drastically improve the energy storage duration; one of the main functions of a FES system. The WFXLMS controller is also the ideal system for higher operating speeds because of the system's stability in the frequency domain. Comparing the average displacements shows that the WFXLMS controller had the largest average displacement (particularly in the z-axis), but the WFXLMS controller only used a fraction of the available clearance gap.

If the FES system was used in an environment like space or a wind-farm where external excitations are limited, the WFXLMS controller is the clear choice. However, if external excitations are a real concern, the PID and fuzzy-logic controllers demonstrated a much quicker reaction time and would be the better choice.

To my family, friends, and mentors.

TABLE OF CONTENTS

LIST OF FIGURES

LIST OF TABLES

1   INTRODUCTION

1.1   Kinetic Energy Storage Using Flywheel Devices

The use of devices that are capable of storing kinetic energy has been around for centuries in tools like the pottery wheel and the spinning wheel, but their use in larger scale systems and their interest in the research community were relatively insignificant until recently. Contemporary, high-performance flywheel energy storage (FES) research began to gain momentum in the engineering research community in the 1960s as subsequent advances in the material science and controller design fields provided FES systems with crucial advantages over standard, electrochemical batteries [1, 2]. Applications for these modern FES systems include: energy storage and attitude control for orbiting satellites [1], stabilizing energy production in wind farms by acting as an uninterrupted power supply (UPS) [2], batteries in electric automobiles [2], and alternators that deliver pulsed power to weapons [3].

In contrast to electrochemical batteries – which store energy in the form of chemical potential – FES relies on the use of kinetic energy. The kinetic energy (T) stored in a FES system is governed by equation 1.1 below.

$$T = \frac{1}{2}I\omega^2 \tag{1.1}$$

This equation demonstrates that angular velocity (ω) and the mass moment of inertia

(*I*) of the flywheel rotor both impact the total energy stored in the FES system. Since angular velocity is squared, increasing angular velocity has a larger impact on total energy stored than mass moment of inertia. The maximum angular velocity of a FES system depends, primarily, on the efficacy of the implemented controller scheme and is covered in more depth in the next chapter.

Since the kinetic energy of a FES system is proportional to the mass moment of inertia of the rotor, conventional systems increase the inertia - increasing the total energy storage capacity for a particular operating speed - by increasing the radius of the flywheel. Assuming that the flywheel is made of a single material with uniform density (ρ) and a constant inner and outer radius (r_i and r_o, respectively), the kinetic energy of the flywheel rotor can be rewritten using equation 1.2.

$$T = \frac{1}{4}\rho\pi h(r_o^4 - r_i^4)\omega^2 \tag{1.2}$$

This equation shows that while kinetic energy increases quadratically with angular velocity, the radius of the rotor plays an even more significant role. However, as the rotor radius increases, the velocity of the rotor at the outer radius experiences greater internal stresses. Accordingly, only materials with exceptionally high hoop strength can be used in FES systems with large angular velocities and large outer diameters. Considering a thin-rim rotor as an approximation, it can be shown that the product of maximum rotor radius and angular velocity is dependent on the strength of a material in the hoop direction ($S_{\theta\theta}$) and the density of the material as shown in equation 1.3 [2].

$$\omega_{max} = \frac{1}{r_{o,max}}\sqrt{\frac{S_{\theta\theta}}{\rho}} \tag{1.3}$$

Because the materials selected for flywheel rotors need to have a high hoop strength and a low density in order to maximize kinetic energy storage, a flywheel rotor is typically made of fiber-reinforced polymer composite that is filament-wound in the circumferential direction. Equation 1.3 also demonstrates that the maximum speed of the rotor is inversely proportional to the outer radius of the flywheel. Therefore, decreasing the outer radius of the flywheel increases the maximum possible operating speeds while staying within the rotor material's physical limitations. In conclusion, due to the material properties of available materials, the ideal way to increase the energy storage capacity of a FES system is to maintain or reduce the outer radius of the rotor and increase the operating speed.

1.2   Contemporary FES Configuration

Current FES systems employ the use of a flywheel rotor to store angular momentum by rotating at speeds up to 60,000-100,000 rpm depending on size and controller efficacy [2, 4]. This rotor is accelerated and decelerated by an electrical device (most commonly a motor/generator hybrid unit) that provides and withdraws the kinetic energy from the system. A simplified model of a FES system that demonstrates the flow of energy is shown in Figure 1.1 [2].

Since FES systems target large angular velocities, vacuum chambers and active magnetic bearings (AMB) are used to minimize losses from drag and bearing friction, respec-
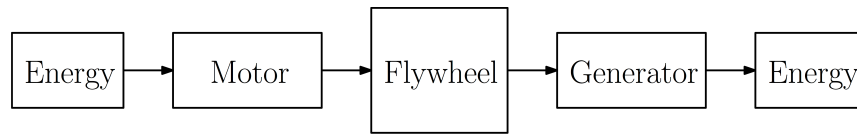
Figure 1.1: Simplified model of power flow through a FES system.

tively. Consequently, a lack of physical contact between the rotor and the FES housing means that the AMBs have to be actively controlled. Specifically, each electromagnet passes current through a coil of wire that generates a flux field that pulls the rotor towards it. Since the electromagnet surrounds the rotor, this flux can be adapted around the rotor to change the direction and magnitude of the net force applied to the rotor. A typical configuration for a commercially available FES system is shown in Figure 1.2 [2].
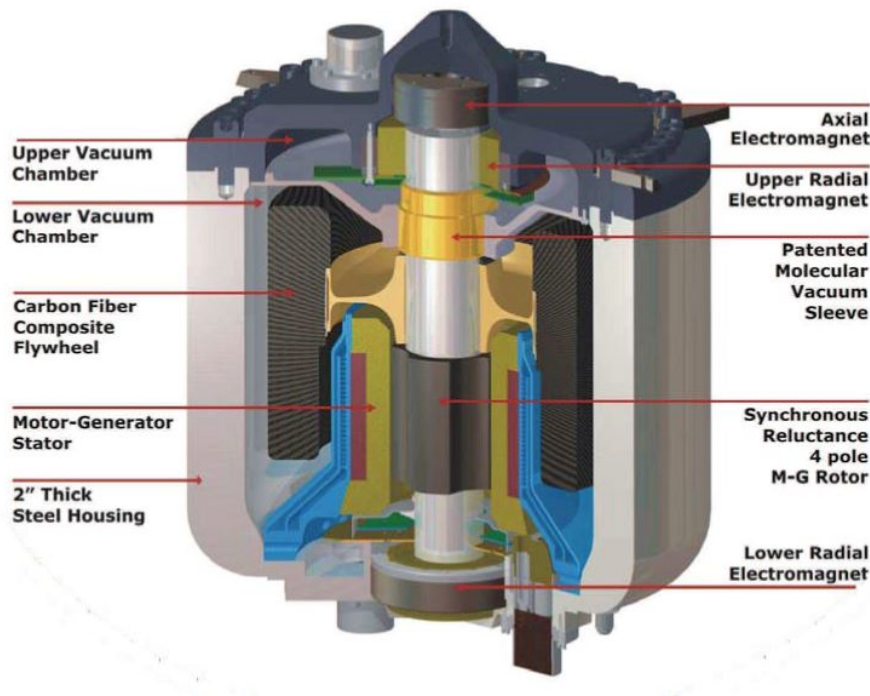
Figure 1.2: Example of a commercially available FES system [2].

To ensure that the flywheel rotor remains suspended in space, at least 3 magnetic

bearings are required. The radial position is controlled by AMBs (referred to as the upper and lower radial electromagnet in Figure 1.2) and the vertical position is controlled by a thrust bearing (referred to as an axial electromagnet in Figure 1.2). Sometimes, the thrust and radial position is controlled with unique, hybrid bearings, but the layout shown in Figure 1.2 is the most common.

1.3   Comparison of FES Systems with Existing Electrochemical Batteries

It is important to highlight the advantages and disadvantages for FES systems compared to common lead-acid and lithium-ion electrochemical batteries to show why continued FES research is propitious for the energy sector. One of the most cited advantages of FES systems is its excellent energy storage capacity per unit mass (often referred to as energy density). Most FES systems can achieve specific energies of at least 100 Wh/kg while current, state-of-the-art FES systems can reach values of 200 Wh/kg. In comparison, a typical lead-acid battery has a specific energy of 30 Wh/kg, and lithium-ion can reach a value of 100 Wh/kg [2].

A theoretical double in energy density for FES systems means that companies can supply similar power while, simultaneously, halving the weight of the existing battery. This is particularly useful when weight is a major concern. For example, replacing current electrochemical batteries in satellites with FES systems will reduce the amount of fuel - thus the cost - required for getting it into orbit. In this particular case, the introduction of a few FES systems in a satellite provides the added benefit of controlling the attitude

by assembling 5 double-gimbaled systems in 'planar' arrangement [1]. Furthermore, the rapidly growing electric vehicle market is developing vehicles that are hindered by the relative weight of the chemical battery to the car. This problem is quickly rectified by replacing the chemical battery with a FES system of similar energy capacity. In fact, there are places where FES system powered vehicles are already in operation. One such example is the 'Gyrobus' that was developed by the Maschinenfabrik Oerlikon in Switzerland in the 1930s [2].

In addition to the excellent energy density, FES systems have a smaller environmental impact than electrochemical batteries because they lack any harmful chemicals, they minimize heat dissipation when charging and discharging, and they can operate over a much larger temperature range of -250°C to 450°C (subject to system materials and machining tolerances) [5].

In contrast, one of the primary disadvantages of FES systems is their cost. FES systems can cost up to 8 times more than the typical cost of a lead-acid battery system. However, this disadvantage is offset by the much longer service life which can reach up to 8 times longer than the same lead-acid batteries [2]. FES systems can operate longer than electro-chemical batteries because they have practically infinite charge and discharge cycles while electrochemical batteries see a decrease in storage capacity as the number of charge and discharge cycles increases. Cost consideration for these FES systems must also include the energy recovery efficiency. FES systems are 90-95% efficient whereas lead-acid batteries have energy recovery efficiencies in the range of 60-70% [2].

1.4 Literature Review

The goal of any FES system is to maximize the stored energy while minimizing both the active power consumption and maintenance issues. The important design issues for AMBs within a FES system include: the bearing load capacity (the attractive forces of the bearings), the bearing stiffness, the maximum flux density in the air gap, the maximum bearing (coil) operating temperature, geometric and gyroscopic coupling forces, and eddy current/hysteresis loss [5, 6]. Additionally, the dynamics of the flywheel rotor are inherently nonlinear because of force coupling effects along non parallel axis and the non-linearities of electromagnetic fields.

The motion of the rotor that is generated by an eccentric force creates a geometric coupling of the magnetic forces acting on the rotor. The geometric coupling force can be modeled by an equation, but it relies on a parameter that can only be determined experimentally or using a two-dimensional finite element method [6]. For an AMB, this gemotric coupling force can lead to Hopf bifurcation to periodic solutions as the speed changes through critical values [6]. This bifurcation behavior can lead to distinctly different solutions between a linear and a nonlinear model. The stability of a system demonstrating Hopf bifurcation (coexisting solutions) seems to be mainly dependent on the amplitude of excitation, and the 'critical' amplitude for bifurcation seems to depend mainly on the following parameters: stiffness (proportional feedback), damping (derivative feedback), eccentricity, and the geometric coupling parameter [7].

To demonstrate the nonlinearities in the electromagnetic field generated by an AMB,

consider the simplified configuration shown in Figure 1.3.
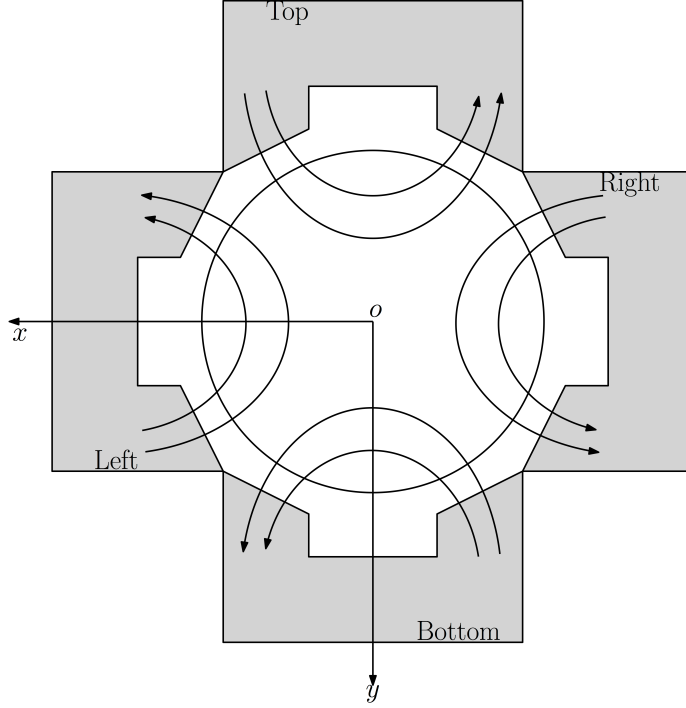
Figure 1.3: Simplified front-view of a typical AMB.

In this diagram, a four-pole AMB controls the position of the flywheel rotor along both the x- and y-axis. Considering the magnetic bearing force (B) induced by the electromagnets on the left and right side of the flywheel rotor, results in equation 1.4 [5].

$$B = \frac{\mu_0 A_g N^2 (i_0 + u)^2}{(c_r - x)^2} - \frac{\mu_0 A_g N^2 (i_0 - u)^2}{(c_r + x)^2} \tag{1.4}$$

In this equation, μ_0 is the permeability of air, A_g is the pole area, N is the winding number, i_0 is the bias current, u is the control current, c_r is the air gap, and x is the position of the rotor in the x-axis. This equation shows that the electromagnetic force is proportional

to the square of the coil current ($i_0 \pm u$) and inversely proportional to the square of the air gap ($c_r \pm x$). This relationship is highly nonlinear and is coupled with displacement and current. Furthermore, mass imbalances due to non-uniform material composition, gyroscopic effects/coupling, the changes in model characteristics as a function of rotor speed, and the flywheel rotor flexibility also play a role in accurate system modeling for high speed FES systems. With the exception of the last decade or so, most AMB controller approaches were linear. Some of these methods included, linear-quadratic design, eigenstructure assignment, modal control, and an integral type controller [5]. Thus, the maximum achievable angular velocity of flywheel rotors implementing these controller schemes was limited by the accuracy of their model with regards to the nonlinear parameters discussed above, and varied from experimental setup to setup.

The force generated by electromagnets is dependent on the material composition of the rotor and has a nonlinear, curved shape. This nonlinear, curved shape is partly a result of the hysteric behavior of electromagnets where flux lines are dislocated from their original pinning position to a new one; this effect is most notable when the rotor material is heterogeneous and anisotropic [8]. Figure 1.4 shows the static characteristics of the AMB force as a function of coil current (u) when deflections are small and hysteresis can be ignored [9]. The only time that the magnetic bearing force is zero is when the current is also zero. This means that AMBs require power in order to control the flywheel. For real systems, this causes a problem because all shafts rotate with some degree of eccentricity. Eccentric forces introduce non-periodic (i.e. highly nonlinear) whirring of the shaft that

becomes more significant with increasing speeds. Therefore, to implement controllers effectively, it is standard practice to use a small, constant current (called premagnetization or bias current) in each AMB coil to stabilize the rotor during operation and to reduce the maximum allowable operating speed [9]. However, this introduces an entirely new problem for FES systems: they need to be actively powered in order to store energy and they have a reduced maximum energy storage capacity.
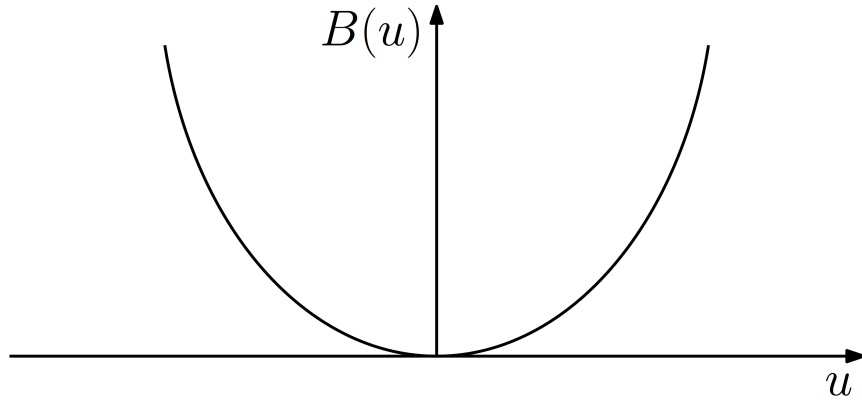
Figure 1.4: AMB force as a function of coil current.

Minimizing the total current required to control the shaft during operation will reduce the power draw of the system, but will also reduce the impact of apparent bearing drag (eddy-current loss). The eddy-current loss is produced from the interaction of the upward induced current density and the external magnetic field. Crucially, this interaction - confirmed with the right-hand-rule - opposes the motion of the rotor [10]. For laminated AMBs, eddy currents are generally negligible [11].

Large rotor displacements could lead to another issue with FES systems; flux saturation. Flux saturation of the magnetic material could result in a loss of the bearing's

restoring force and subsequently cause the rotor to crash into the AMBs. The flux saturation was first studied in [12] where the authors used an iterative method to estimate the flux density. An offshore turboexpander using AMBs demonstrated a nonlinear behavior induced by flux saturation when it experienced erratic, subsyncronous oscillations over a broad frequency range due to the reduced stiffness [13].

Modern FES systems research also is experimenting with the use of high-Tc superconductors. High-Tc superconductors are useful because they introduce strong pinning forces that hold the flywheel rotor on the central axis (serving the same purpose as premagnetization) [14]. Use of these superconducting magnetic bearings (SMB) has the ability to eliminate the requirement for a bias current in other AMB configurations; thus, reducing the power requirements of the AMBs. For high-Tc superconductors to function properly, they must be cooled using liquid nitrogen. Constant maintenance is required to ensure that the SMBs stay below their critical temperature. An example of a hybrid FES system is shown in Figure 1.5 using both SMB and permanent magnetic bearings (PMB).

In conclusion, the current research effort (geared towards increasing the maximum operating velocity or reducing required rotor radius for similar energy storage capacity) has been focused on finding a novel nonlinear controller scheme that requires the least amount of active control. One nonlinear controller scheme called 'wavelet-based time-frequency control' (WFXLMS) was recently introduced and has shown intriguing results for a rotor-AMB system [15]. For a rigid shaft, controlled in the radial direction, robust numerical simulation of this nonlinear controller has demonstrated that it is capable of effectively

11
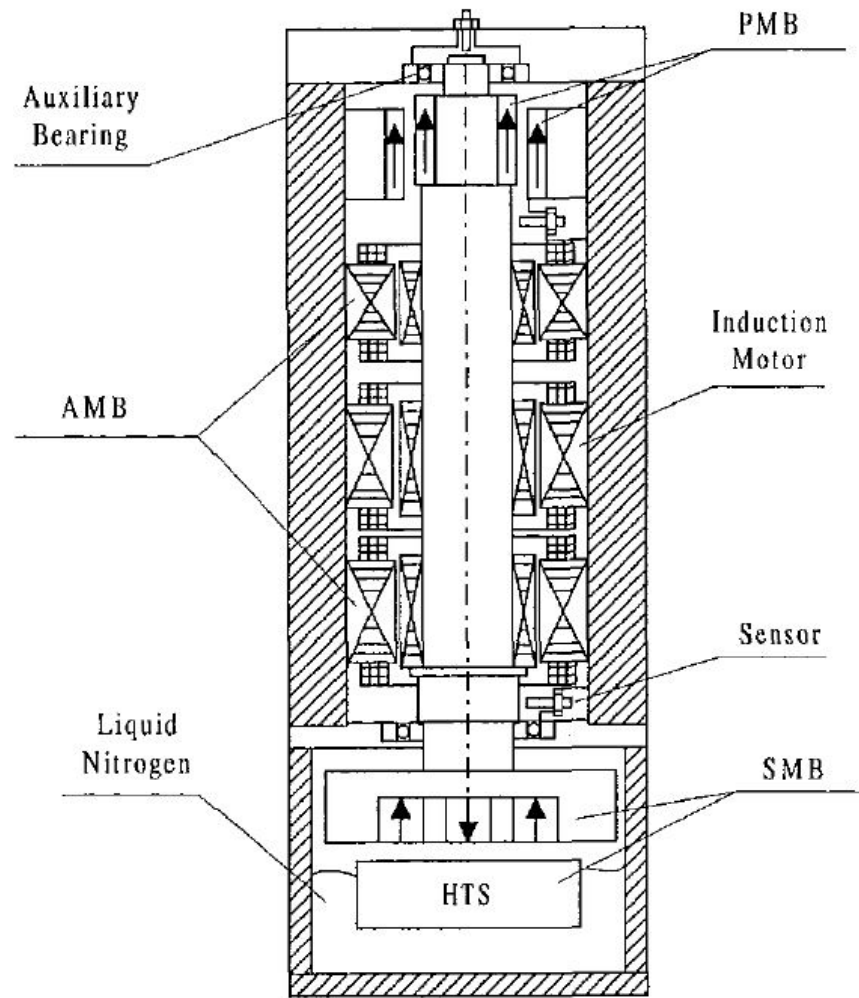
Figure 1.5: An example of a hybrid FES system using SMB and AMB [14].

controlling the shaft at speeds up to 187,500 rpm [15]. Thus, the subsequent research

provided by this thesis is the investigation of the robustness of this controller scheme for a

FES system with additional thrust control by comparing it to PID (linear) and fuzzy-logic

(nonlinear) controllers.

2 METHOD

For this thesis, some key assumptions were made. The first is that the rotor is suffi-
ciently stiff as to neglect vibrations due to a flexible shaft. Second, the bounds for accept-
able control were established such that the effects of flux saturation on system dynamics
are negligible. Next, the materials used in the FES system are considered to be homo-
geneous and isotropic; thereby neglecting hysteresis effects. Discrete excitation currents
in the AMBs were represented by a uniform flux density field across the bearing's cross-
section since variations in practice are relatively small.

2.1 Equations of Motion

For a FES system, it is imperative that the energy transferred to the flywheel is con-
verted to rotational energy only. Consequently, the rotor must remain sufficiently rigid as
to eliminate the transfer of rotational energy to shaft vibration. Based on this assertion, a
five-degree-of-freedom, rigid FES system (depicted in Figure 2.1) was used for this study.

The equations of motion for this system can be described by the following differential
equation

$$\mathbf{M_B \ddot{q}_B} + \omega \mathbf{G_B \dot{q}_B} = \mathbf{Q_B} \tag{2.1}$$

Where $\mathbf{M_B}$ and $\mathbf{G_B}$ are the mass and gyroscopic damping matrices of the FES system
(respectively), $\mathbf{Q_B}$ is the force exerted on the rotor, and $\mathbf{q_B}$ is the displacement vector.
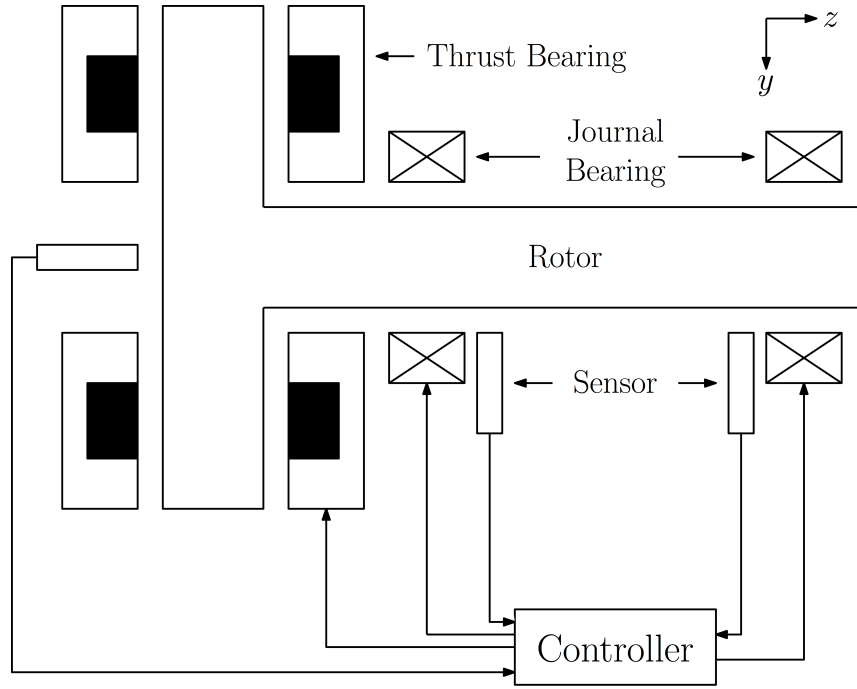
Figure 2.1: FES system schematic.

Summing the forces and moments generated by the thrust and journal bearings (shown in Figure 2.2) generates a system of five equations and five unknowns. These equations can be rewritten in matrix form as shown in equations 2.2 through 2.5

$$
\mathbf{M_B} = \frac{1}{l}
\begin{bmatrix}
l_b m & 0 & l_a m & 0 & 0 \\
0 & l_b m & 0 & l_a m & 0 \\
-J_y & 0 & J_y & 0 & 0 \\
0 & -J_x & 0 & J_x & 0 \\
0 & 0 & 0 & 0 & lm
\end{bmatrix}
\tag{2.2}
$$
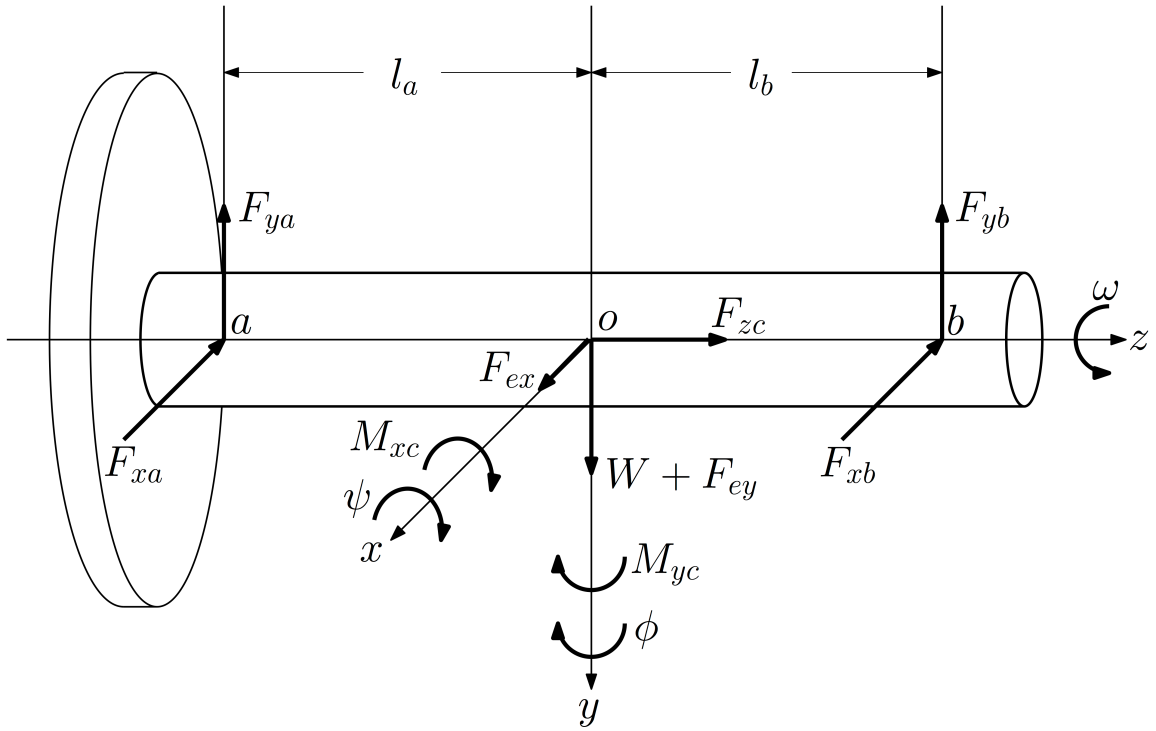
Figure 2.2: FBD of the FES system.

$$\mathbf{G_B} = \frac{J_z}{l} \begin{bmatrix} 0 & 0 & 0 & 0 & 0 \\ 0 & 0 & 0 & 0 & 0 \\ 0 & 1 & 0 & -1 & 0 \\ -1 & 0 & 1 & 0 & 0 \\ 0 & 0 & 0 & 0 & 0 \end{bmatrix} \tag{2.3}$$

$$
\mathbf{Q_B} = \left\{ \begin{array}{c} -F_{xa} - F_{xb} + em\omega^2 \sin(\omega t) \\[2mm] -F_{ya} - F_{yb} + W + em\omega^2 \cos(\omega t) \\[2mm] F_{xa}l_a - F_{xb}l_b + M_{yc} \\[2mm] F_{ya}l_a - F_{yb}l_b + M_{xc} \\[2mm] F_{zc} \end{array} \right\} \tag{2.4}
$$

$$
q_{\mathrm{B}} = \left\{ \begin{array}{c} x_a \\[2mm] y_a \\[2mm] x_b \\[2mm] y_b \\[2mm] z \end{array} \right\} \tag{2.5}
$$

where m is the mass of the rotor, J_x and J_y are the transverse moments of inertia, J_z is the polar moment of inertia, ω is the angular velocity of the rotor, l_a and l_b are the distances to journal bearings a and b from the geometric center of mass (O in Figure 2.2), $F_{xa,xb}$ and $F_{ya,yb}$ are the forces generated by both of the journal bearings in the x and y direction (respectively), F_{zc} is the force generated by the thrust bearing in the z direction, M_{xc} and M_{yc} are the moments of inertia generated by the thrust bearing in the x and y directions (respectively), and W is the weight of the rotor.

The FES system analyzed in this research had the physical parameters listed in Table 2.1 [16]. The parameters for the AMBs are shown in Table 2.2 [16]. These values were selected based on a real FES system that was controlled with a PID scheme.

16

Table 2.1: Rotor parameters.

Parameter	Value
l_a (mm)	74.3
l_b (mm)	105.7
m (kg)	9.6
J_x (kg/m^2)	0.128
J_y (kg/m^2)	0.128
J_z (kg/m^2)	0.01

Table 2.2: Bearing parameters.

AMB type	Parameter	Value
Journal bearings	Radial clearance	0.4 mm
	Winding number	57
	Width	44.2 mm
	Diameter	60 mm
Thrust bearing	Axial clearance	0.5 mm
	Winding number	143
	Diameter	75 mm
	R_1	33 mm
	R_2	46.95 mm
	R_3	67.15 mm
	R_4	75 mm

2.2 Electromagnetic Forces: Journal Bearings

For both journal bearings, an eight-pole configuration (Figure 2.3) was selected to control motion in both the x- and y- axis. Each pole generates a force that can be described by equations 2.6 through 2.9.

$$F_{xa} = f_{ra} - f_{la} - \alpha_{xy}\frac{x_a}{c_r}(f_{ta} + f_{ba}) \tag{2.6}$$
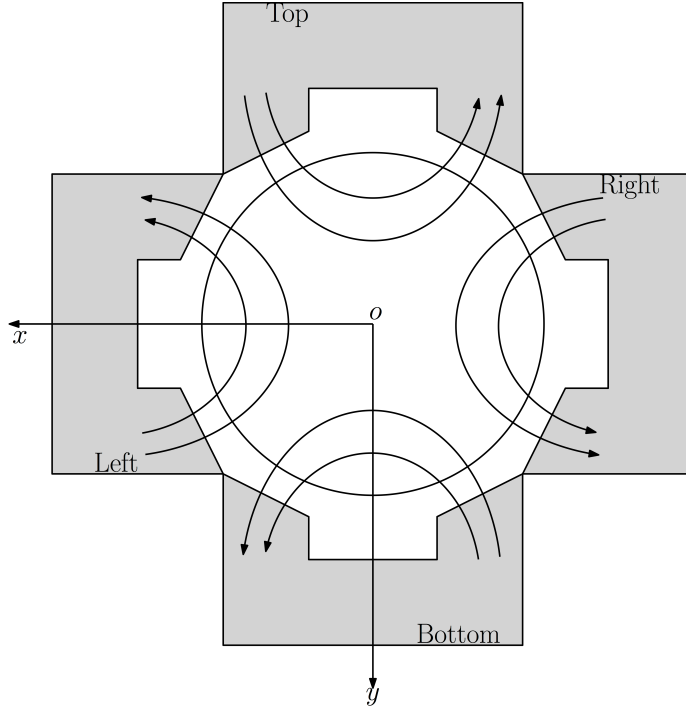
Figure 2.3: Cross-sectional view of an eight-pole journal bearing.

$$F_{ya} = f_{ta} - f_{ba} - \alpha_{xy} \frac{y_a}{c_r} (f_{ra} + f_{la}) \tag{2.7}$$

$$F_{xb} = f_{rb} - f_{lb} - \alpha_{xy} \frac{x_b}{c_r} (f_{tb} + f_{bb}) \tag{2.8}$$

$$F_{yb} = f_{tb} - f_{bb} - \alpha_{xy} \frac{y_b}{c_r} (f_{rb} + f_{lb}) \tag{2.9}$$

where

$$f_{ra} = \frac{\mu_0 N_r^2 A_r}{4} \frac{(I_{0r} + i_{xa})^2}{(c_r + x_a)^2} \tag{2.10}$$

18

$$f_{la} = \frac{\mu_0 N_r^2 A_r}{4} \frac{(I_{0r} - i_{xa})^2}{(c_r - x_a)^2} \tag{2.11}$$

$$f_{ta} = \frac{\mu_0 N_r^2 A_r}{4} \frac{(I_{0r} + i_{ya})^2}{(c_r + y_a)^2} \tag{2.12}$$

$$f_{ba} = \frac{\mu_0 N_r^2 A_r}{4} \frac{(I_{0r} - i_{ya})^2}{(c_r - y_a)^2} \tag{2.13}$$

$$f_{rb} = \frac{\mu_0 N_r^2 A_r}{4} \frac{(I_{0r} + i_{xb})^2}{(c_r + x_b)^2} \tag{2.14}$$

$$f_{lb} = \frac{\mu_0 N_r^2 A_r}{4} \frac{(I_{0r} - i_{xb})^2}{(c_r - x_b)^2} \tag{2.15}$$

$$f_{tb} = \frac{\mu_0 N_r^2 A_r}{4} \frac{(I_{0r} + i_{yb})^2}{(c_r + y_b)^2} \tag{2.16}$$

$$f_{bb} = \frac{\mu_0 N_r^2 A_r}{4} \frac{(I_{0r} - i_{yb})^2}{(c_r - y_b)^2} \tag{2.17}$$

In these equations, α_{xy} is the geometric coupling coefficient which was obtained experimentally in a previous study to have an average value of 0.16 [16]. Additionally, c_r is the radial clearance of the journal bearings, μ_0 is the permeability of air ($4\pi \times 10^{-7} N/A^2$), N_r and A_r are the winding number and pole areas of the journal bearings (respectively), I_{0r} is the bias current supplied to the journal bearings, and i_{ij} is the current supplied to the
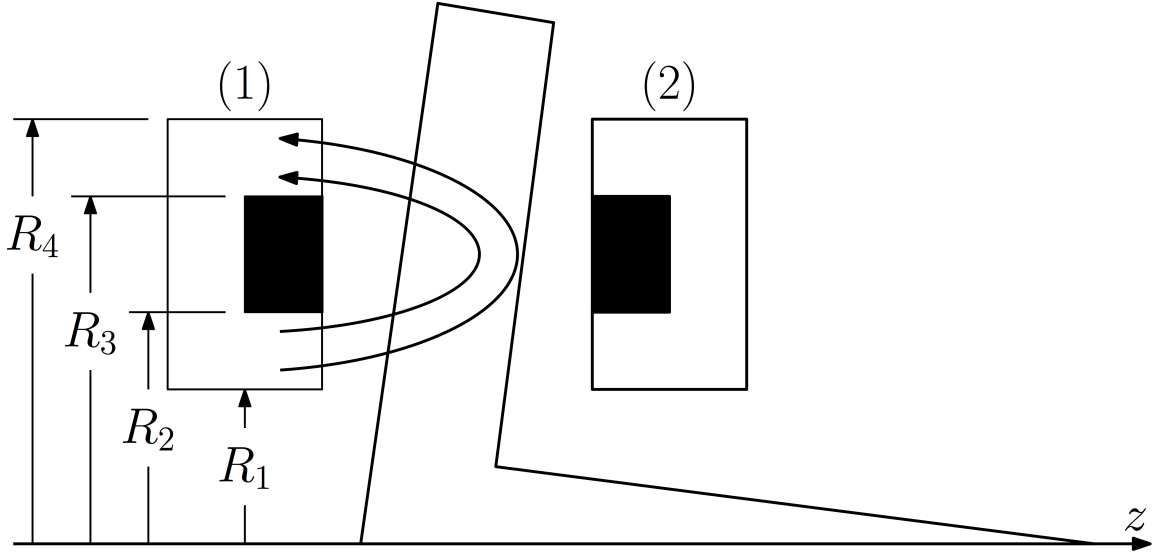
Figure 2.4: Cross-sectional view of a thrust bearing.

journal bearings from the controller.

2.3 Electromagnetic Forces: Thrust Bearing

A single, two-pole thrust bearing was used to apply a force on the larger disc on the left side of Figure 2.2. Figure 2.4 shows the cross section of the thrust bearing used in this research and depicts the flow of magnetic flux through the rotor. The air gaps for the outer and inner annuli of the thrust bearing (denoted by superscripts) are described as [16]

$$h_i^{(1)} = c_z + z - \sin(\phi)r_i\sin(\theta) - \sin(\psi)r_i\cos(\theta) \tag{2.18}$$

$$h_o^{(1)} = c_z + z - \sin(\phi)r_o\sin(\theta) - \sin(\psi)r_o\cos(\theta) \tag{2.19}$$

$$h_i^{(2)} = c_z - z + \sin(\phi) r_i \sin(\theta) + \sin(\psi) r_i \cos(\theta) \tag{2.20}$$

$$h_o^{(2)} = c_z - z + \sin(\phi) r_o \sin(\theta) + \sin(\psi) r_o \cos(\theta) \tag{2.21}$$

where c_z is the axial clearance of the thrust bearing, r_i and r_o are the inner and outer radius of the thrust bearing (respectively), and ϕ and ψ describe the tilt of the rotor about the x- and y- axis and are defined as follows

$$\phi \approx \frac{x_b - x_a}{l} \tag{2.22}$$

$$\psi \approx \frac{y_b - y_a}{l} \tag{2.23}$$

Assuming flux loss from (r_i, θ) to (r_o, θ) is minimal, the relationship between r_i and r_o can be defined as

$$r_o = R_4 + \alpha(r_i - R_1) \tag{2.24}$$

with

$$\alpha = -\frac{R_4 - R_3}{R_2 - R_1} \tag{2.25}$$

The force and moments created by the thrust bearing are expressed as

$$F_{zc} = F_{zc}^{(1)} + F_{zc}^{(2)} \tag{2.26}$$

$$M_{xc} = M_{xc}^{(1)} + M_{xc}^{(2)} \tag{2.27}$$

$$M_{yc} = M_{yc}^{(1)} + M_{yc}^{(2)} \tag{2.28}$$

These forces are highly nonlinear and are defined as follows [16].

$$
\begin{aligned}
F_{zc}^{(1)} = &-\int_0^{2\pi} \int_{R_1}^{R_2} \frac{[\alpha\mu_0 N(I_{0z}+i_z)]^2}{2\mu_0} \times \left[\frac{r_o/r_i}{h_o^{(1)} - \alpha(r_o/r_i)h_i^{(1)}} \right]^2 r_i dr_i d\theta \\
&+\int_0^{2\pi} \int_{R_4}^{R_3} \frac{[\mu_0 N(I_{0z}+i_z)]^2}{2\mu_0} \times \frac{1}{[h_o^{(1)} - \alpha(r_o/r_i)h_i^{(1)}]^2} r_o dr_o d\theta
\end{aligned}
\tag{2.29}
$$

$$
\begin{aligned}
F_{zc}^{(2)} = &\int_0^{2\pi} \int_{R_1}^{R_2} \frac{[\alpha\mu_0 N(I_{0z}-i_z)]^2}{2\mu_0} \times \left[\frac{r_o/r_i}{h_o^{(2)} - \alpha(r_o/r_i)h_i^{(2)}} \right]^2 r_i dr_i d\theta \\
&-\int_0^{2\pi} \int_{R_4}^{R_3} \frac{[\mu_0 N(I_{0z}-i_z)]^2}{2\mu_0} \times \frac{1}{[h_o^{(2)} - \alpha(r_o/r_i)h_i^{(2)}]^2} r_o dr_o d\theta
\end{aligned}
\tag{2.30}
$$

$$
\begin{aligned}
M_{xc}^{(1)} = &-\int_0^{2\pi} \int_{R_1}^{R_2} \frac{[\alpha\mu_0 N(I_{0z}+i_z)]^2}{2\mu_0} \times \left[\frac{r_o}{h_o^{(1)} - \alpha(r_o/r_i)h_i^{(1)}} \right]^2 \cos(\theta) dr_i d\theta \\
&+\int_0^{2\pi} \int_{R_4}^{R_3} \frac{[\mu_0 N(I_{0z}+i_z)]^2}{2\mu_0} \times \left[\frac{r_o}{h_o^{(1)} - \alpha(r_o/r_i)h_i^{(1)}} \right]^2 \cos(\theta) dr_o d\theta
\end{aligned}
\tag{2.31}
$$

$$
\begin{aligned}
M_{xc}^{(2)} = &\int_0^{2\pi} \int_{R_1}^{R_2} \frac{[\alpha\mu_0 N(I_{0z}-i_z)]^2}{2\mu_0} \times \left[\frac{r_o}{h_o^{(2)} - \alpha(r_o/r_i)h_i^{(2)}} \right]^2 \cos(\theta) dr_i d\theta \\
&-\int_0^{2\pi} \int_{R_4}^{R_3} \frac{[\mu_0 N(I_{0z}-i_z)]^2}{2\mu_0} \times \left[\frac{r_o}{h_o^{(2)} - \alpha(r_o/r_i)h_i^{(2)}} \right]^2 \cos(\theta) dr_o d\theta
\end{aligned}
\tag{2.32}
$$

$$M_{yc}^{(1)} = -\int_0^{2\pi} \int_{R_1}^{R_2} \frac{[\alpha\mu_0 N(I_{0z}+i_z)]^2}{2\mu_0} \times \left[\frac{r_o}{h_o^{(1)} - \alpha(r_o/r_i)h_i^{(1)}}\right]^2 \sin(\theta)dr_i d\theta$$

$$+ \int_0^{2\pi} \int_{R_4}^{R_3} \frac{[\mu_0 N(I_{0z}+i_z)]^2}{2\mu_0} \times \left[\frac{r_o}{h_o^{(1)} - \alpha(r_o/r_i)h_i^{(1)}}\right]^2 \sin(\theta)dr_o d\theta \qquad (2.33)$$

$$M_{yc}^{(2)} = \int_0^{2\pi} \int_{R_1}^{R_2} \frac{[\alpha\mu_0 N(I_{0z}-i_z)]^2}{2\mu_0} \times \left[\frac{r_o}{h_o^{(2)} - \alpha(r_o/r_i)h_i^{(2)}}\right]^2 \sin(\theta)dr_i d\theta$$

$$- \int_0^{2\pi} \int_{R_4}^{R_3} \frac{[\mu_0 N(I_{0z}-i_z)]^2}{2\mu_0} \times \left[\frac{r_o}{h_o^{(2)} - \alpha(r_o/r_i)h_i^{(2)}}\right]^2 \sin(\theta)dr_o d\theta \qquad (2.34)$$

Attempting to fully integrate equations 2.29 through 2.34 is impossible, but they can be solved using numerical integration techniques. For this research, a tiled, double numerical integration method was used for any section that did not have infinite integration limits. Integration limits that were infinite were solved using a single integration program evaluated over $x_{min} \le x \le x_{max}$. The inner integral was then evaluated over $y_{min}(x) \le y \le y_{max}(x)$.

2.4 Wavelet-Based Time-Frequency Control

The logic of the WFXLMS control scheme (see Figure 2.7) relies on discrete wavelet transformations (DWT) of Daubechies-3 wavelets (Table 2.3) and filtered-x least-mean-squared (LMS) algorithms [15]. The Daubechies-3 wavelet coefficients are exact and are used to create the scaling and wavelet functions in Figures 2.5 and 2.6. As feedback can perturb a nonlinear system, this controller uses feed-forward control of the FES system by implementing adaptive filters.
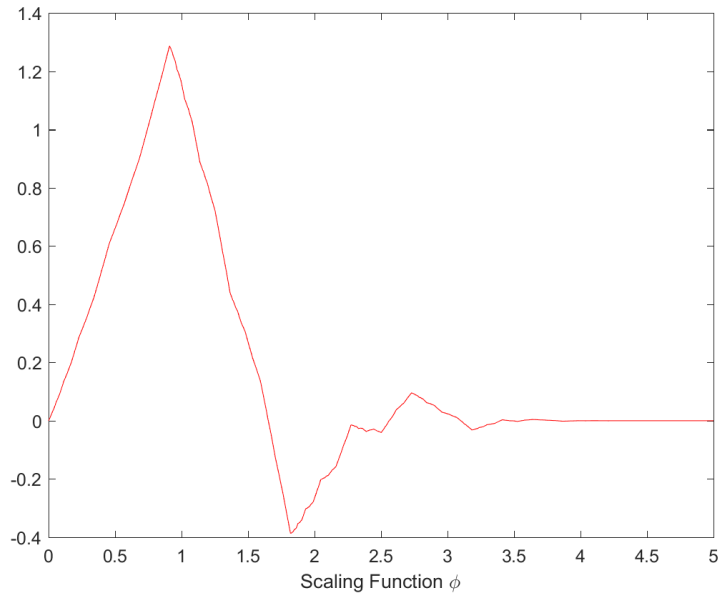
Figure 2.5: Scaling function for Daubechies-3 wavelet.
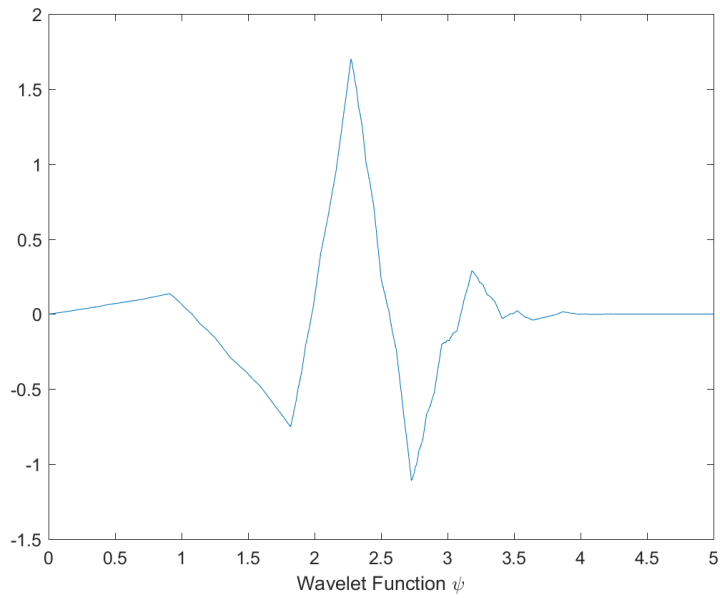
Figure 2.6: Wavelet function for Daubechies-3 wavelet.

Table 2.3: Daubechies-3 wavelet coefficients.

Decomposition low-pass filter		Deconstruction high-pass filter	
h_0	0.035226291882100656	g_0	-0.3326705529509569
h_1	-0.08544127388224149	g_1	0.8068915093133388
h_2	-0.13501102001039084	g_2	-0.4598775021193313
h_3	0.4598775021193313	g_3	-0.13501102001039084
h_4	0.8068915093133388	g_4	0.08544127388224149
h_5	0.3326705529509569	g_5	0.035226291882100656

Simultaneous time and frequency control of the FES system can be achieved by scaling the DWT and the wavelet coefficients. These two parameters describe all of the time and frequency information related to the signal. In Figure 2.7, there are two loops that help the controller operate successfully; referred to as the inner and outer loops.

For the outer loop, an adaptive filter $\mathbf{W}_2$ takes the input signal $(x(n))$ - after it has been decomposed into its wavelet coefficients using the $N \times N$ DWT matrix $\mathbf{T}$ - and generates the control signal $(u(n))$ based on the residual error $(e(n))$ between the output of the FES system $(y(n))$ and the desired response $(d(n))$. The values for the adaptive filters are updated by attempting to minimize the residual error using the LMS blocks. The inner loop operates in a similar manner to the outer loop, but it is used as a method of on-line system identification. In other words, this system characterizes the time and frequency response of the nonlinear system based on the system identification error $(f(n))$. Finally, a filter $\hat{\mathbf{W}}_1$ is applied to compensate for the possible disturbances that appear in the propagation of $u(n)$.

The weight vectors of $\mathbf{W}_1$ and $\mathbf{W}_2$ at time step n are

$$\mathbf{W}_1(n) = [w_{1,1}(n), w_{1,2}(n), \cdots, w_{1,N}(n)] \quad (2.35)$$
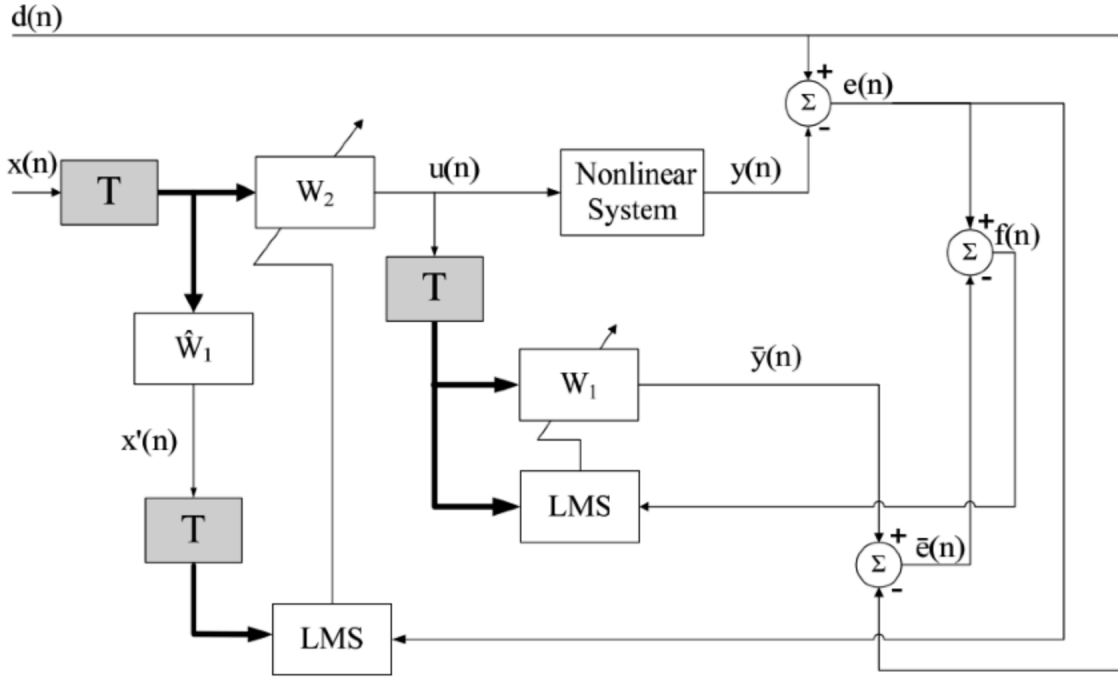
Figure 2.7: WFXLMS controller for a FES system.

$$\mathbf{W}_2(n) = [w_{2,1}(n), w_{2,2}(n), \cdots, w_{2,N}(n)] \tag{2.36}$$

where N is the length of the weight vector. The $N \times N$ DWT filter bank $\mathbf{T}$ used for this research is

$$\mathbf{T} = \begin{bmatrix} T_{11} & T_{12} & \cdots & T_{1N} \\ T_{21} & T_{22} & \cdots & T_{2N} \\ \vdots & \cdots & \ddots & \vdots \\ T_{N1} & T_{N2} & \cdots & T_{NN} \end{bmatrix} \tag{2.37}$$

For this FES system, $d(n)$ is defined for x_a, y_a, x_b, y_b, and z. Thus, for the FES system

$y(n)$ is the actual, real-time position of the rotor in a single coordinate direction, and

$$\bar{y}(n) = \mathbf{W}_1^\mathbf{T}(n)\mathbf{T}\mathbf{U}(n) \tag{2.38}$$

is the estimated position of the shaft based on the calculations done in the inner loop.

The controlled signal array $\mathbf{U}(n)$ is defined as

$$\mathbf{U}(n) = [u(n), u(n-1), \cdots, u(n-N+1)]^\mathbf{T} \tag{2.39}$$

The input control vector to the FES system is defined as

$$\mathbf{X}(n) = [x(n), x(n-1), \cdots, x(n-N+1)]^\mathbf{T} \tag{2.40}$$

and is used in the controlled signal equation (shown below)

$$u(n) = \mathbf{W}_2^\mathbf{T}\mathbf{T}\mathbf{X}(n) \tag{2.41}$$

The estimation $(e(n))$ and identification error $(\bar{e}(n))$ are

$$e(n) = d(n) - y(n) \tag{2.42}$$

$$\bar{e}(n) = \bar{y}(n) - d(n) \tag{2.43}$$

and the difference between them is defined as

$$f(n) = e(n) - \bar{e}(n) \tag{2.44}$$

The feed-forward, adaptive algorithms used to update the filter coefficients are

$$\mathbf{W}_1(n+1) = \mathbf{W}_1(n) + \mu_1(n)\mathbf{TU}(n)f(n) \tag{2.45}$$

$$\mathbf{W}_2(n+1) = \mathbf{W}_2(n) + \mu_2(n)\mathbf{T}\hat{\mathbf{X}}(n)e(n) \tag{2.46}$$

where μ_1 and μ_2 are step-sizes. The compensated output vector generated by the filter $\hat{\mathbf{W}}_1$ is defined as

$$\hat{\mathbf{X}}(n) = [\hat{x}(n), \hat{x}(n-1), \cdots, \hat{x}(n-N+1)]^{\mathbf{T}} \tag{2.47}$$

and

$$\hat{x}(n) = \mathbf{W}_1^{\mathbf{T}}\mathbf{TX}(n) \tag{2.48}$$

2.5 PID Control

The parameters used for PID control of this FES system were optimized in a previous study and tweaked to improve performance using a trial and error method [16]. The specific parameters used for the control are listed in Table 2.4

where K_p is the proportional gain, K_i is the integral gain, K_d is the derivative gain, and

Table 2.4: PID simulation parameters.

Parameter	Value
K_p	38
K_i (s^{-1})	100
K_d (s)	0.5
G	7800
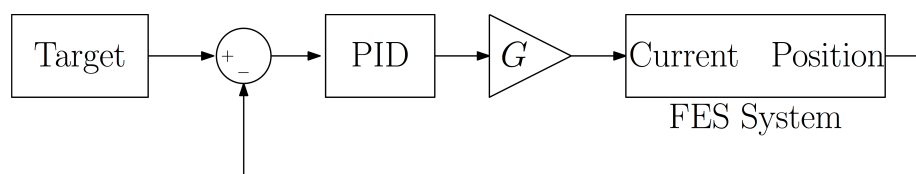
Figure 2.8: PID controller logic.

G is the gain multiplied to the output of the controller. The schematic for the PID controller is depicted in Figure 2.8. A discrete-time method was employed using the forward Forward Euler setting in the SIMULINK control toolbox.

2.6 Fuzzy-Logic Control

The fuzzy logic control (FLC) scheme used to control the FES system is shown in Figure 2.9. This figure shows that the FLC controller requires both position error and rate of change of the position error as inputs to calculate the desired current.

For this controller, trapezoidal and triangular membership functions (MF) were se-
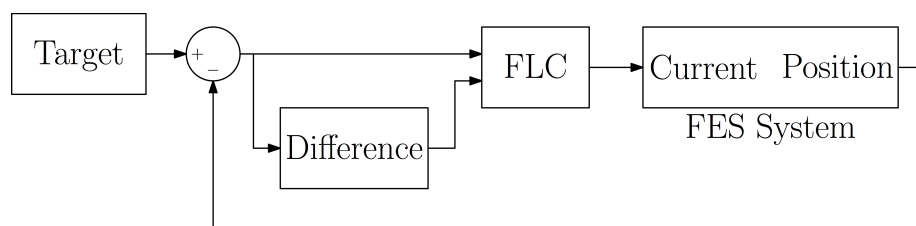
Figure 2.9: Fuzzy logic controller.
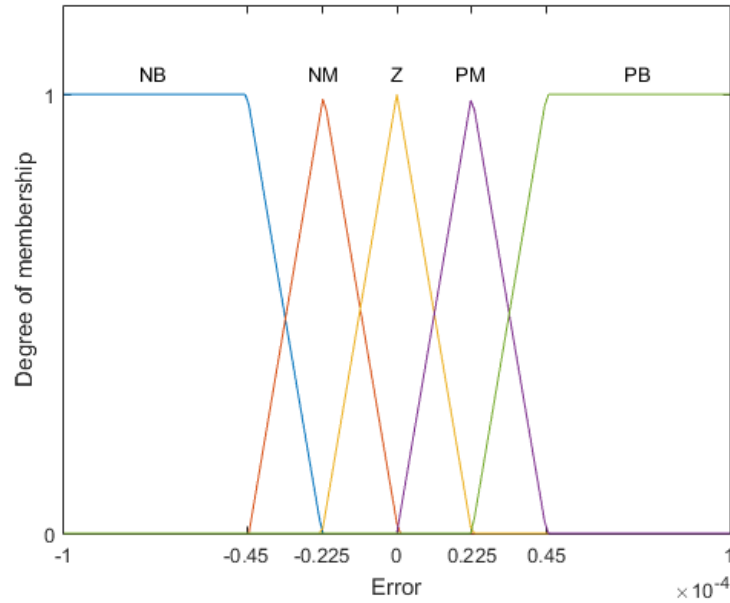
Figure 2.10: Membership function for error input.

Table 2.5: FLC rule base.

		$\Delta Error/\Delta t$				
		NB	**NM**	**Z**	**PM**	**PB**
	NB	NB	NB	NM	NM	Z
	NM	NB	NB	NM	Z	Z
Error	**Z**	NM	NM	Z	PM	PM
	PM	Z	Z	PM	PB	PB
	PB	Z	PM	PM	PB	PB

lected for simplicity, faster rise and settling times, and a higher computational efficiency [17]. Specifically, 5 MFs were selected for both of the inputs and the output of the controller with the trapezoidal covering the extreme values and the triangular covering the middle. The specific values for each MF were established by trial and error and are shown in Figures 2.10, through 2.12.

The rule base that was used by the inference engine in the FLC is in Table 2.5 [17].

30
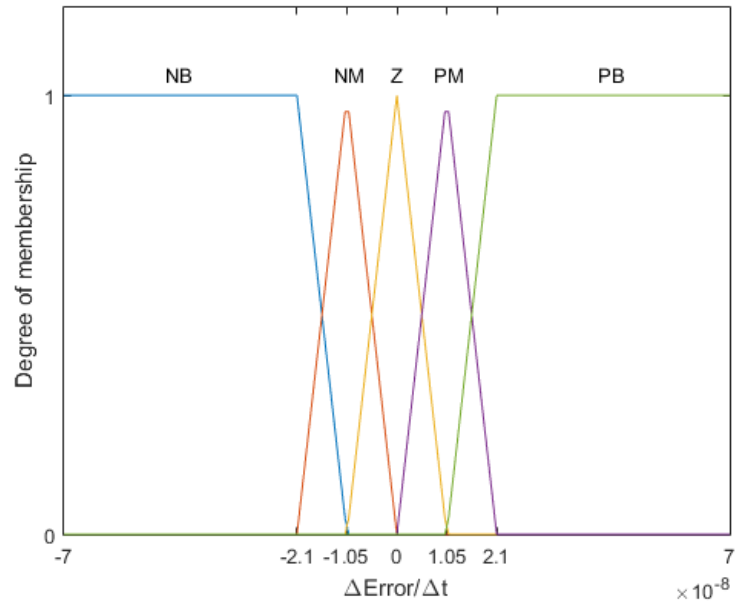
Figure 2.11: Membership function for change-in-error input.
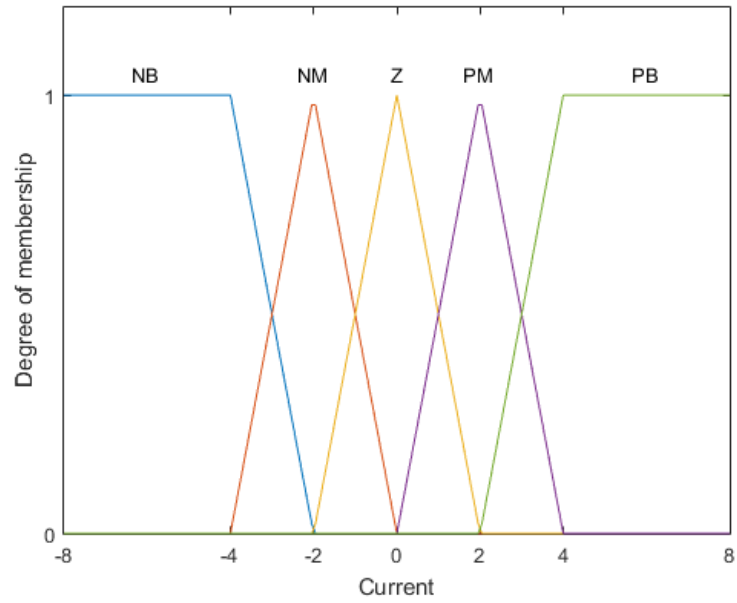
Figure 2.12: Membership function for current output.

The membership functions were implemented in the Fuzzy-Logic toolbox provided by MATLAB to obtain the numerical solutions in this thesis.

3   RESULTS AND DISCUSSION

The flywheel model was configured in a SIMULINK environment (see Appendix A for details) using an ordinary differential equation (ODE) solver called 'ode45.' The results of the PID, fuzzy-logic, and wavelet-based time-frequency controller are presented in the following sections.

3.1   PID Results

The PID controller was tested over a limited range but demonstrated effective control of the flywheel system. The PID parameters used for this test were presented in Table 2.4 but are included in Table 3.1 for convenience. The following subsections show the results of some of the simulations.

Table 3.1: PID parameters.

Parameter	Value
K_p	38
K_i (s^{-1})	100
K_d (s)	0.5
G	7800

3.1.1   Test 1

The flywheel parameters used for this test are listed in Table 3.2. The step size for the ODE solver was 1×10^{-6} seconds. The average and maximum values for the current and position based on this simulation are shown in Table 3.3.

Table 3.2: PID test 1 conditions.

Term	Value	Units
ω	100000	rpm
	1667	Hz
e	1	μm
I_{0r}	4	A
I_{0z}	4	A

Table 3.3: PID test 1 results.

Term	Axis	Average	Maximum
	x	6.79×10^{-1}	1.80×10^{0}
Current (A)	y	6.89×10^{-1}	1.63×10^{0}
	z	2.54×10^{-9}	1.41×10^{-8}
	x	9.89×10^{-7}	2.75×10^{-6}
Magnitude (m)	y	9.95×10^{-7}	2.51×10^{-6}
	z	3.70×10^{-15}	2.07×10^{-14}

The time domain response of the FES system for all three bearings are shown in Figures 3.1 through 3.3.

An instantaneous frequency (IF) plot of each temporal response was generated to evaluate the stability in the frequency domain and is shown in Figures 3.4 through 3.8. The raw data generated for each bearing had significant signal processing noise due to the nature of the IF calculations process. Therefore, a smoothing function was applied to this data to reveal the frequency trends and omit unnecessary data outliers. When comparing the raw plot with the smoothed plot, there was not a noticeable difference in the general trend of the data. Therefore, it is reasonable to assume that these plots do an adequate job depicting the controller's stability in the frequency domain.

While this data looks like it converged, a linear trend line from 1.5 seconds to the end

Figure 3.1: PID test 1: independent bearing A temporal responses.
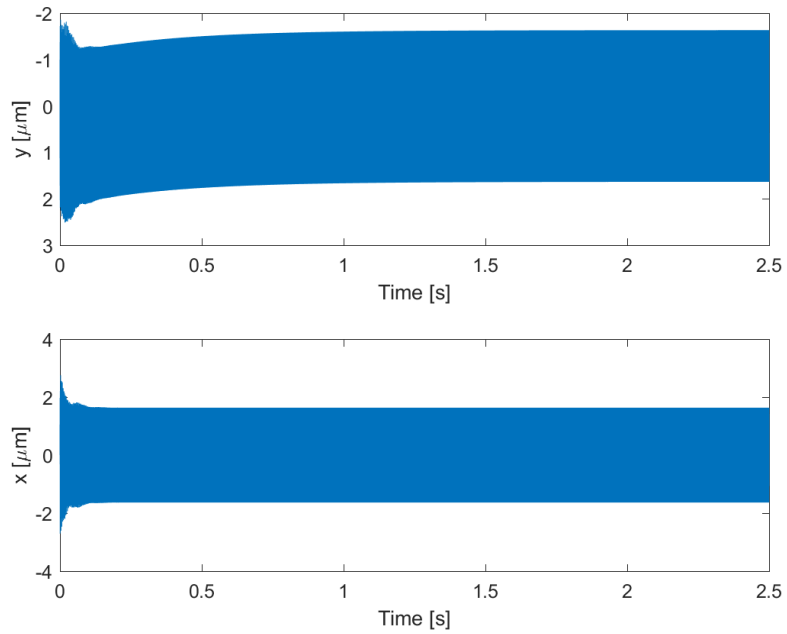
Figure 3.2: PID test 1: independent bearing B temporal responses.
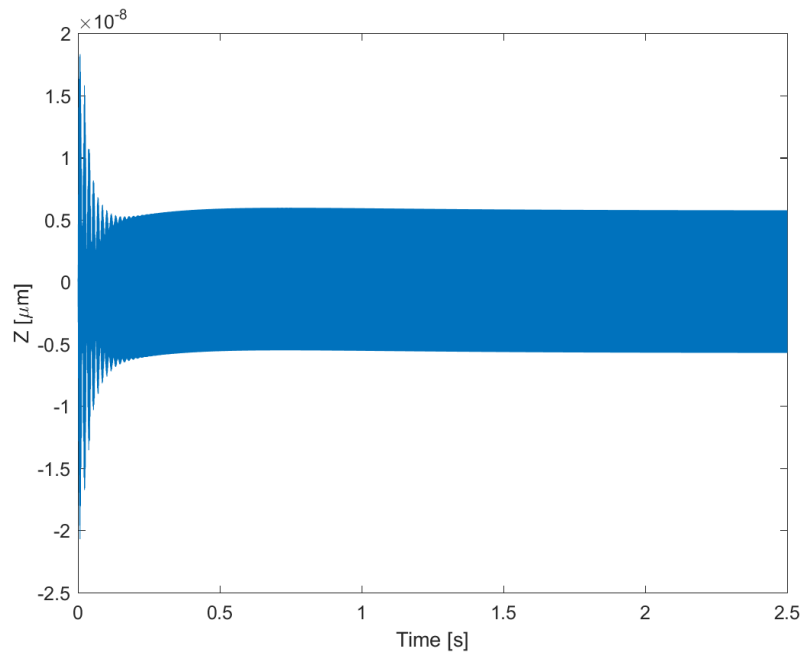
Figure 3.3: PID test 1: thrust bearing.

Figure 3.4: PID test 1: bearing A IF response for *y*-axis.

Figure 3.5: PID test 1: bearing A IF response for *x*-axis.

Figure 3.6: PID test 1: bearing B IF response for *y*-axis.

Figure 3.7: PID test 1: bearing B IF response for *x*-axis.
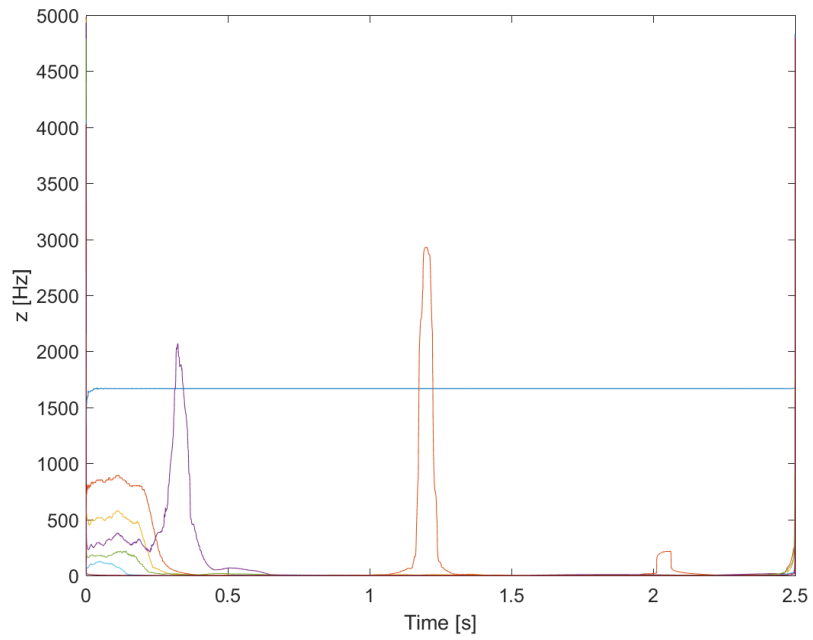
Figure 3.8: PID test 1: thrust bearing IF response.

of the simulation was created for the *y*-axis at bearing A and B to verify the *y*-axis stability (Figures 3.9 and 3.10).
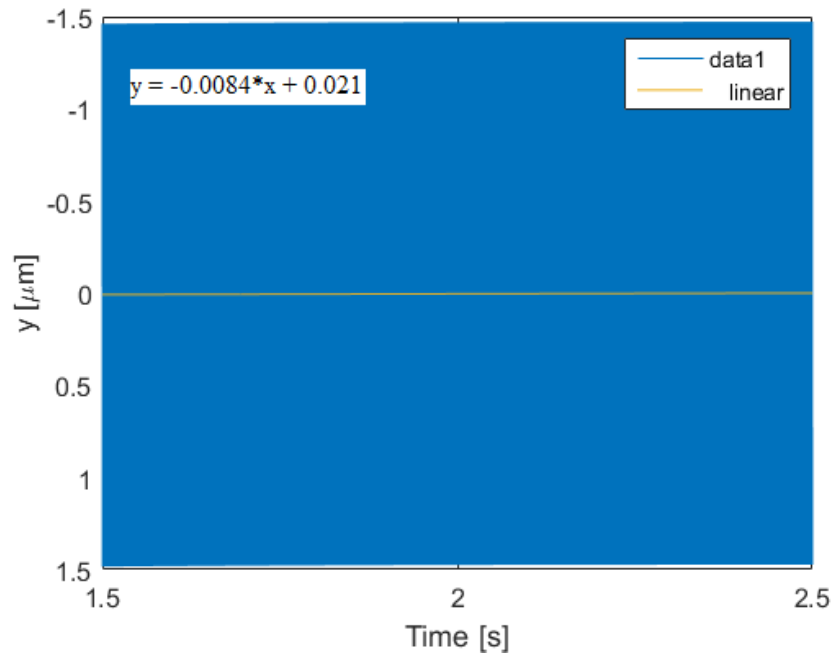
Figure 3.9: PID test 1: linear trend line for *y*-axis at bearing A.

The temporal and IF plots of this test in the *x*-axis (Figures 3.1 3.2, 3.5, and 3.7) all show near instant convergence and stability. Where the controller struggles a little more noticeably is in the *y*-axis of the temporal and frequency response. Clearly, the effect of gravity on this axis has an impact on stability. However, around 0.5 seconds into the simulation, the controller seems to achieve a similar level of stability as the *x*-axis in the temporal domain (Figures 3.1 and 3.2) and it completely eliminates the gravity's low-frequency impact in the frequency domain (Figures 3.4 and 3.6).

The *z*-axis stability is slightly different. The average amplitude of motion in the
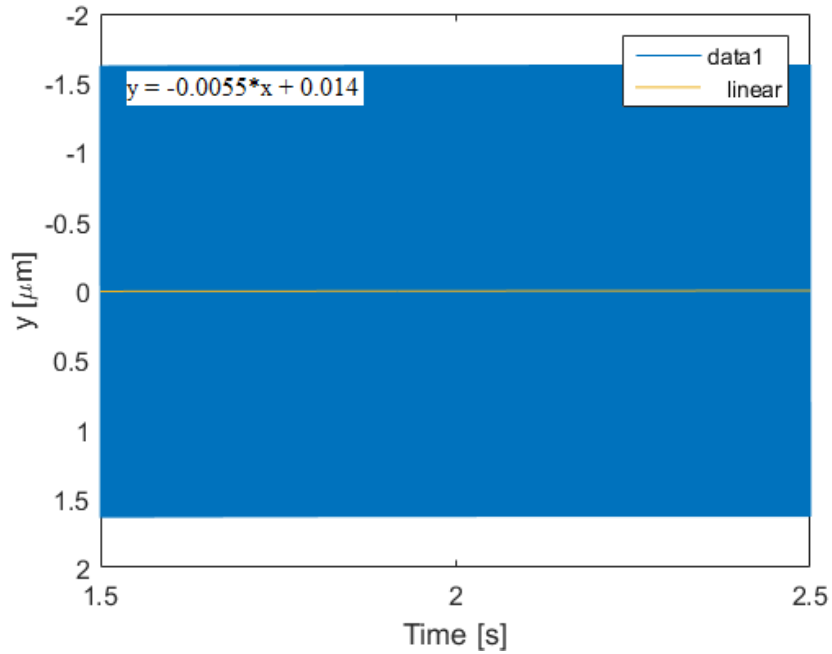
Figure 3.10: PID test 1: linear trend line for *y*-axis at bearing B.

temporal domain (Figure 3.3) is far less than in the *x*- or *y*-axis, but it still demonstrates a stable oscillation about zero after one second of the simulation. Looking at the IF of the thrust bearing in Figure 3.8 reveals that the high frequency oscillation matches the *x*- and *y*-axis at 100,000 rpm (1,667 Hz) despite its independence from the eccentric excitation force. In contrast, the low-frequency behavior is notably different than the *x*- and *y*-axis. There are two peaks that emerge from zero a after the start of the simulation. This behavior is likely indicative of a low frequency overshoot of the control target. Therefore, even though it may not be obvious in the temporal response, the *z*-axis controller probably overshoots the target slightly before correcting and reaching stability in the time domain.

Finally, Figures 3.9 and 3.10 show a maximum slope of about $-0.0084 \mu m/s$ in the *y*-axis for the final second of the simulation. This can be considered a slope of 0 and that

the controller has reached stability in the time domain.

3.1.2 Test 2

The flywheel parameters used for this test are listed in Table 3.6. The step size for the ODE solver was 1×10^{-6} seconds. From these testing conditions, the average and maximum values for the current and position in Table 3.5 were determined.

Table 3.4: PID test 2 conditions.

Term	Value	Units
ω	150000	rpm
	2500	Hz
e	1	μm
I_{0r}	4	A
I_{0z}	4	A

Table 3.5: PID test 2 results.

Term	Axis	Average	Maximum
	x	5.19×10^{-1}	1.22×10^{0}
Current (A)	y	5.31×10^{-1}	1.22×10^{0}
	z	9.08×10^{-11}	1.68×10^{-9}
	x	7.56×10^{-7}	1.78×10^{-6}
Magnitude (m)	y	7.64×10^{-7}	1.91×10^{-6}
	z	1.83×10^{-16}	2.57×10^{-15}

The time domain response of the FES system at the three bearings are shown in Figures 3.11 through 3.13.

An instantaneous frequency (IF) plot of each temporal response was generated to evaluate the stability in the frequency domain and is shown in Figures 3.14 through 3.18. The raw data generated for each bearing had significant signal processing noise due to the
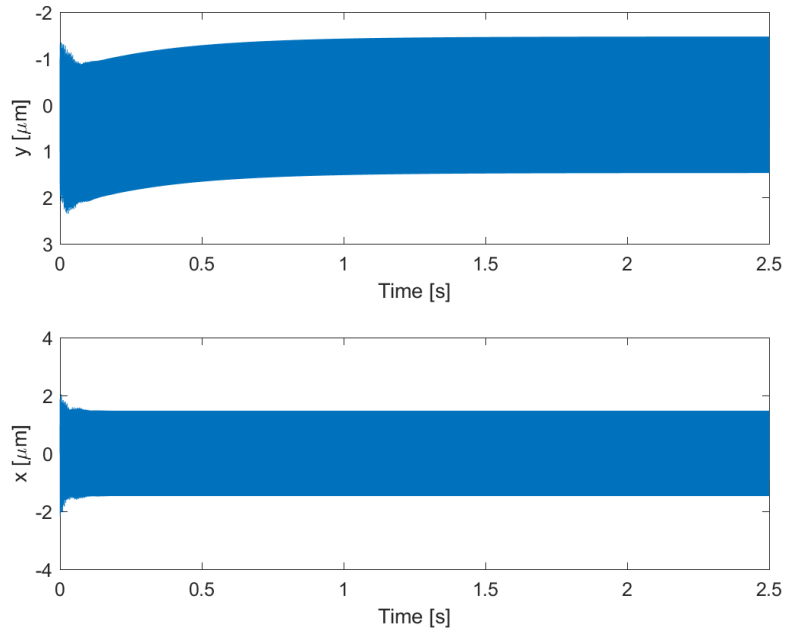
Figure 3.11: PID test 2: independent bearing A temporal responses.
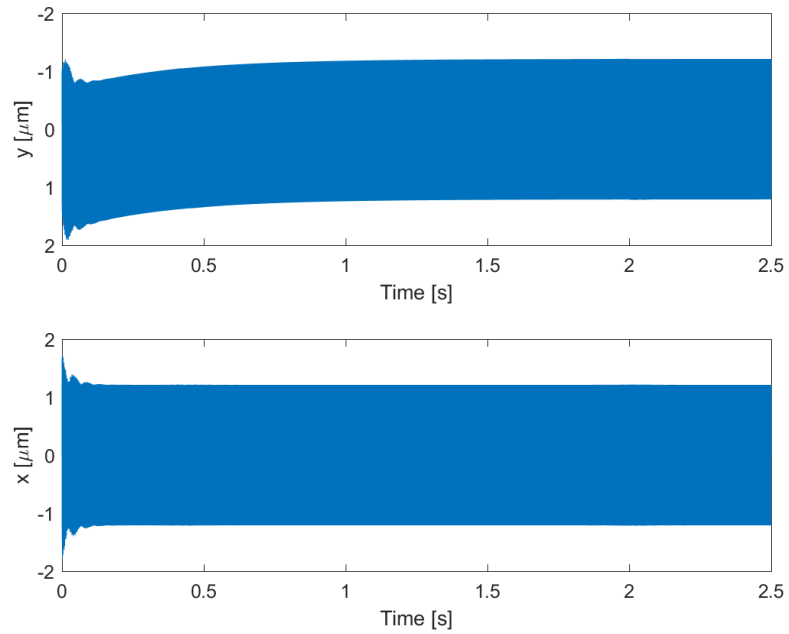
Figure 3.12: PID test 2: independent bearing B temporal responses.
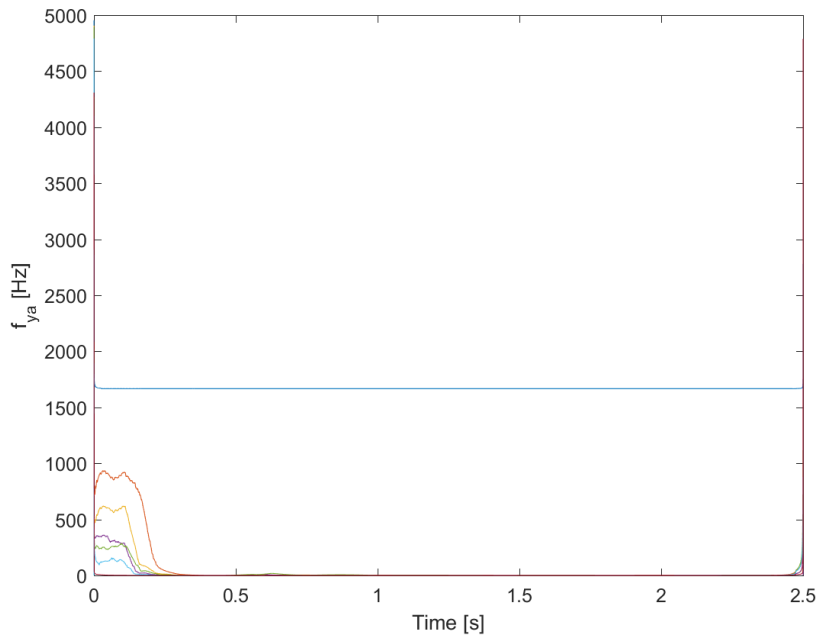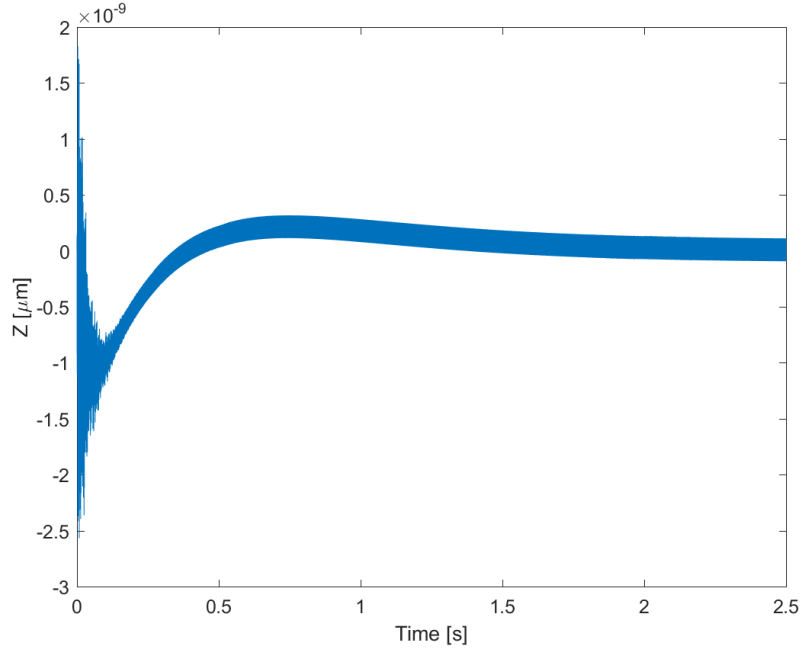
Figure 3.13: PID test 2: thrust bearing.

nature of the IF calculations process. Therefore, a smoothing function was applied to this data to reveal the frequency trends and omit unnecessary data outliers. When comparing the raw plot with the smoothed plot, there was not a noticeable difference in the general trend of the data. Therefore, it is reasonable to assume that these plots do an adequate job depicting the controller's stability in the frequency domain.

This test used the identical PID parameters as test 1, but increased the operating speed to 150,000 rpm. The first notable difference between this test and the last one is the magnitude of the z-axis displacement in the time domain (Table 3.3 vs. Table 3.5). It seems that the gyroscopic behavior of the flywheel was magnified because it was operating 50,000 rpm faster than for test 1, and the increased resistance to rotation allowed the controller to limit the tilting about the x- and y-axis. Additionally, the observed decrease in mean and

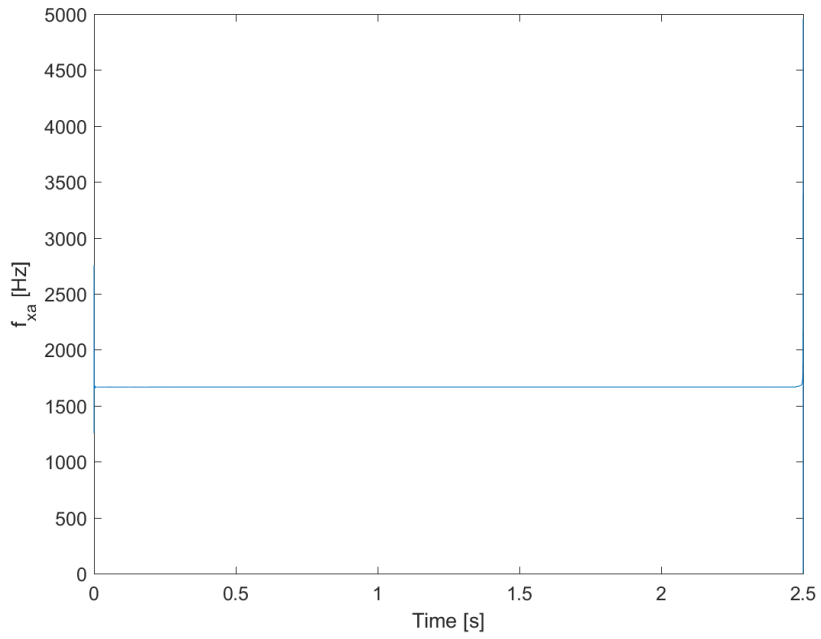Figure 3.14: PID test 2: bearing A IF response for *y*-axis.

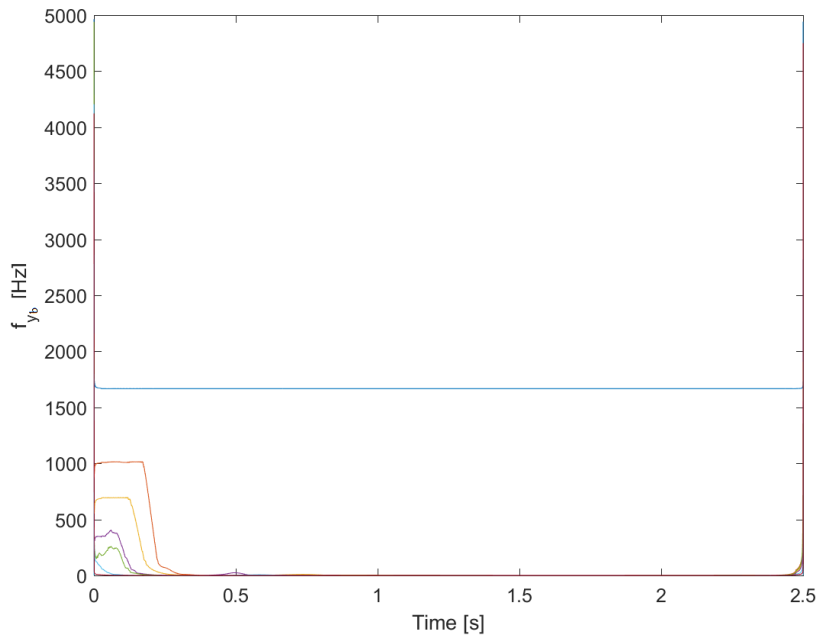Figure 3.15: PID test 2: bearing A IF response for *x*-axis.
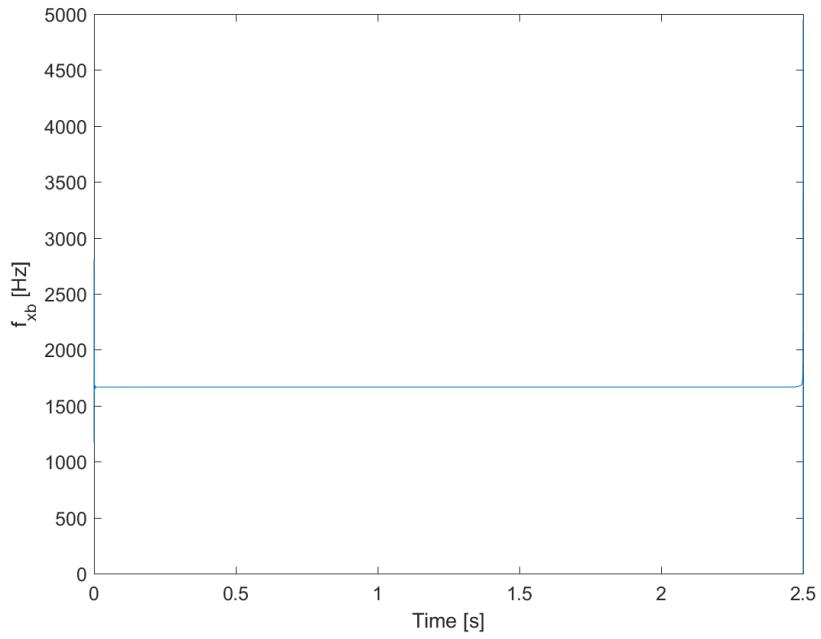
Figure 3.16: PID test 2: bearing B IF response for *y*-axis.

Figure 3.17: PID test 2: bearing B IF response for *x*-axis.
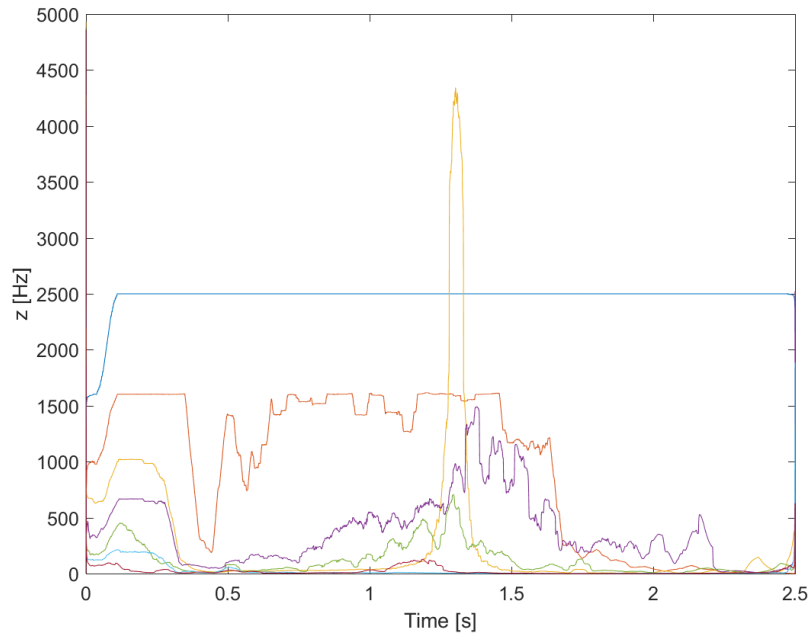
Figure 3.18: PID test 2: thrust bearing IF response.

maximum displacement was also observed in the x- and y-axis. Reduction in the magnitude

of oscillation in the time domain also resulted in a noticeable reduction in required control

current. The maximum control current was applied at the beginning of the simulation and

was similar to test 1, but the average control current was one order of magnitude smaller

for the x- and y-axis and two orders of magnitude smaller in the z axis.

The time domain responses in Figures 3.11 through 3.13 match the shape of test 1, but

all the overshoot - particularly in the z-axis (Figure 3.13) is more exaggerated and appears

to take a longer time to settle. Again, this is likely due to the increase in the gyroscopic

effect; all actions that the controller takes are resisted with a greater force.

In the frequency domain, the response is less stable. This indicates that the exact

position of the shaft is difficult to predict since the frequencies are changing in an unpre-

dictable manner. While the *y*-axis IF plots (Figures 3.14 and 3.16) show a similar response to test 1, newer low-frequency modes appear in the *x*-axis plots that did not exist before (Figures 3.15 and 3.17); particularly for bearing B. While the controller does handle - and eventually eliminate - the controller overshoot, this is a new phenomenon that was not observed before.

Finally, the IF response of the *z*-axis (Figure 3.18) is drastically different than in test 1. First, a new low-frequency mode was added at about 1,500 Hz for the first 1.5 seconds. The frequency peak at about 1.3 seconds is again likely due to the presence of target overshoot and matches up with when the controller begins to slow its approach towards the target.

3.1.3 Test 3

The flywheel parameters used for this test are listed in Table 3.6. The step size for the ODE solver was 1×10^{-6} seconds. From these testing conditions, the average and maximum values for the current and position in Table 3.7 were determined.

Table 3.6: PID test 3 conditions.

Term	Value	Units
ω	200000	rpm
	3333	Hz
e	1	μm
I_{0r}	4	A
I_{0z}	4	A

The time domain response of the FES system at the three bearings are shown in Figures 3.19 through 3.21.

An instantaneous frequency (IF) plot of each temporal response was generated to

47

Table 3.7: PID test 3 results.

Term	Axis	Average	Maximum
	x	4.80×10^{-1}	1.01×10^{0}
Current (A)	y	4.93×10^{-1}	1.10×10^{0}
	z	6.79×10^{-11}	8.17×10^{-10}
	x	6.99×10^{-7}	1.48×10^{-6}
Magnitude (m)	y	7.07×10^{-7}	1.77×10^{-6}
	z	1.65×10^{-16}	1.42×10^{-15}
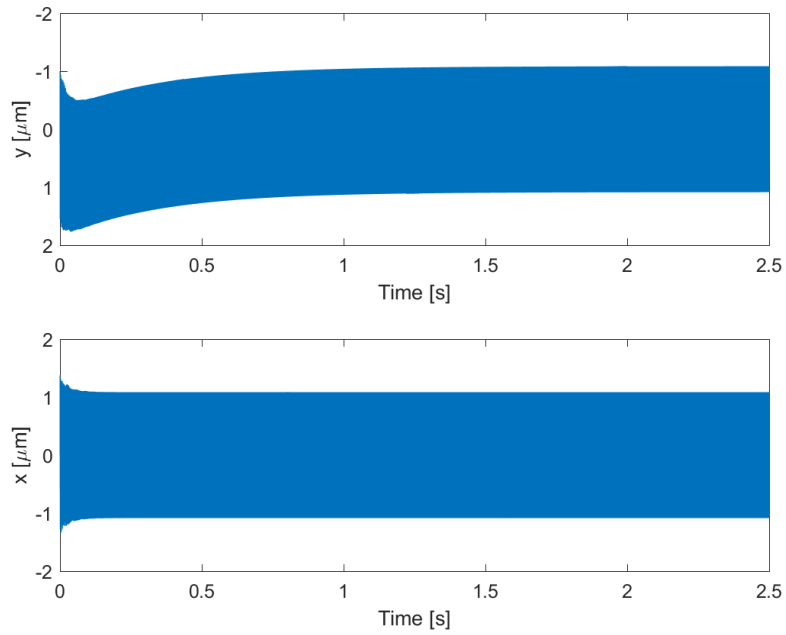
Figure 3.19: PID test 3: independent bearing A temporal responses.

evaluate the stability in the frequency domain and is shown in Figures 3.22 through 3.26.

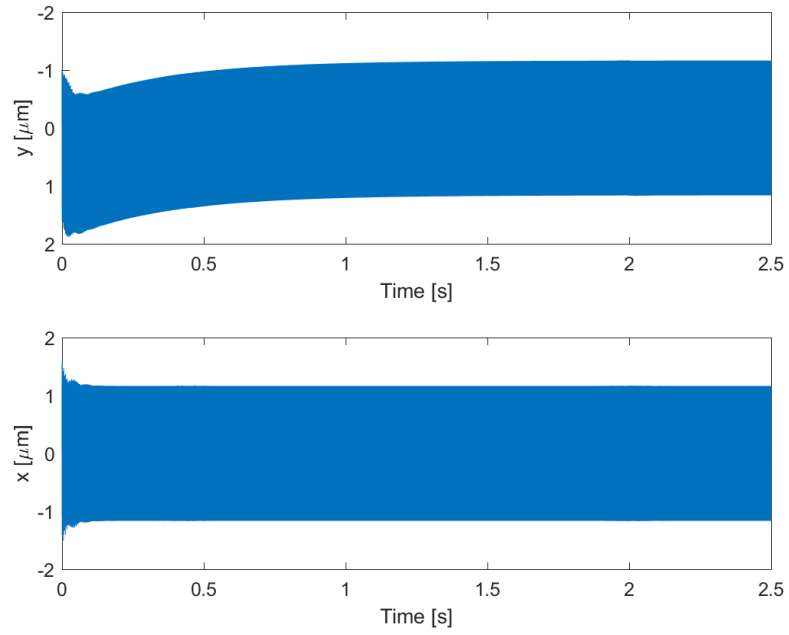The raw data generated for each bearing had significant signal processing noise due to the

nature of the IF calculations process. Therefore, a smoothing function was applied to this

data to reveal the frequency trends and omit unnecessary data outliers. When comparing

the raw plot with the smoothed plot, there was not a noticeable difference in the general

trend of the data. Therefore, it is reasonable to assume that these plots do an adequate job
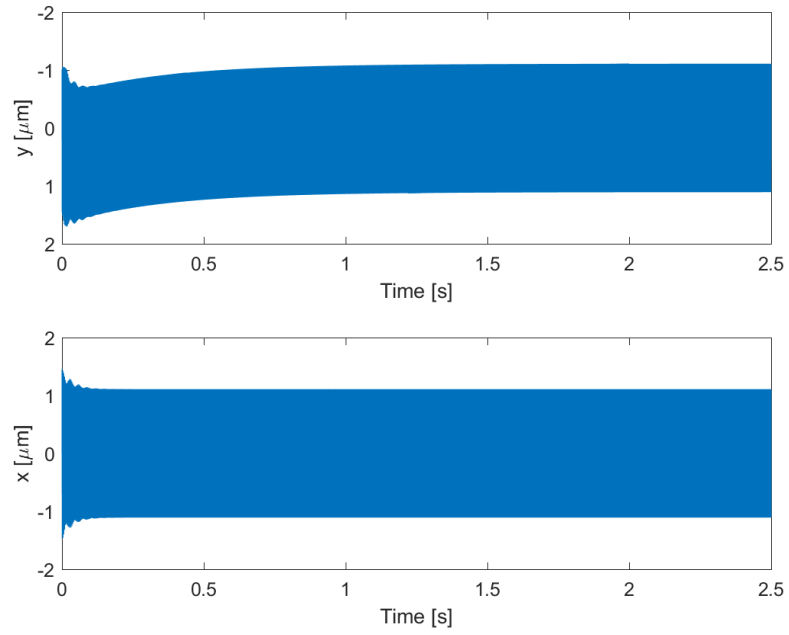
Figure 3.20: PID test 3: independent bearing B temporal responses.
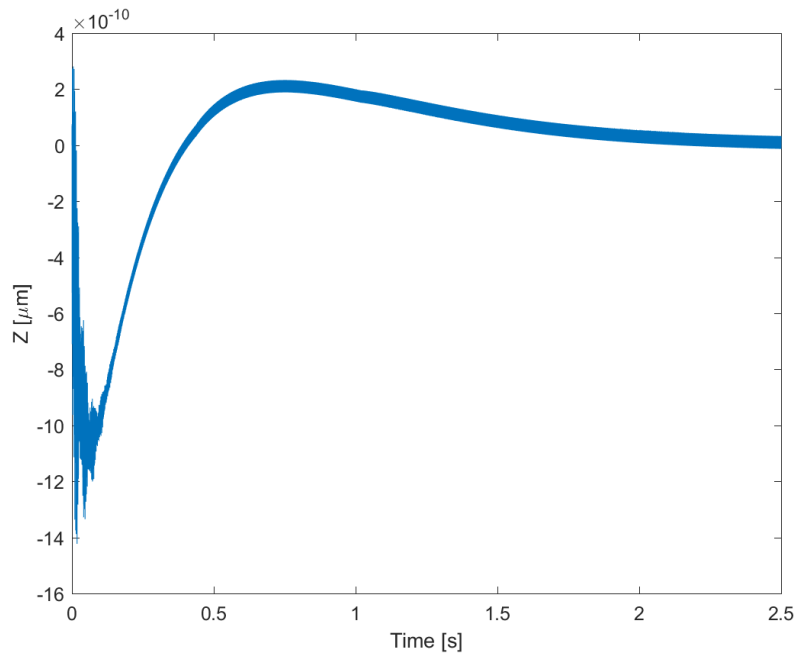
Figure 3.21: PID test 3: thrust bearing.

depicting the controller's stability in the frequency domain.
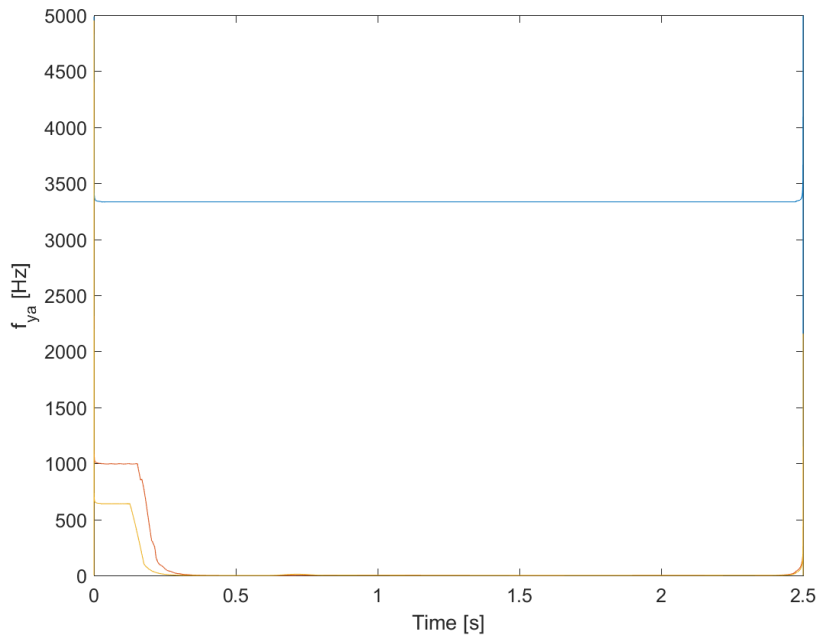
Figure 3.22: PID test 3: bearing A IF response for *y*-axis.

This is the last test for the PID controller. This test used the same controller parameters but increased the operating speed to 200,000 rpm. Spinning the rotor even faster seems to continue the trend observed from test 1 to 2. A reduction of average and maximum time domain amplitude and control current was observed. The *z*-axis response in the time domain (Figure3.21) looks the most different because the magnitude of the high-frequency oscillation is much smaller. Thus, making small changes in average amplitude appear more obvious.

In the IF plots (Figures 3.22 through 3.26), a low frequency noise (1,000 Hz) is now apparent in both the *x*- and *y*-axis but is reduced to zero after about one second. This new
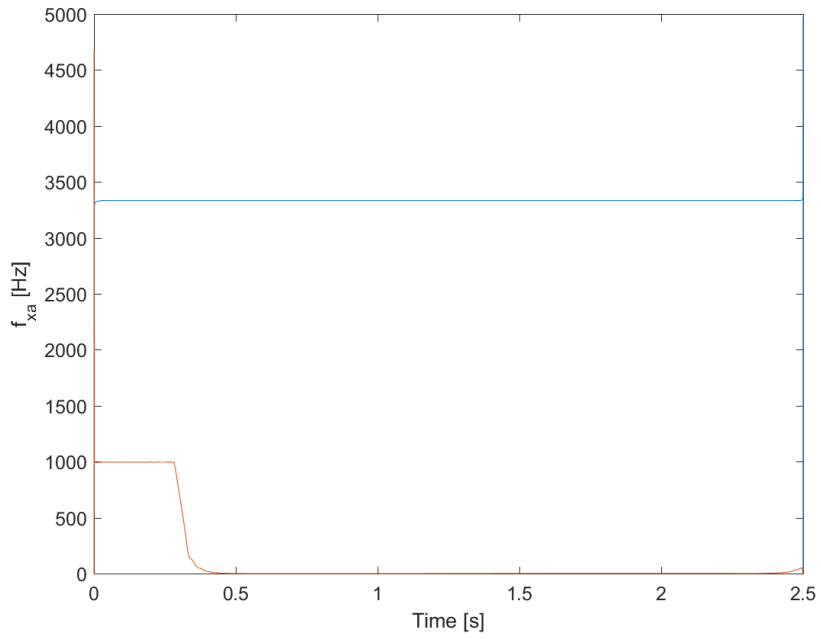
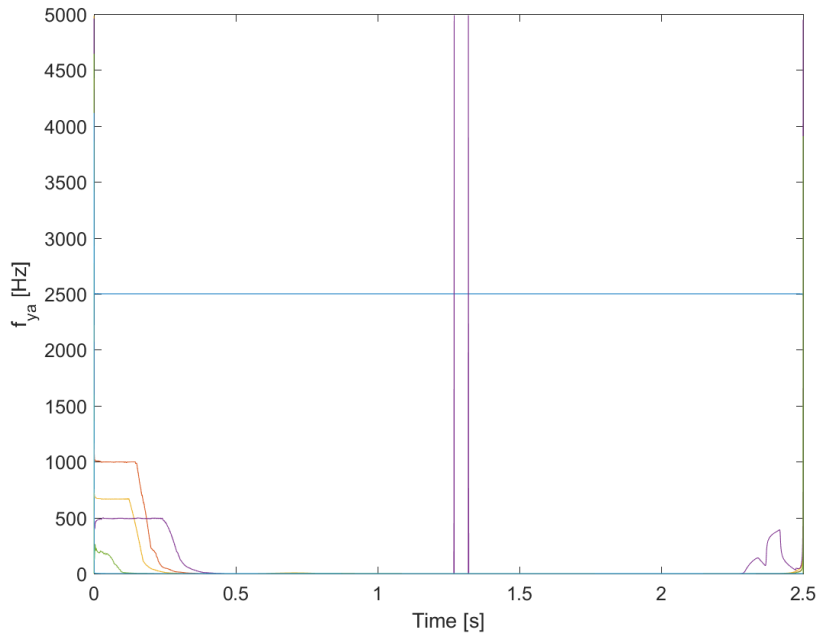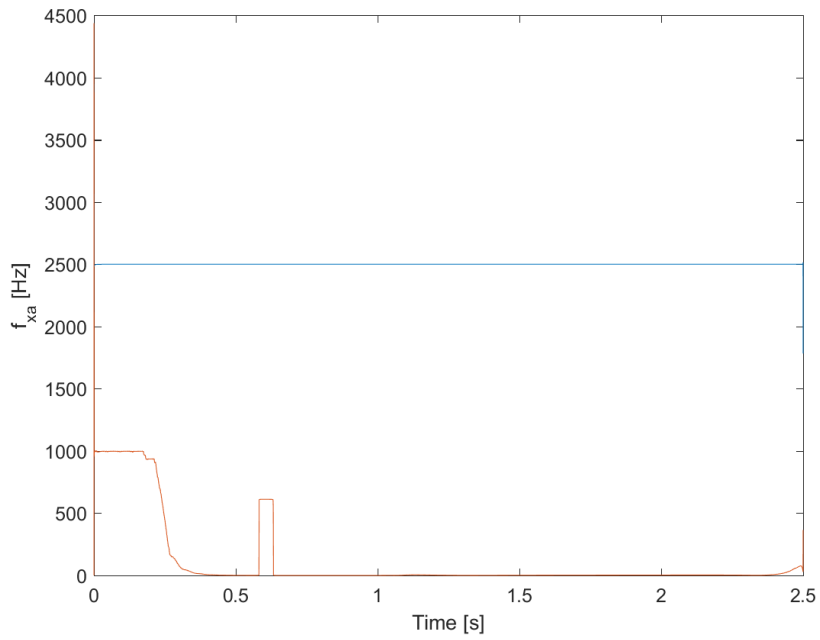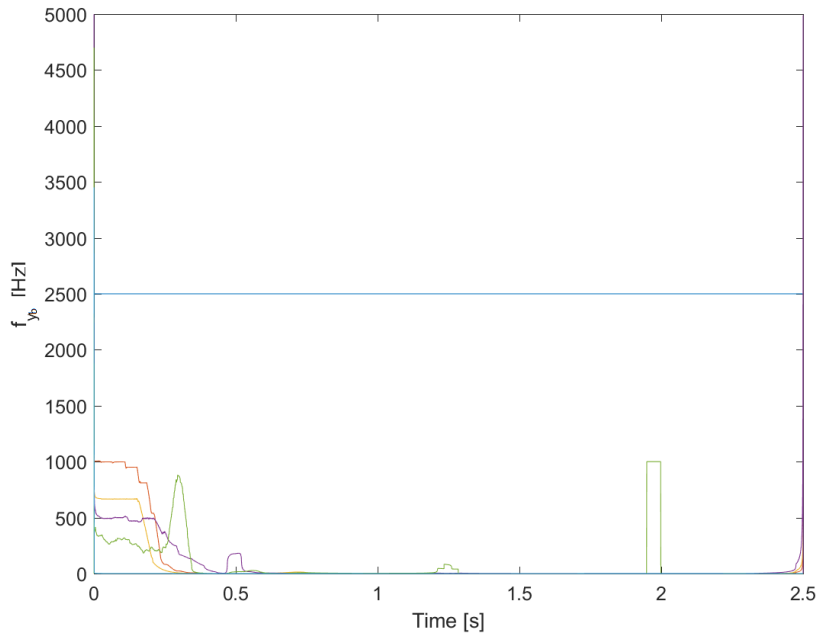Figure 3.23: PID test 3: bearing A IF response for *x*-axis.
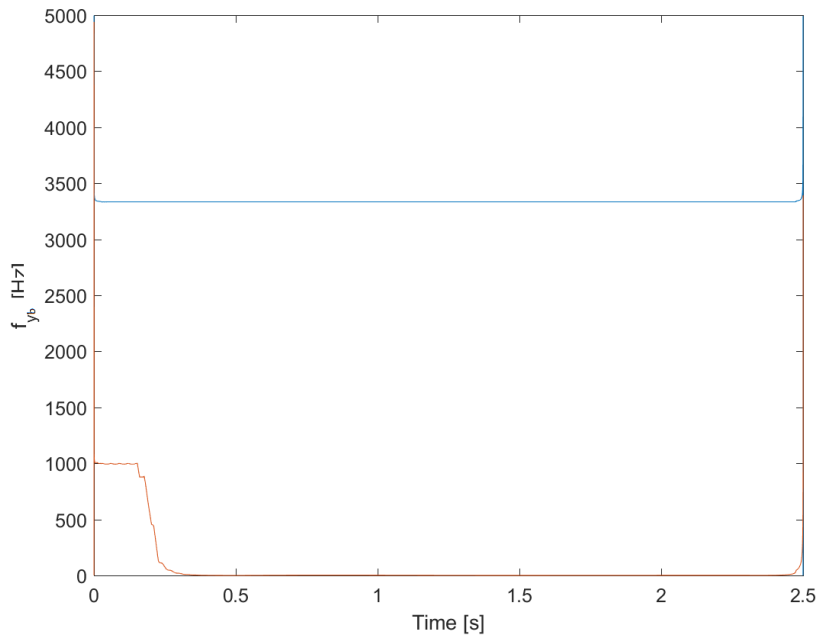
Figure 3.24: PID test 3: bearing B IF response for *y*-axis.
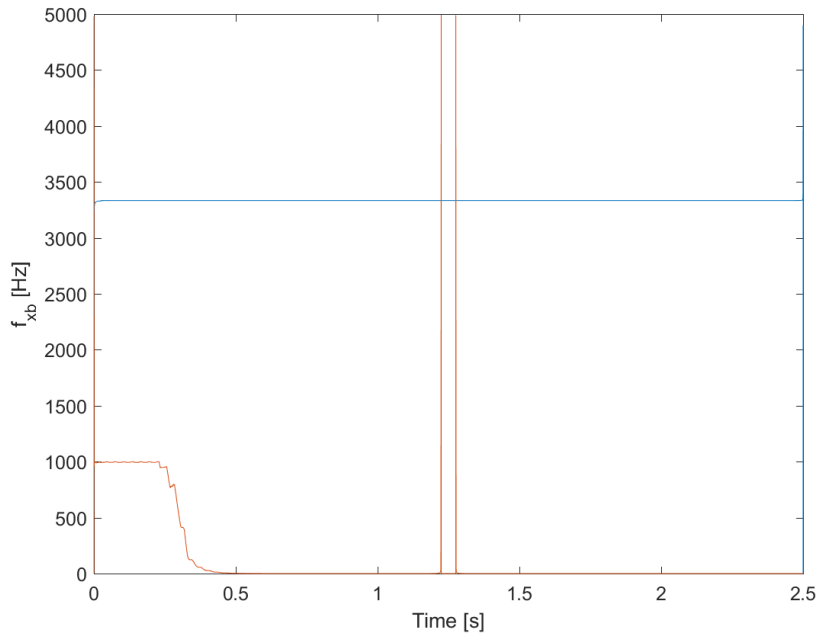
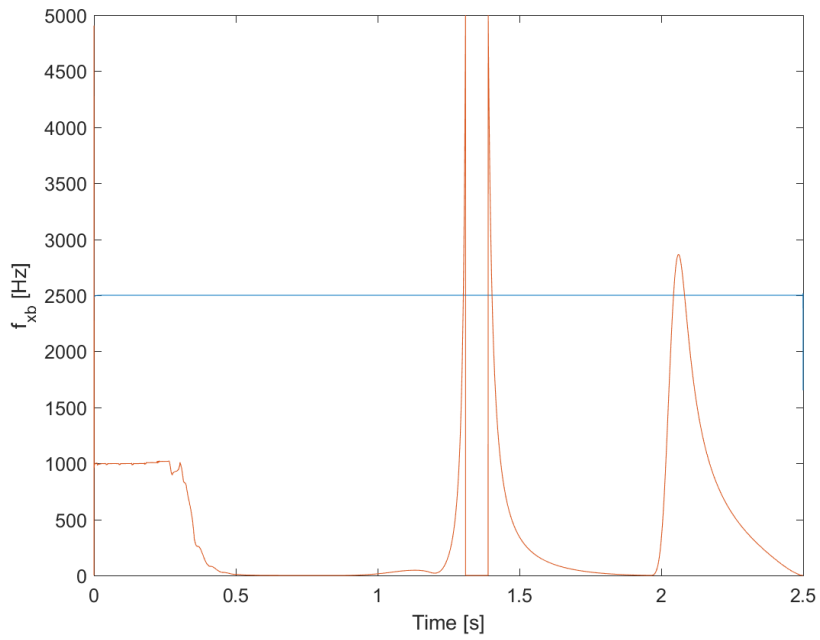Figure 3.25: PID test 3: bearing B IF response for *x*-axis.
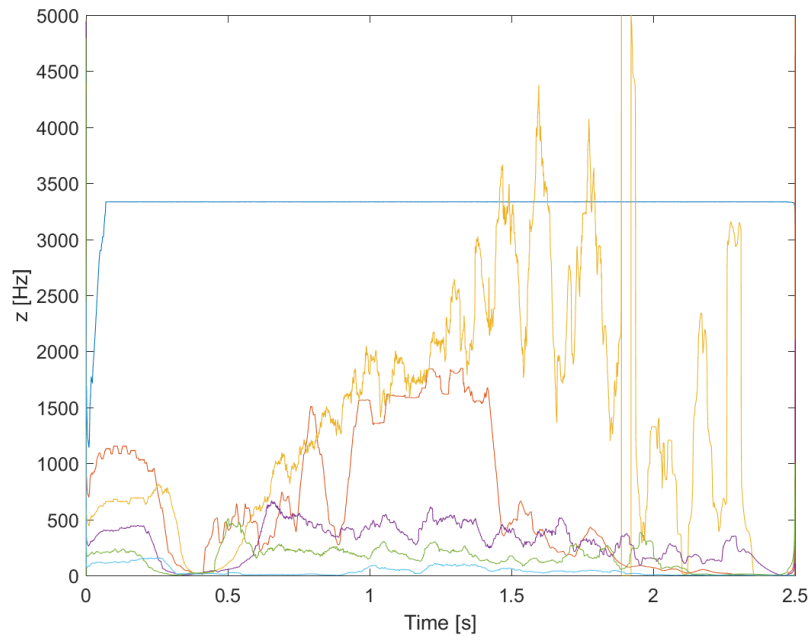
Figure 3.26: PID test 3: thrust bearing IF response.

phenomenon does not seem to challenge the controller as it quickly removes this frequency and achieves steady state in the frequency domain. Where the frequency response looks much less controlled is in the *z*-axis (Figure 3.26). Clearly, increasing the rotating speed has the biggest impact in the frequency domain. The rotor is highly unstable in the *z*-axis with time-varying spectral bandwidth and time-varying frequency components. While this model was still considered well-controlled in the time domain, these new low-frequency modes could excite natural vibration modes in the FES rotor and cause failure. However, the point of these simulations with the PID controller was to demonstrate that this system could be controlled and to give a point of reference when observing the results from the WFXLMS controller.

3.2 Fuzzy Logic Results

The next controller used to verify that the system is controllable and to provide another point of reference is the fuzzy logic controller. Since the PID controller appeared to stabilize the system from 100,000 rpm to 200,000 rpm. The fuzzy logic controller was tested at the extrema of that range.

3.2.1 Test 1

The flywheel parameters used for this test are listed in Table 3.8. The step size for the ODE solver was 1×10^{-6} seconds. From these testing conditions, the average and maximum values for the current and position in Table 3.9 were determined.

The time domain response of the FES system at the three bearings are shown in

Table 3.8: Fuzzy logic test 1 conditions.

Term	Value	Units
ω	100000	rpm
	1667	Hz
e	1	μm
I_{0r}	4	A
I_{0z}	4	A

Table 3.9: Fuzzy logic test 1 results.

Term	Axis	Average	Maximum
Current (A)	x	8.41×10^{-1}	1.92×10^{0}
	y	8.37×10^{-1}	2.32×10^{0}
	z	2.16×10^{-3}	6.41×10^{-2}
Magnitude (m)	x	4.13×10^{-7}	1.07×10^{-6}
	y	4.15×10^{-7}	1.49×10^{-6}
	z	2.68×10^{-7}	2.68×10^{-7}

Figures 3.27 through 3.29.

An instantaneous frequency (IF) plot of each temporal response was generated to evaluate the stability in the frequency domain and is shown in Figures 3.30 through 3.34. The raw data generated for each bearing had significant signal processing noise due to the nature of the IF calculations process. Therefore, a smoothing function was applied to this data to reveal the frequency trends and omit unnecessary data outliers. When comparing the raw plot with the smoothed plot, there was not a noticeable difference in the general trend of the data. Therefore, it is reasonable to assume that these plots do an adequate job depicting the controller's stability in the frequency domain.

Clearly, in the time domain, this controller performs with a much better tolerance and stability than the PID controller. When compared directly with the PID controller at

Figure 3.27: Fuzzy logic test 1: independent bearing A temporal responses.

Figure 3.28: Fuzzy logic test 1: independent bearing B temporal responses.
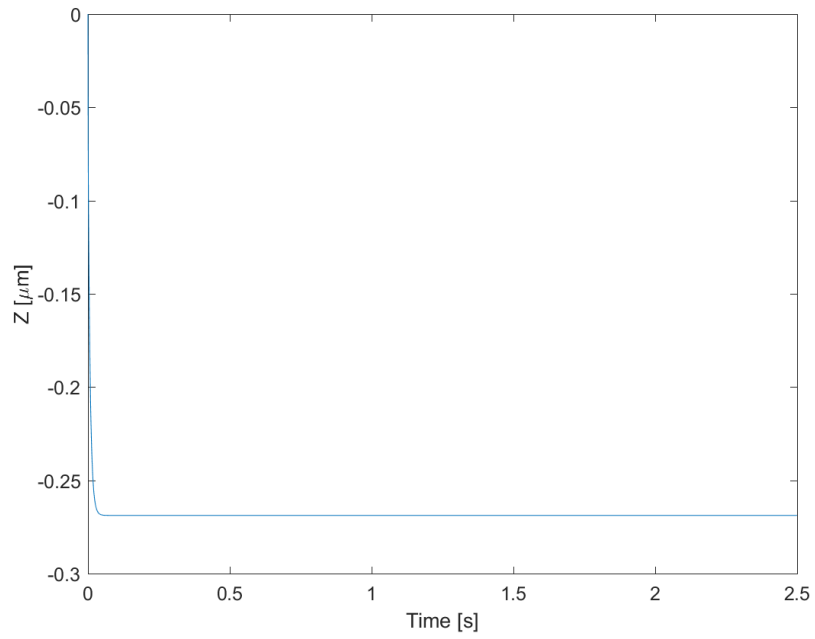
Figure 3.29: Fuzzy logic test 1: thrust bearing.

Figure 3.30: Fuzzy logic test 1: bearing A IF response for *y*-axis.

Figure 3.31: Fuzzy logic test 1: bearing A IF response for *x*-axis.

Figure 3.32: Fuzzy logic test 1: bearing B IF response for *y*-axis.

Figure 3.33: Fuzzy logic test 1: bearing B IF response for *x*-axis.

Figure 3.34: Fuzzy logic test 1: thrust bearing IF response.

the same speed, the fuzzy-logic controller used about 0.2 Amps more average current than the PID and about 0.7 Amps more maximum current in the y-axis to achieve that improved stability. Even more unique is the time domain behavior of the controller in the z-axis. Due to the nature of membership functions, the relatively small error that was achieved with the PID controller was treated as zero error by the fuzzy-logic membership functions. Therefore, the fuzzy-logic controller did not supply adequate current to the thrust bearing until it had reached an error of similar magnitude to that of the x- and y-axis, and, once it did detect an error, it was six orders of magnitude larger than the PID.

Where the controller really suffers is in the frequency domain. This is shown in the IF plots (Figures 3.30 through 3.34). The first mode is the only stable frequency at 1,667 Hz which is the operating speed of the rotor. The lower modes are erratic and unpredictable; primarily for the x- and y-axis. While the z-axis looks stable in the time domain, there are clearly multiple vibration modes with a maximum frequency of about 750 Hz. Based on this results, it can be concluded that the dynamic behavior of the rotor would be completely different for a flexible rotor model as these frequencies could likely induce resonance within the rotor.

3.2.2 Test 2

The flywheel parameters used for this test are listed in Table 3.10. The step size for the ODE solver was 1×10^{-6} seconds. From these testing conditions, the average and maximum values for the current and position in Table 3.11 were determined.

The time domain response of the FES system at the three bearings are shown in

Table 3.10: Fuzzy logic test 2 conditions.

Term	Value	Units
ω	200000	rpm
	3333	Hz
e	1	μm
I_{0r}	4	A
I_{0z}	4	A

Table 3.11: Fuzzy logic test 2 results.

Term	Axis	Average	Maximum
Current (A)	x	1.77×10^0	2.55×10^0
	y	1.84×10^0	3.05×10^0
	z	2.16×10^{-3}	6.41×10^{-2}
Magnitude (m)	x	6.61×10^{-7}	1.39×10^{-6}
	y	1.14×10^{-6}	2.63×10^{-6}
	z	2.68×10^{-7}	2.69×10^{-7}

Figures 3.35 through 3.37.

An instantaneous frequency (IF) plot of each temporal response was generated to evaluate the stability in the frequency domain and is shown in Figures 3.38 through 3.42. The raw data generated for each bearing had significant signal processing noise due to the nature of the IF calculations process. Therefore, a smoothing function was applied to this data to reveal the frequency trends and omit unnecessary data outliers. When comparing the raw plot with the smoothed plot, there was not a noticeable difference in the general trend of the data. Therefore, it is reasonable to assume that these plots do an adequate job depicting the controller's stability in the frequency domain.

This simulation does the best job at demonstrating the effect that gyroscopics has on system stability for the rigid rotor model. While the time domain response was a little less
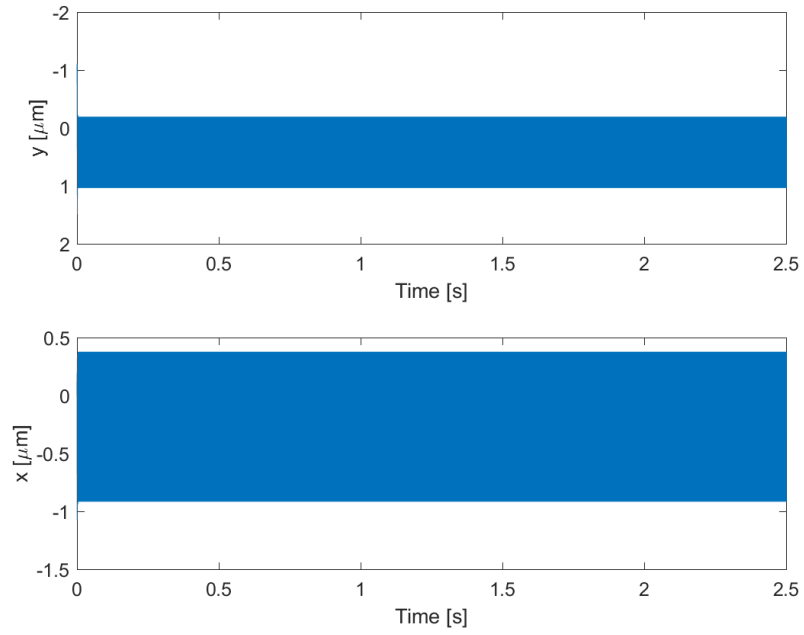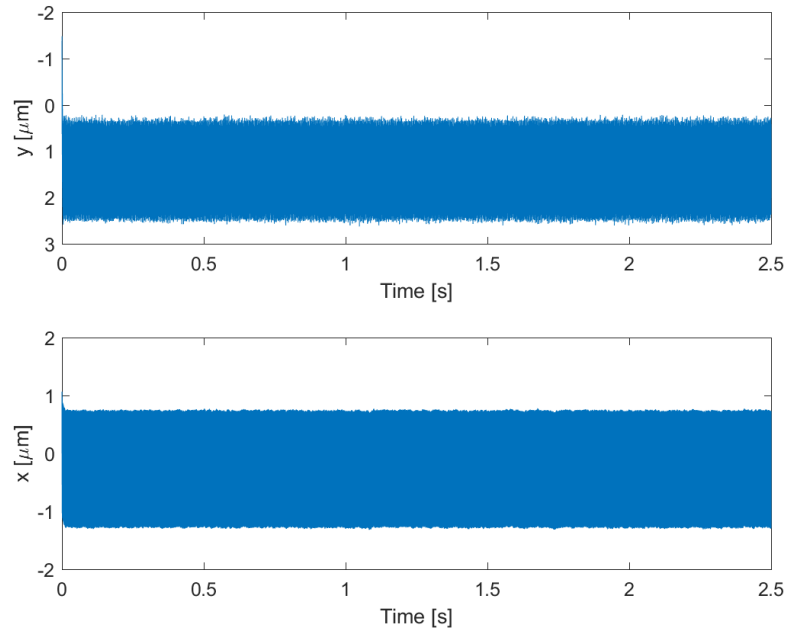
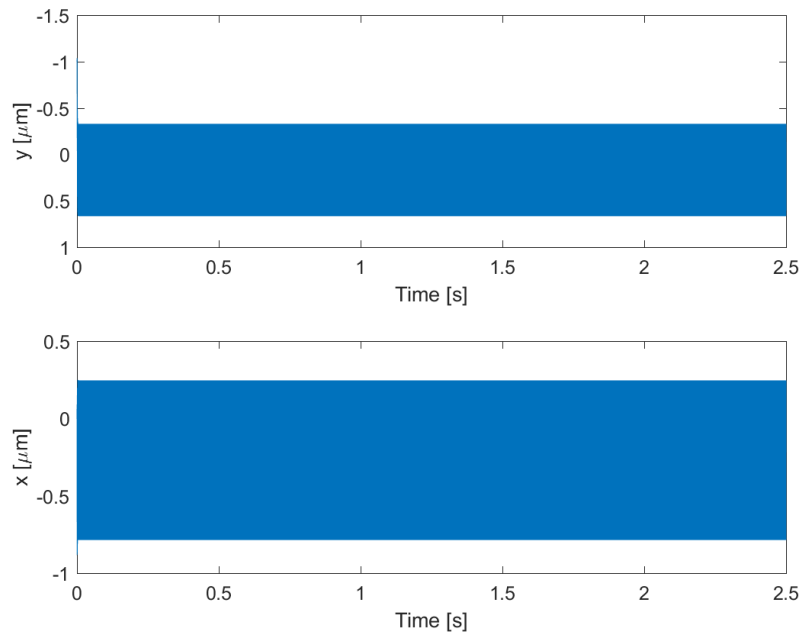Figure 3.35: Fuzzy logic test 2: independent bearing A temporal responses.

Figure 3.36: Fuzzy logic test 2: independent bearing B temporal responses.
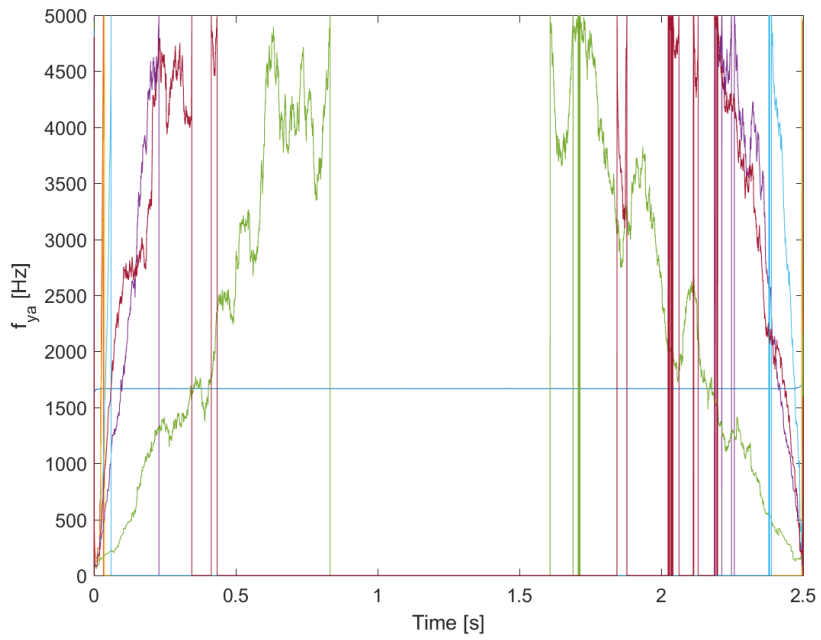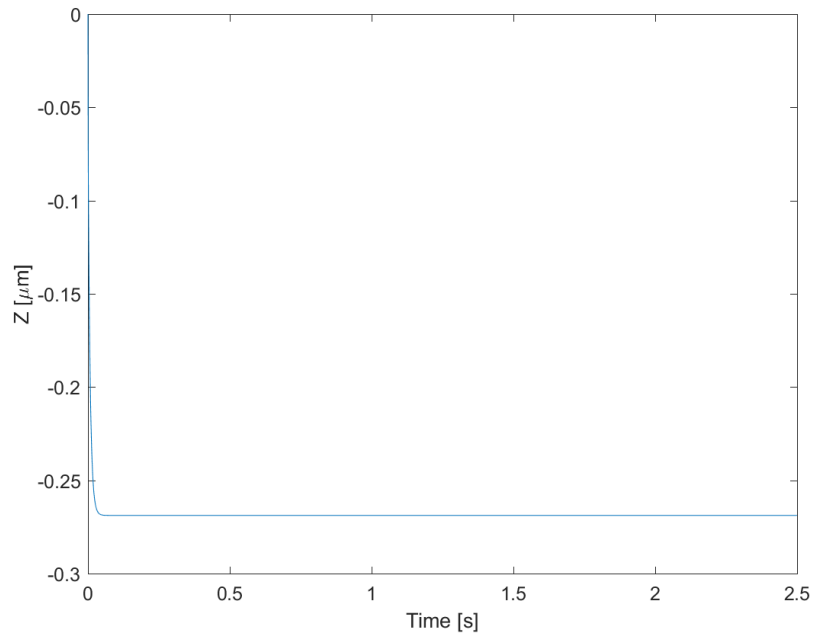
Figure 3.37: Fuzzy logic test 2: thrust bearing.

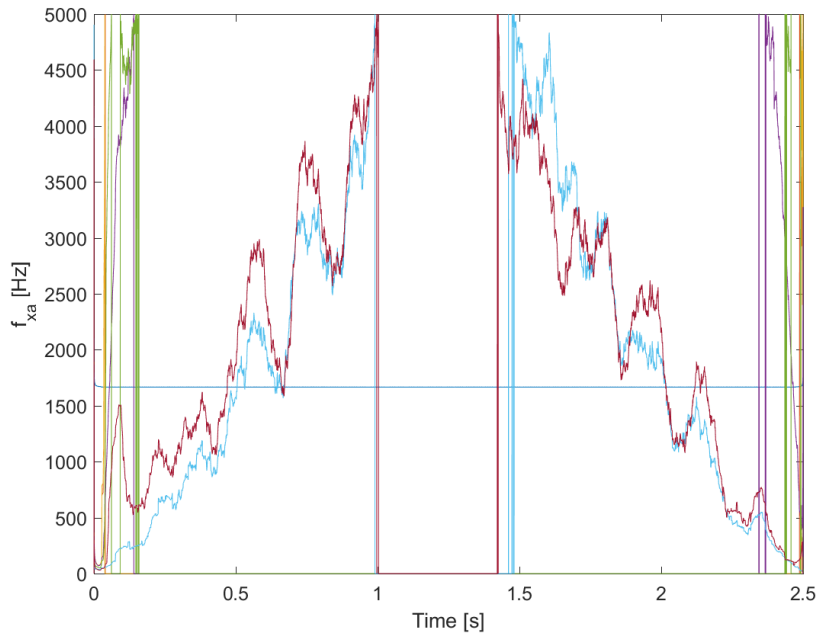Figure 3.38: Fuzzy logic test 2: bearing A IF response for *y*-axis.

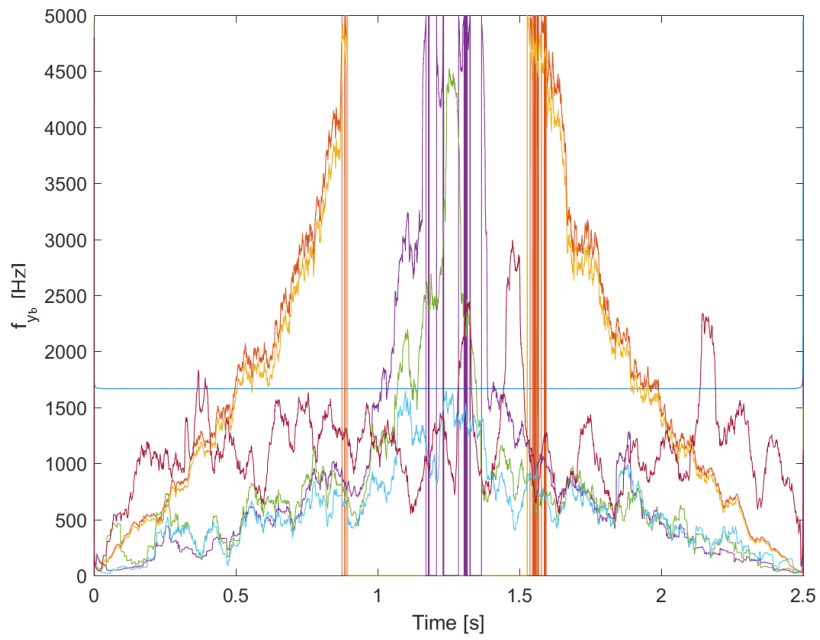Figure 3.39: Fuzzy logic test 2: bearing A IF response for *x*-axis.

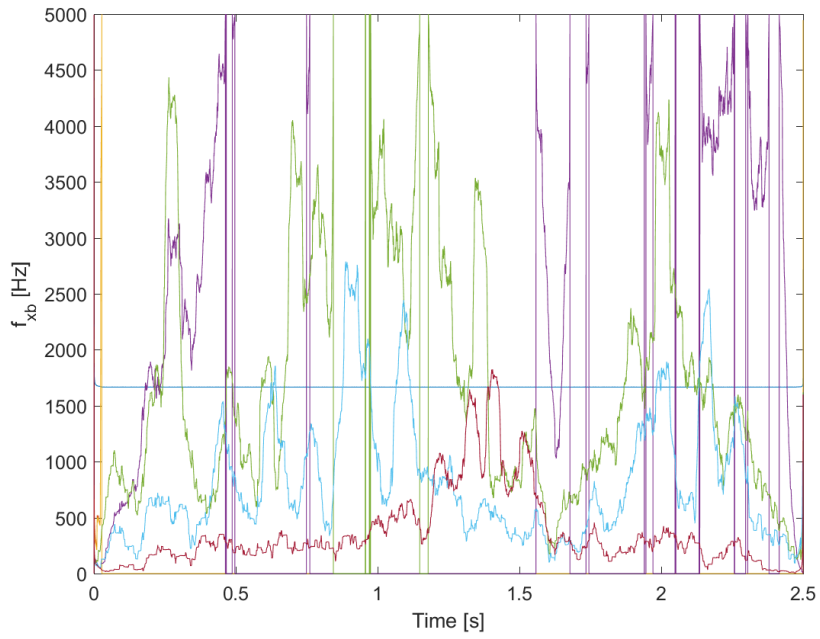Figure 3.40: Fuzzy logic test 2: bearing B IF response for *y*-axis.

Figure 3.41: Fuzzy logic test 2: bearing B IF response for *x*-axis.
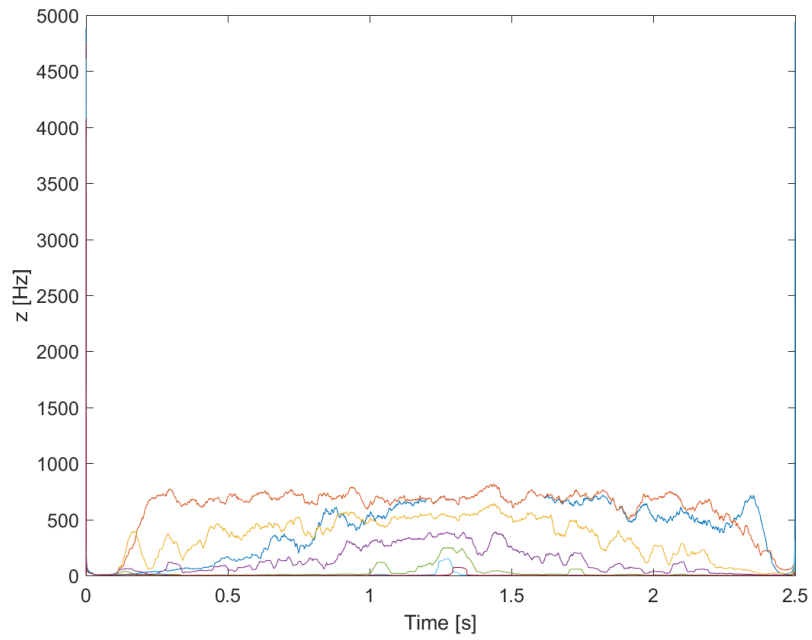

Figure 3.42: Fuzzy logic test 2: thrust bearing IF response.

solid (the outer edges of the time domain response were more jagged) than the previous test, the frequency response is vastly different. Instead of random low frequency mode shifting the lower modes all seems stable and no greater than 1,500 Hz. Clearly, spinning this system at higher rates increases stability instead of decreasing it. However, the IF response from the 0-500 Hz range show frequencies with a temporal-modal structure that is characteristic of a bifurcated, unstable response. The time-domain displacements may seem contained, but the dynamics are technically still unstable.

The average current required to control at 200,000 rpm increased about 1 Amp for the x- and y-axis but stayed the exact same for the z-axis. Similarly, a 0.2 μm increase in average amplitude oscillation was observed but the peak displacement actually decreased slightly.

3.2.3 Test 3

The flywheel parameters used for this test are listed in Table 3.12. The step size for the ODE solver was 1×10^{-5} seconds. From these testing conditions, the average and maximum values for the current and position in Table 3.13 were determined.

Table 3.12: Fuzzy logic test 3 conditions.

Term	Value	Units
ω	100000	rpm
	1667	Hz
e	1	μm
I_{0r}	4	A
I_{0z}	4	A

The time domain response of the FES system at the three bearings are shown in

Table 3.13: Fuzzy logic test 3 results.

Term	Axis	Average	Maximum
	x	1.50×10^0	3.71×10^0
Current (A)	y	1.51×10^0	4.23×10^0
	z	7.66×10^{-1}	1.83×10^0
	x	2.11×10^{-6}	5.81×10^{-6}
Magnitude (m)	y	2.95×10^{-6}	1.05×10^{-5}
	z	1.71×10^{-7}	1.77×10^{-7}

Figures 3.43 through 3.45.
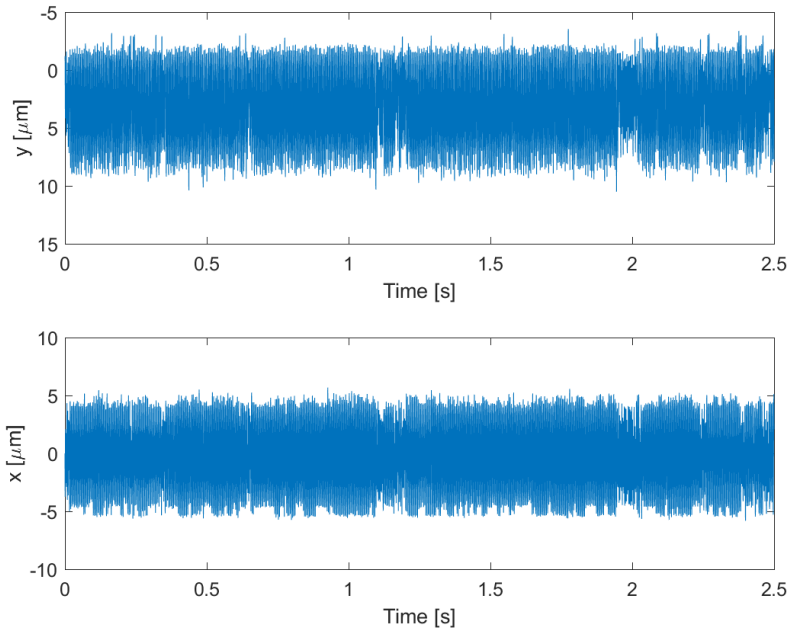
Figure 3.43: Fuzzy logic test 3: independent bearing A temporal responses.

An instantaneous frequency (IF) plot of each temporal response was generated to evaluate the stability in the frequency domain and is shown in Figures 3.46 through 3.50. The raw data generated for each bearing had significant signal processing noise due to the nature of the IF calculations process. Therefore, a smoothing function was applied to this
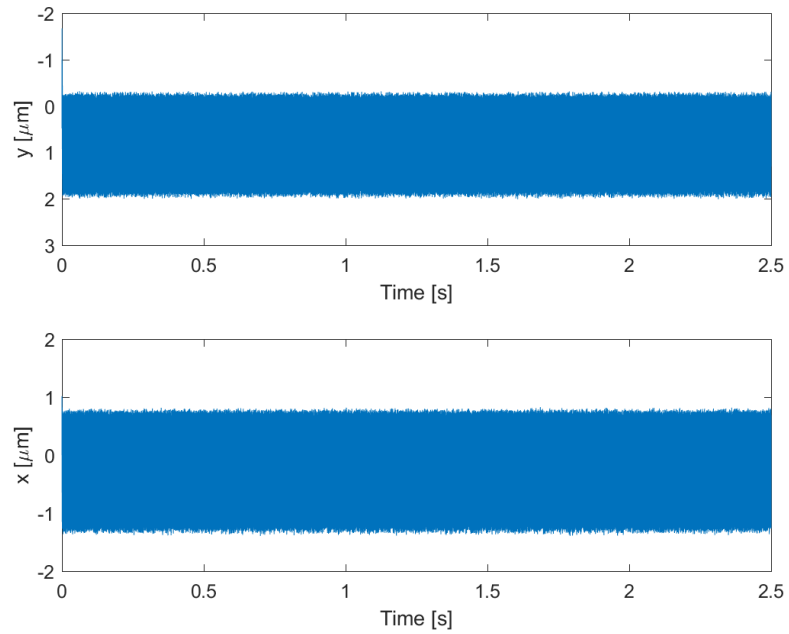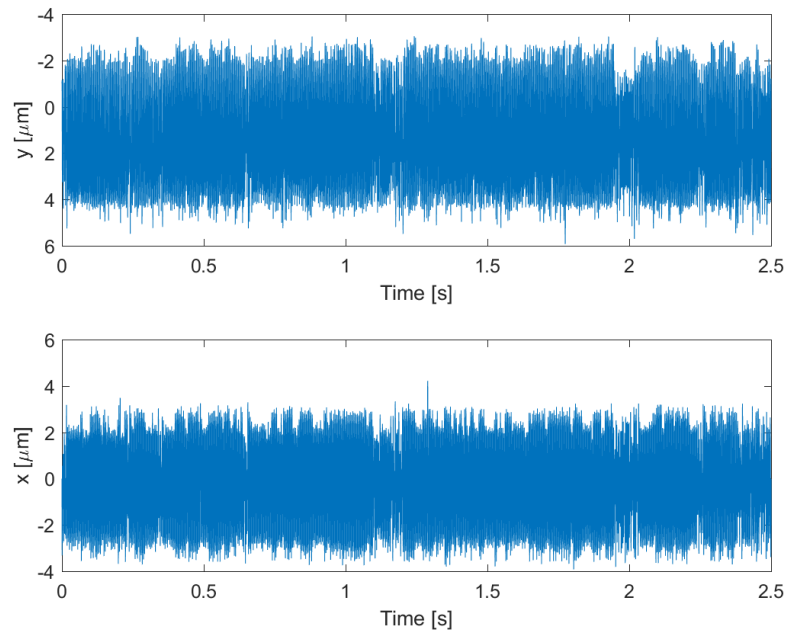
Figure 3.44: Fuzzy logic test 3: independent bearing B temporal responses.
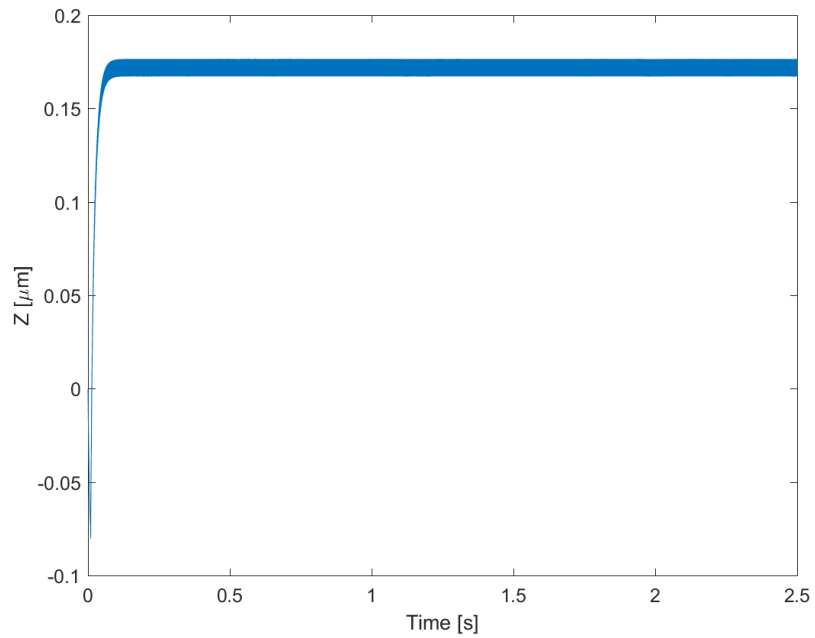
Figure 3.45: Fuzzy logic test 3: thrust bearing.

data to reveal the frequency trends and omit unnecessary data outliers. When comparing the raw plot with the smoothed plot, there was not a noticeable difference in the general trend of the data. Therefore, it is reasonable to assume that these plots do an adequate job depicting the controller's stability in the frequency domain.
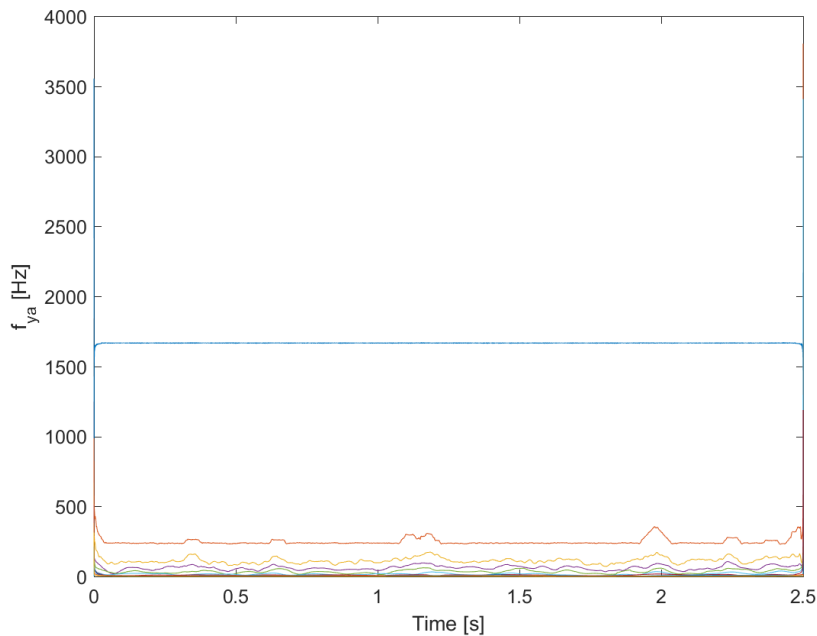
Figure 3.46: Fuzzy logic test 3: bearing A IF response for *y*-axis.

The only difference between this test and test 1 is the differential equation step solver. The dynamic and frequency response of this test is drastically different. This is due to the change-in-error membership function. Because the step size is larger, the calculated rate-of-change of the error is much larger that causes the controller to use much larger currents. On average this controller used double the amount of current as test 1. This is one of the biggest drawbacks to a fuzzy-logic controller; its control efficacy is dependent on the rate
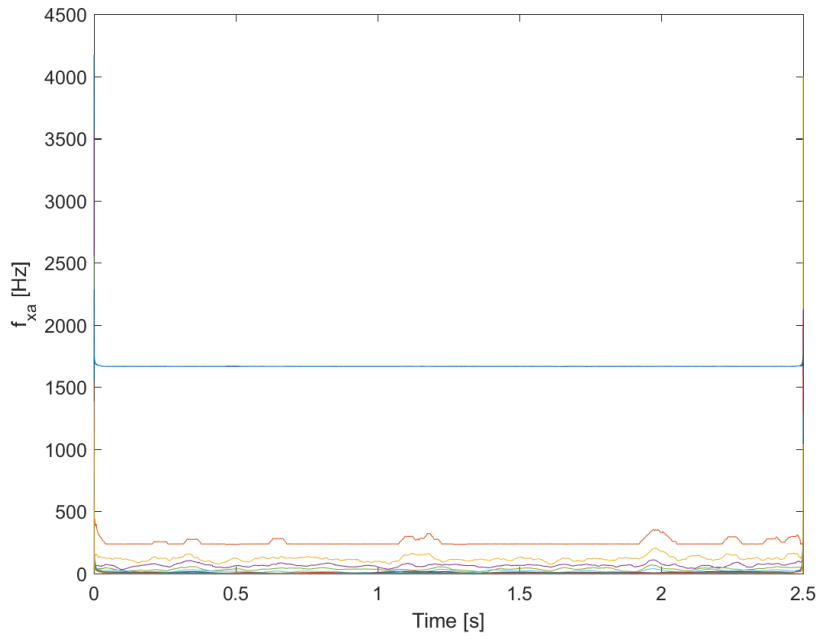
Figure 3.47: Fuzzy logic test 3: bearing A IF response for *x*-axis.
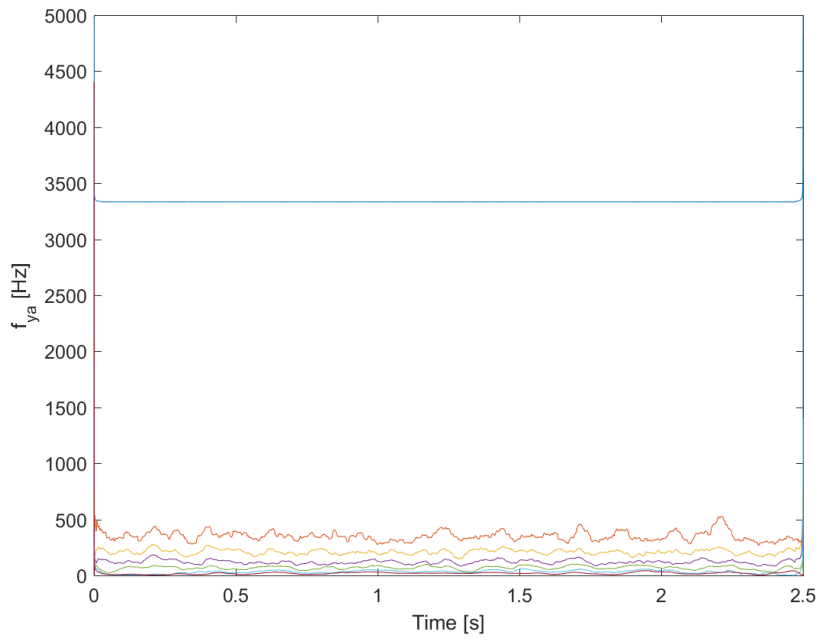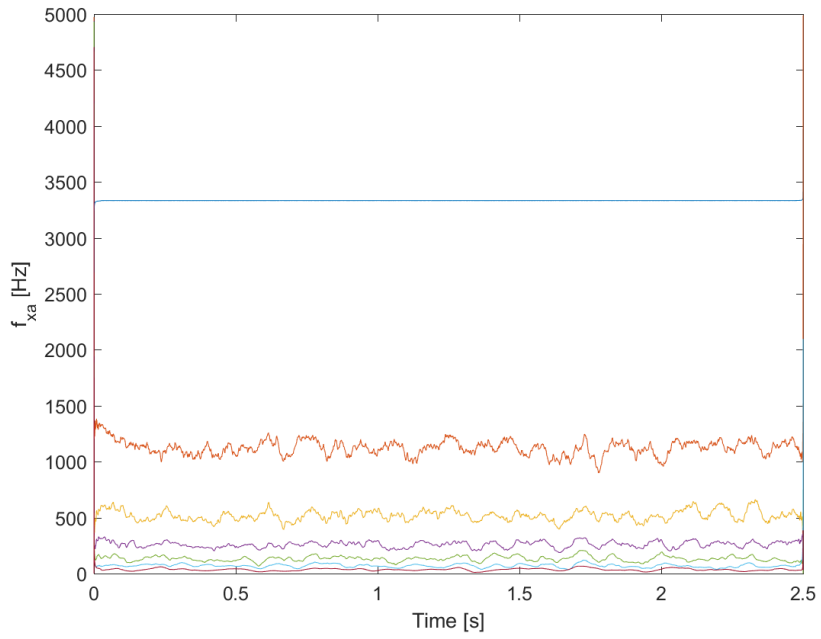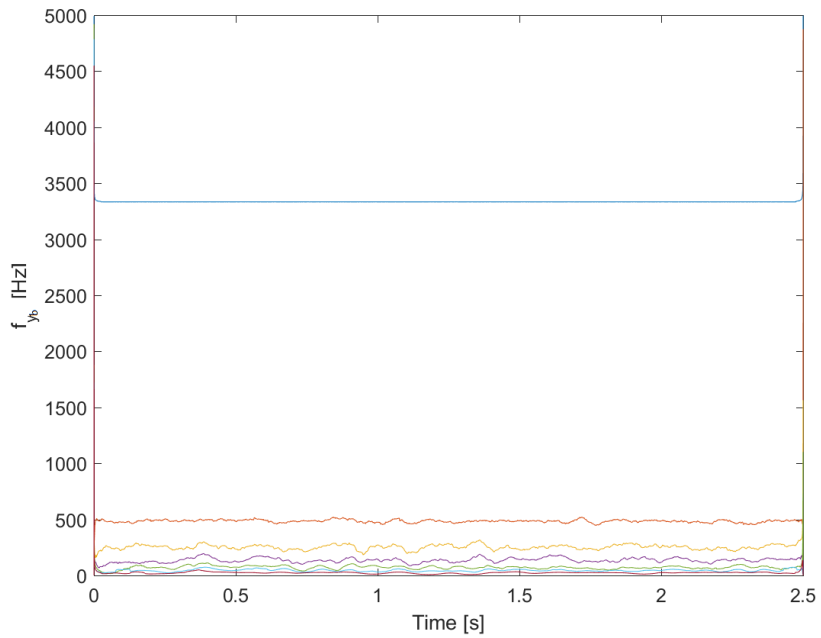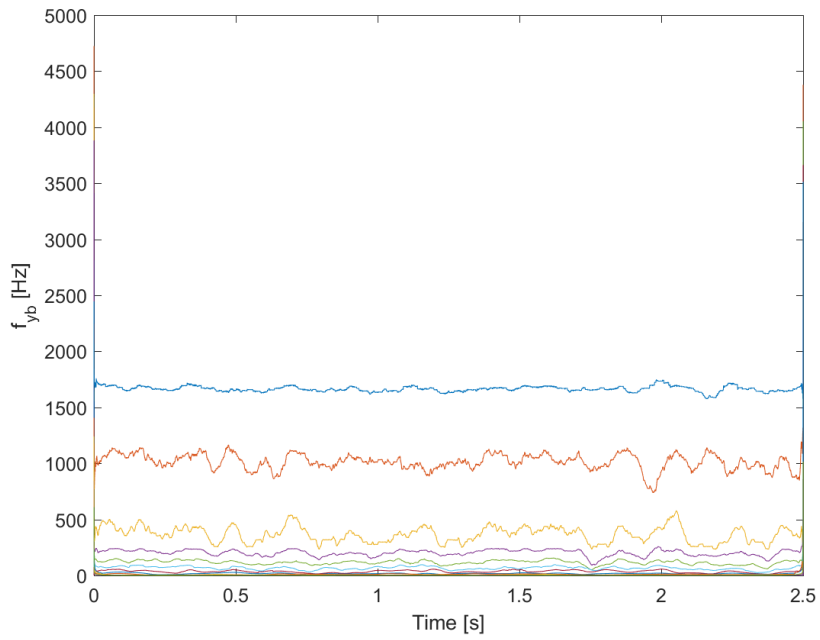

Figure 3.48: Fuzzy logic test 3: bearing B IF response for *y*-axis.
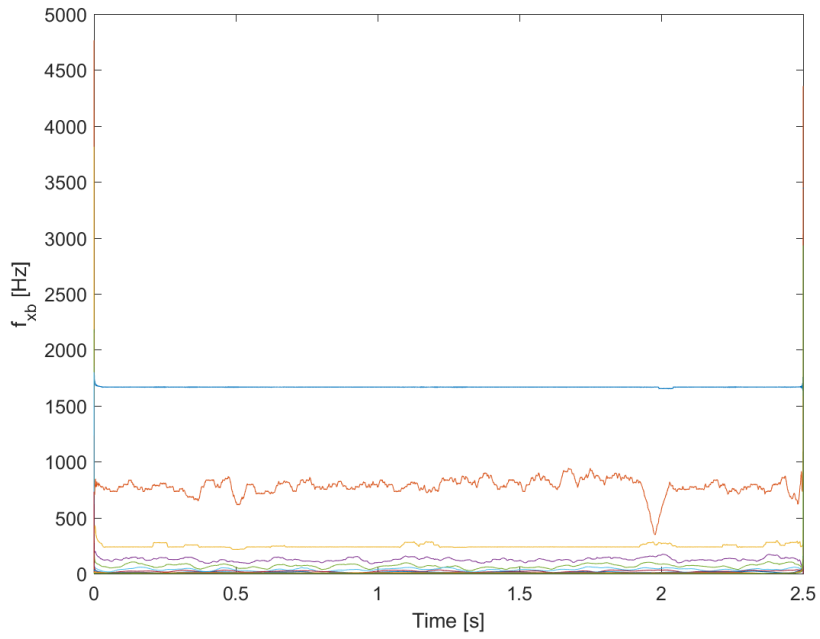
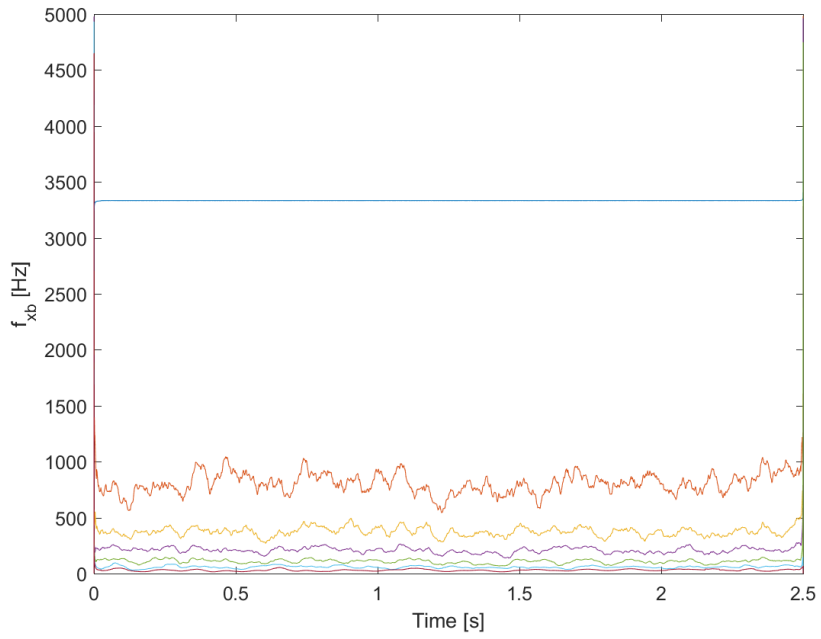Figure 3.49: Fuzzy logic test 3: bearing B IF response for *x*-axis.
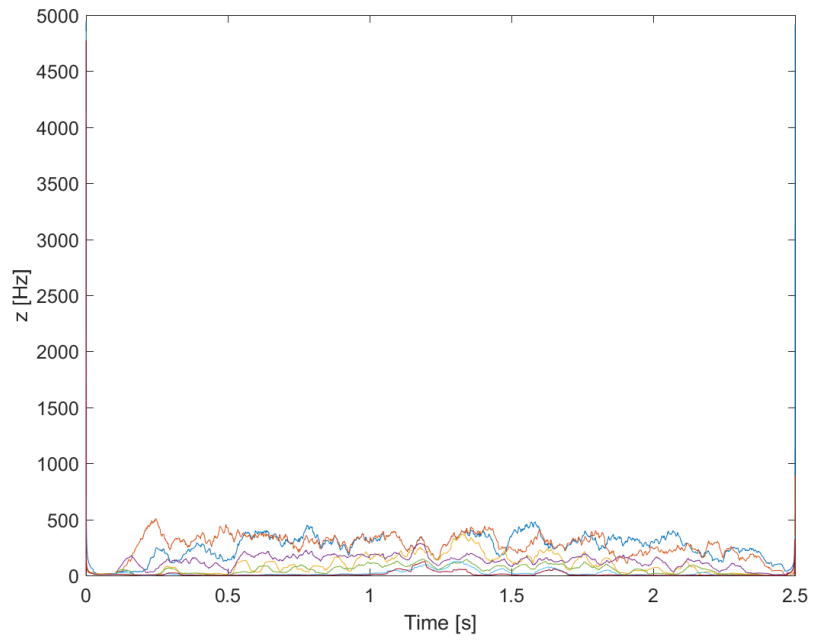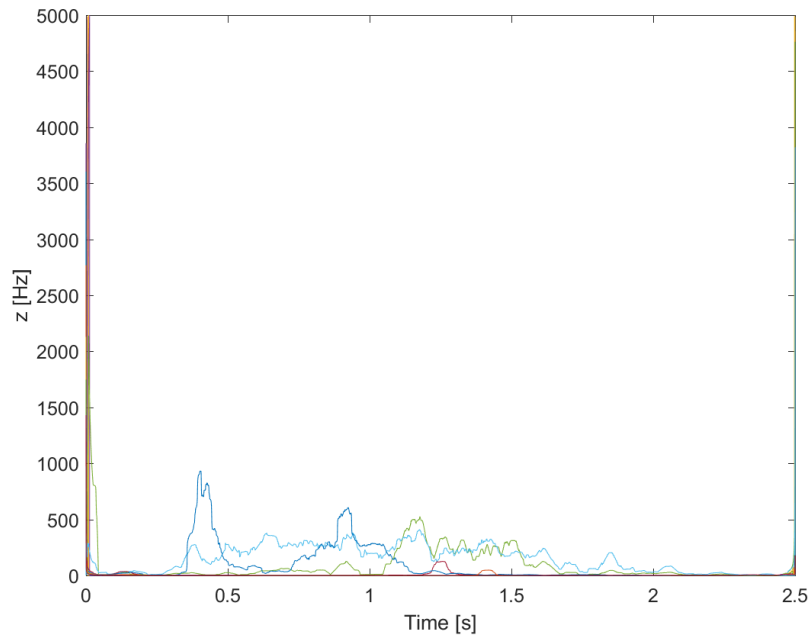

Figure 3.50: Fuzzy logic test 3: thrust bearing IF response.

that data is provided to the controller. This is a bigger problem for real systems. Consider

the case where a position sensor provides data to the controller at an inconsistent rate or that

the sensor periodically skips a measurement. Those instances could cause the controller

to use much larger currents and lead to less dynamic stability. The same test - using a

differential equation solver step size of 1×10^{-5} - was also tested with the PID controller

and that system performed exactly the same regardless of step size.

3.3 WFXLMS Results

Since this controller is brand new, there is not a validated method of determining the

ideal control parameters. Therefore, the following tests demonstrate a range of values that

were tested. The exact range of all the tested parameters are listed in Table 3.15 below.

Table 3.14: WFXLMS testing conditions.

Term	Minimum	Maximum
ω (rpm)	100	100000
dt (s)	5×10^{-7}	1×10^{-5}
I_{0r}	4	10
I_{0z}	4	10
i_{supply}	5	200
$i_{supplyz}$	5	200
N	128	512
eG	-1	1
eGz	-1	1
W1	0.5	5
W1z	0.5	5
μ_1	1×10^{-16}	5×10^{-3}
μ_2	1×10^{-16}	1×10^{-2}
μ_{1z}	1×10^{-16}	5×10^{-3}
μ_{2z}	1×10^{-16}	1×10^{-2}

W1 and W1z are the initial filter values for the journal and thrust bearings, respec-

tively. N is the filter length for the controller. The parameters μ_1, μ_2, μ_{1z}, and μ_{2z} are the filter step sizes for the journal and thrust bearings, respectively. Parameters eG and eGz are arbitrary values that are multiplied to the error and input to the controller for the journal and thrust bearings, respectively. Finally, i_{supply} and $i_{supplyz}$ are the currents that are supplied to a proportional gain that is then used by the controller. In essence, this controller modifies an input signal before it is sent to the FES system and the only method that worked for longer than 0.0005 seconds was if a proportional gain was supplied to the controller. This proportional controller started at 0 Amps when the rotor was at 0 and linearly increased to a maximum value equal to i_{supply} or $i_{supplyz}$ when the rotor was equal to the clearance gap.

3.3.1 Test 1

The flywheel parameters used for this test are listed in Table 3.15. From these testing conditions, the average and maximum values for the current and position in Table 3.16 were determined.

The time domain response of the FES system at the three bearings are shown in Figures 3.51 through 3.53.

An instantaneous frequency (IF) plot of each temporal response was generated to evaluate the stability in the frequency domain and is shown in Figures 3.54 through 3.58. The raw data generated for each bearing had significant signal processing noise due to the nature of the IF calculations process. Therefore, a smoothing function was applied to this data to reveal the frequency trends and omit unnecessary data outliers. When comparing

Table 3.15: WFXLMS test 1 conditions.

Term	Value	Units
ω	100000	rpm
	1667	Hz
dt	1×10^{-6}	s
I_{0r}	4	A
I_{0z}	4	A
i_{supply}	12	A
$i_{supplyz}$	12	A
N	512	
eG	1	
eGz	1	
W1	5	
W1z	5	
μ_1	5×10^{-3}	
μ_2	5×10^{-3}	
μ_{1z}	5×10^{-3}	
μ_{2z}	5×10^{-3}	
t_{end}	1.248	
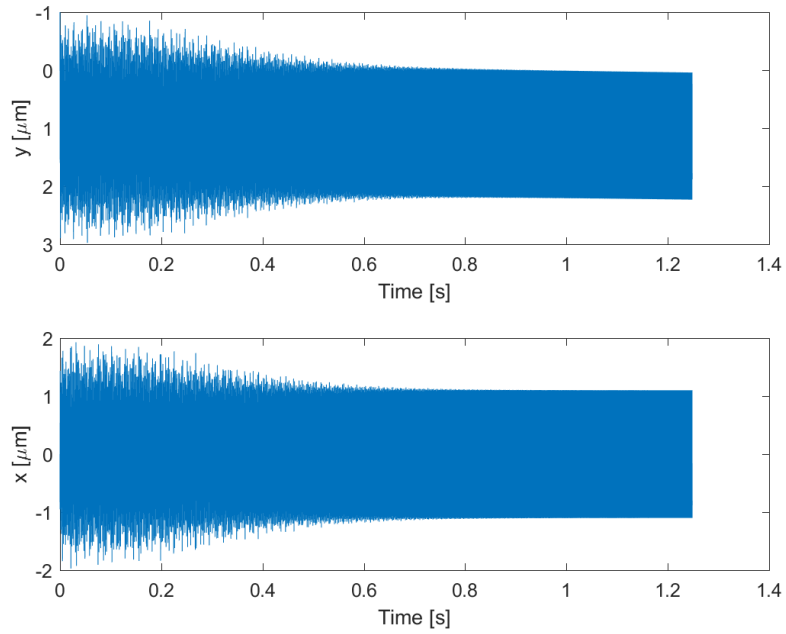
Figure 3.51: WFXLMS test 1: independent bearing A temporal responses.

Table 3.16: WFXLMS test 1 results.

Term	Axis	Average	Maximum
	x	1.51×10^{-1}	4.43×10^{-1}
Current (A)	y	2.03×10^{-1}	6.29×10^{-1}
	z	2.39×10^{-8}	1.25×10^{-7}
	x	7.22×10^{-7}	2.09×10^{-6}
Magnitude (m)	y	9.98×10^{-7}	2.98×10^{-6}
	z	1.41×10^{-13}	7.39×10^{-13}
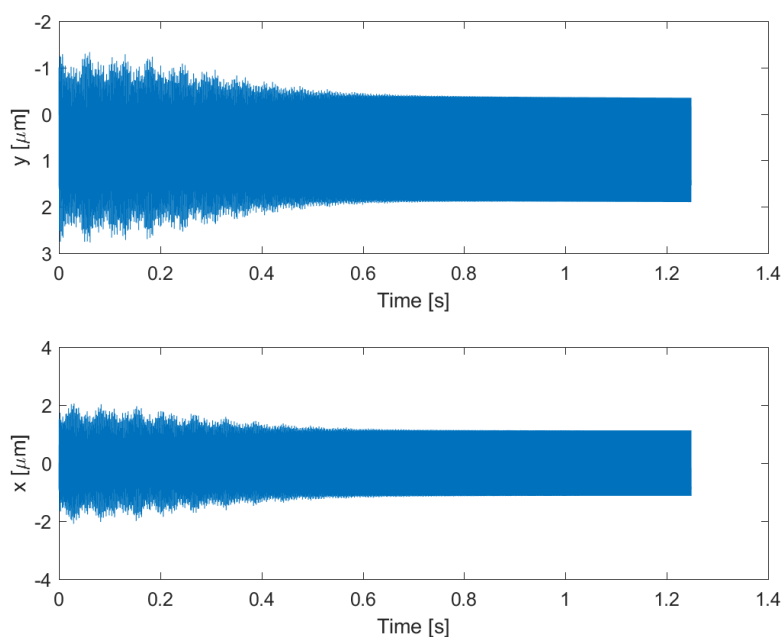
Figure 3.52: WFXLMS test 1: independent bearing B temporal responses.

the raw plot with the smoothed plot, there was not a noticeable difference in the general trend of the data. Therefore, it is reasonable to assume that these plots do an adequate job depicting the controller's stability in the frequency domain.

The only outside information that was used in the first test was the values for current used in the PID and fuzzy-logic tests. Essentially, the parameters i_{supply} and $i_{supplyz}$ were selected to try and get the current used by the WFXLMS controller to resemble that of the

74

Figure 3.53: WFXLMS test 1: thrust bearing.

Figure 3.54: WFXLMS test 1: bearing A IF response for *y*-axis.

Figure 3.55: WFXLMS test 1: bearing A IF response for *x*-axis.

Figure 3.56: WFXLMS test 1: bearing B IF response for *y*-axis.

Figure 3.57: WFXLMS test 1: bearing B IF response for *x*-axis.
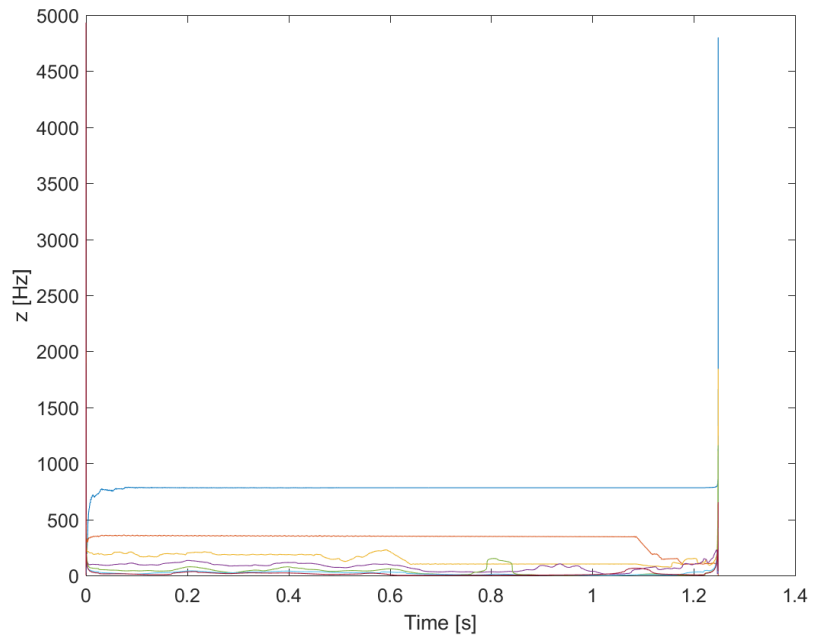
Figure 3.58: WFXLMS test 1: thrust bearing IF response.

previous controllers. Recalling that the fuzzy-logic controller used as much as 2.32 Amps and the PID controller used as much as 1.8 Amps at 100,000 rpm, the maximum current draw of 0.63 Amps was much less than the other controllers. Clearly, the current supplied to the proportional controller needed to be increased for the next test.

This first test reveals the effective control that WFXLMS has in the frequency domain. All of the IF plots, including the z-axis (Figure 3.58), are relatively steady for the duration of the test. However, despite this control in the frequency domain, it seems that the controller is failing in the time domain. Notice the y-axis plots in Figures 3.51 and 3.52 are slowing drifting away from 0 as the influences of gravity take effect. Also, even though the z-axis amplitude of vibration is still pretty small, the thrust bearing is clearly diverging, and, at the very least, is performing much worse than either the PID or the fuzzy-logic controller over the same duration of time. By one second in both the PID and fuzzy-logic results, the z-axis has already reached some form of steady state in the time domain.

3.3.2 Test 2

The flywheel parameters used for this test are listed in Table 3.17. From these testing conditions, the average and maximum values for the current and position in Table 3.18 were determined.

The time domain response of the FES system at the three bearings are shown in Figures 3.59 through 3.61.

An instantaneous frequency (IF) plot of each temporal response was generated to evaluate the stability in the frequency domain and is shown in Figures 3.62 through 3.66.

Table 3.17: WFXLMS test 2 conditions.

| Term	Value	Units
ω	100000	rpm
	1667	Hz
dt	1×10^{-6}	s
I_{0r}	4	A
I_{0z}	4	A
i_{supply}	16	A
$i_{supplyz}$	16	A
N	512	
eG	-1	
eGz	-1	
W1	5	
W1z	5	
μ_1	1×10^{-8}	
μ_2	1×10^{-8}	
μ_{1z}	1×10^{-8}	
μ_{2z}	1×10^{-8}	
t_{end}	1.282	

Figure 3.59: WFXLMS test 2: independent bearing A temporal responses.

Table 3.18: WFXLMS test 2 results.

Term	Axis	Average	Maximum
	x	3.47×10^{-1}	1.68×10^{0}
Current (A)	y	3.79×10^{-1}	1.75×10^{0}
	z	1.02×10^{-8}	8.38×10^{-8}
	x	1.23×10^{-6}	5.94×10^{-6}
Magnitude (m)	y	1.34×10^{-6}	6.19×10^{-6}
	z	4.49×10^{-14}	3.70×10^{-13}
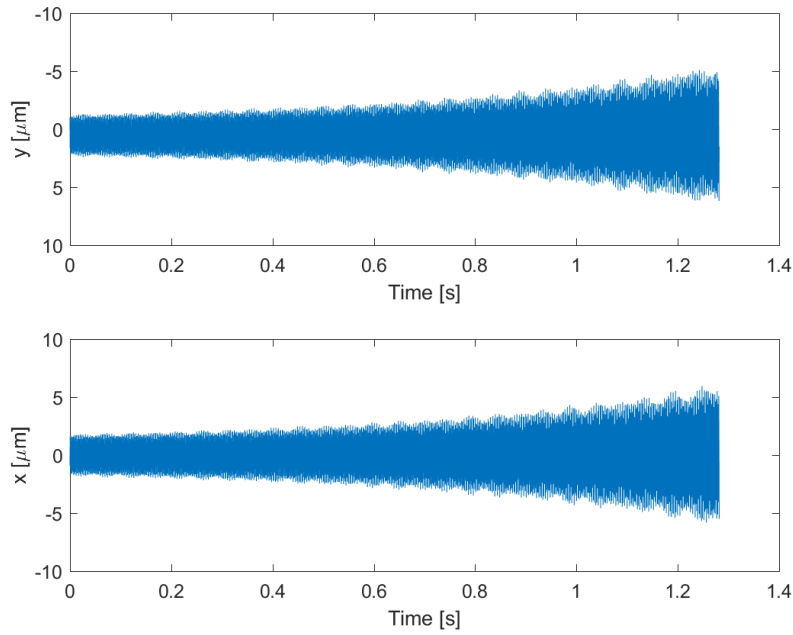
Figure 3.60: WFXLMS test 2: independent bearing B temporal responses.

The raw data generated for each bearing had significant signal processing noise due to the nature of the IF calculations process. Therefore, a smoothing function was applied to this data to reveal the frequency trends and omit unnecessary data outliers. When comparing the raw plot with the smoothed plot, there was not a noticeable difference in the general trend of the data. Therefore, it is reasonable to assume that these plots do an adequate job depicting the controller's stability in the frequency domain.
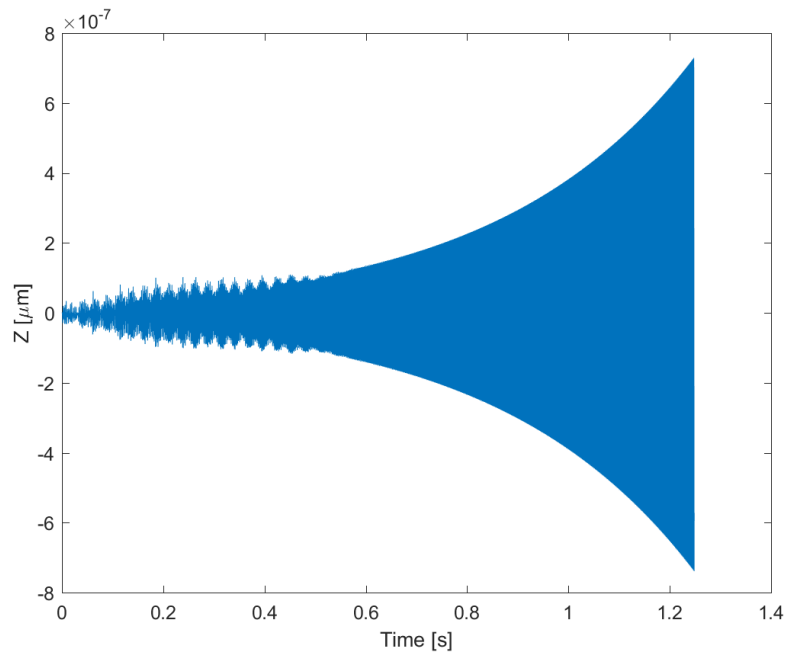
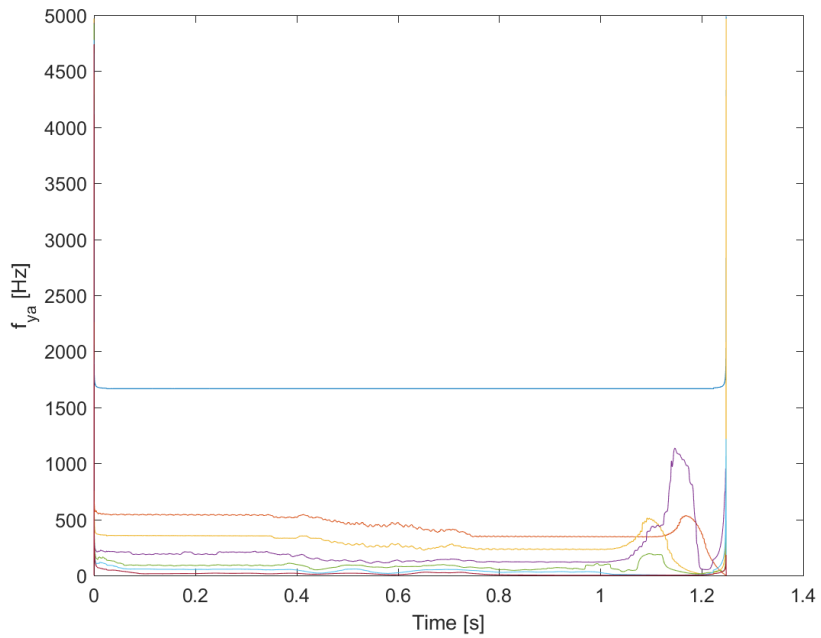Figure 3.61: WFXLMS test 2: thrust bearing.

Figure 3.62: WFXLMS test 2: bearing A IF response for *y*-axis.
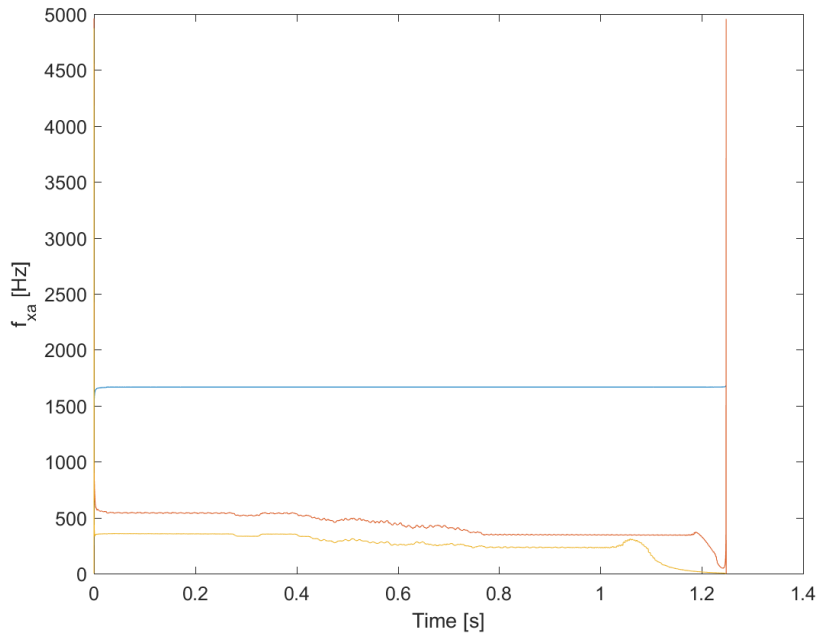
Figure 3.63: WFXLMS test 2: bearing A IF response for *x*-axis.
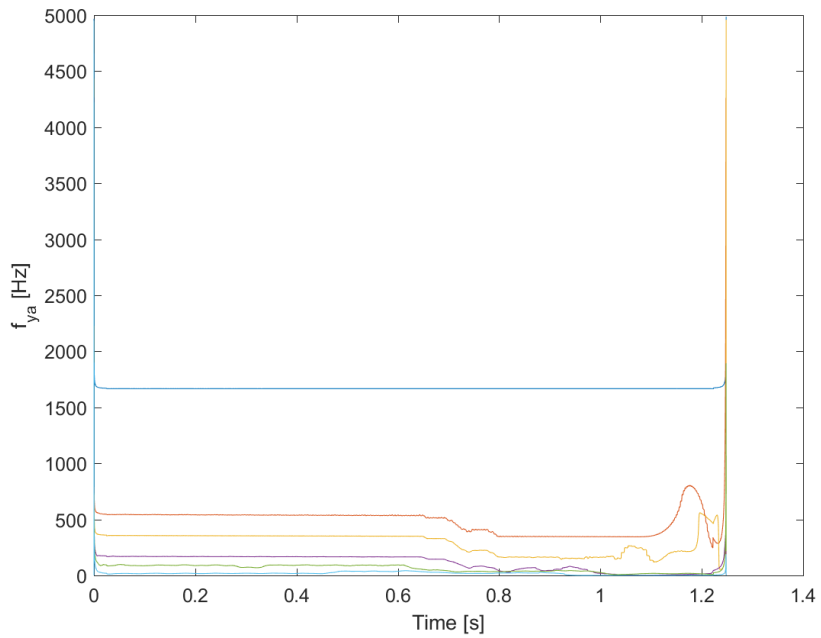

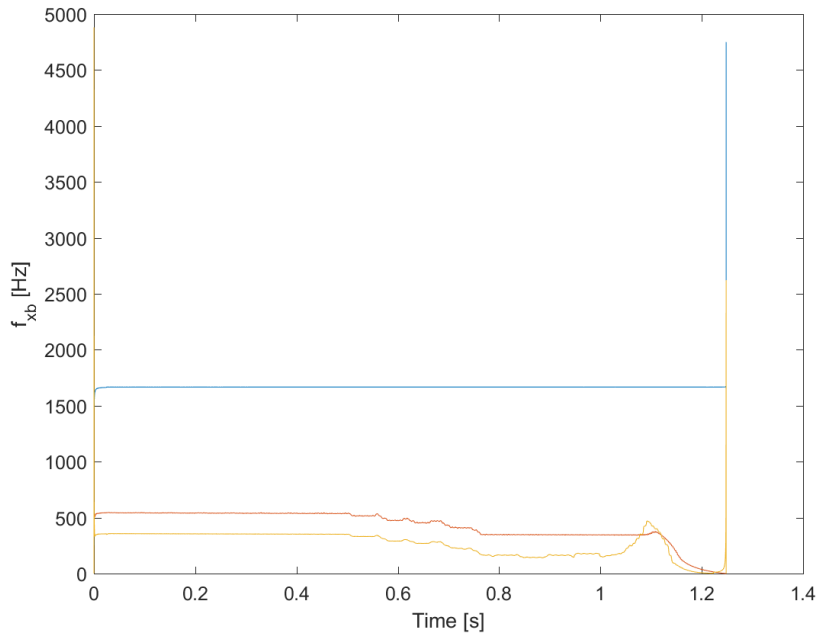Figure 3.64: WFXLMS test 2: bearing B IF response for *y*-axis.

Figure 3.65: WFXLMS test 2: bearing B IF response for *x*-axis.
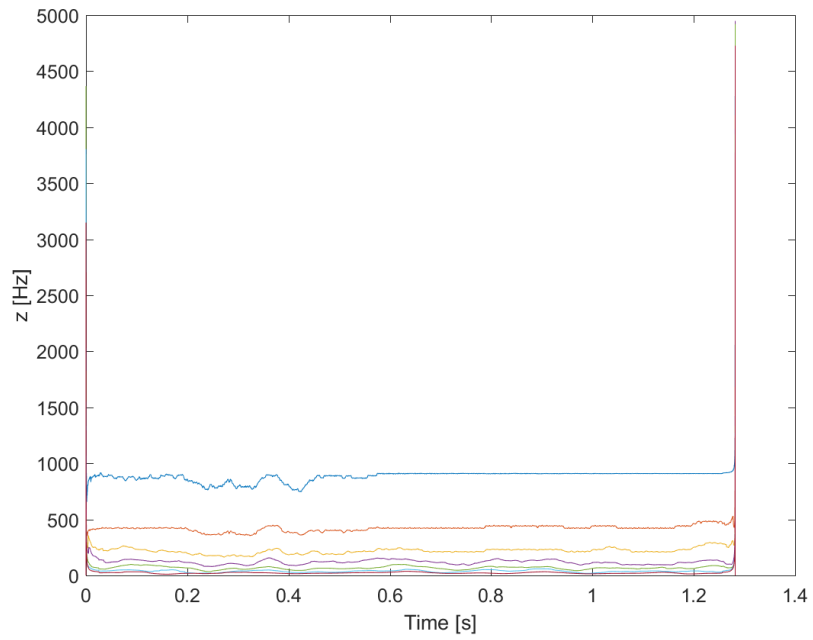
Figure 3.66: WFXLMS test 2: thrust bearing IF response.

The ideas for this test included: to make the filter step size smaller (from 5×10^{-3} to 1×10^{-8}) and see if it was possible that the controller was overstepping some high-frequency component. To see if reversing the error input to the controller (eG) had any impact on performance, and if increasing the supply current would prevent the drifting seen in the previous test (and possibly match either PID or fuzzy-logic current draw). The frequency results for this test seem to demonstrate even more stable results than the previous test. However, the increase in supply current (i_{supply} and $i_{supplyz}$) did not seem to impact the average displacement from 0 in the y-axis compared to the first test (9.98×10^{-7} in test 1 compared to 1.34×10^{-6} in test 2), but did increase the maximum average current draw from 0.2 to 0.38 Amps (still much smaller than PID or fuzzy-logic controllers). Changing all of these parameters did improve the stability of the frequency response, but the response in the x- and y-axis are still diverging one second into the simulation; much worse than last time.

3.3.3 Test 3

The flywheel parameters used for this test are listed in Table 3.19. From these testing conditions, the average and maximum values for the current and position in Table 3.20 were determined.

The time domain response of the FES system at the three bearings are shown in Figures 3.67 through 3.69.

An instantaneous frequency (IF) plot of each temporal response was generated to evaluate the stability in the frequency domain and is shown in Figures 3.70 through 3.74.

Table 3.19: WFXLMS test 3 conditions.

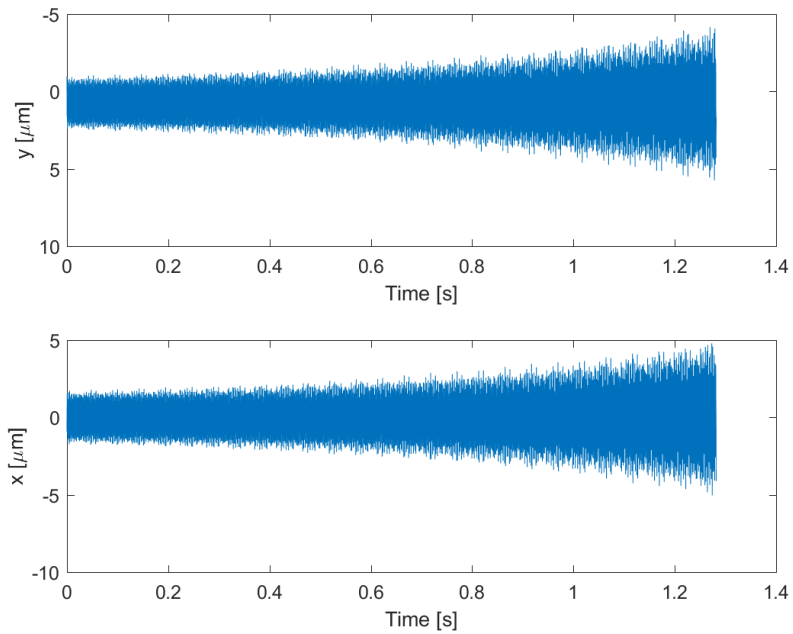| Term	Value	Units
ω	100000	rpm
	1667	Hz
dt	1×10^{-6}	s
I_{0r}	4	A
I_{0z}	4	A
i_{supply}	16	A
$i_{supplyz}$	16	A
N	512	
eG	1	
eGz	1	
W1	5	
W1z	5	
μ_1	1×10^{-8}	
μ_2	1×10^{-8}	
μ_{1z}	1×10^{-8}	
μ_{2z}	1×10^{-8}	
t_{end}	1.278	

Figure 3.67: WFXLMS test 3: independent bearing A temporal responses.

Table 3.20: WFXLMS test 3 results.

| Term	Axis	Average	Maximum
Current (A)	x	3.47×10^{-1}	1.68×10^{0}
	y	3.77×10^{-1}	1.74×10^{0}
	z	1.01×10^{-8}	8.09×10^{-8}
Magnitude (m)	x	1.22×10^{-6}	5.94×10^{-6}
	y	1.33×10^{-6}	6.15×10^{-6}
	z	4.45×10^{-14}	3.58×10^{-13}
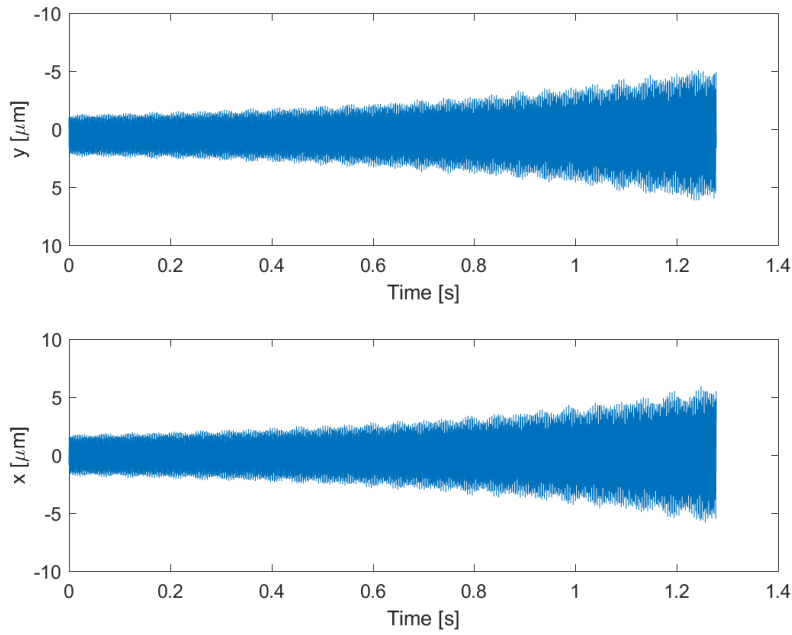
Figure 3.68: WFXLMS test 3: independent bearing B temporal responses.

The raw data generated for each bearing had significant signal processing noise due to the nature of the IF calculations process. Therefore, a smoothing function was applied to this data to reveal the frequency trends and omit unnecessary data outliers. When comparing the raw plot with the smoothed plot, there was not a noticeable difference in the general trend of the data. Therefore, it is reasonable to assume that these plots do an adequate job depicting the controller's stability in the frequency domain.
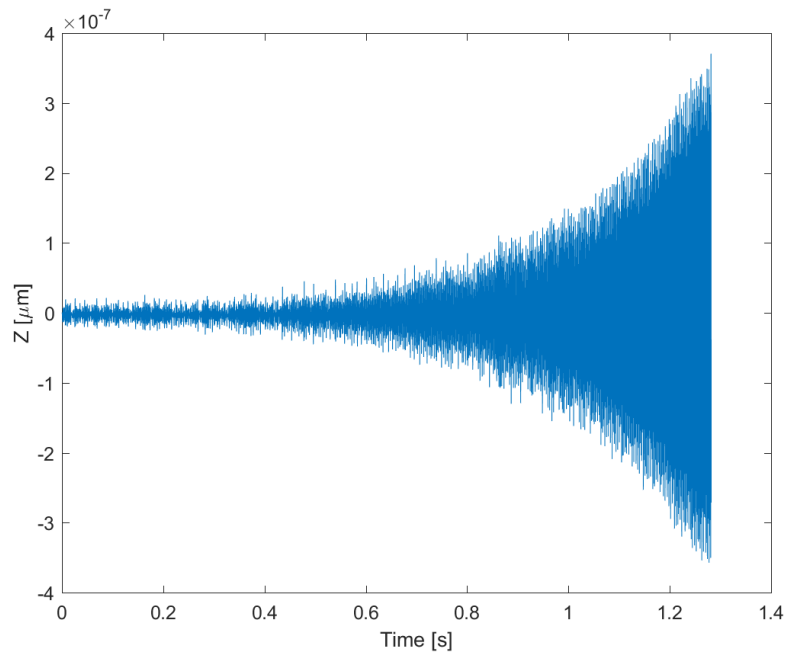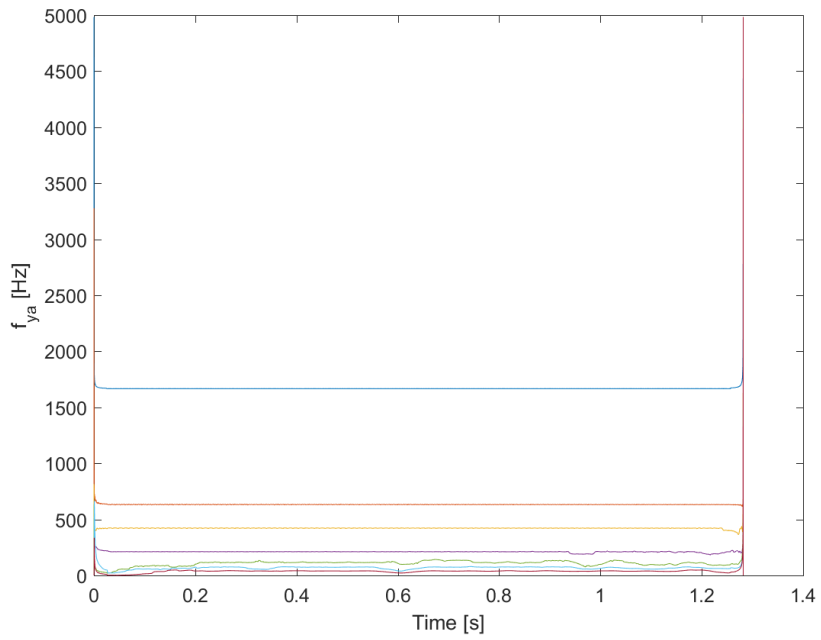
Figure 3.69: WFXLMS test 3: thrust bearing.
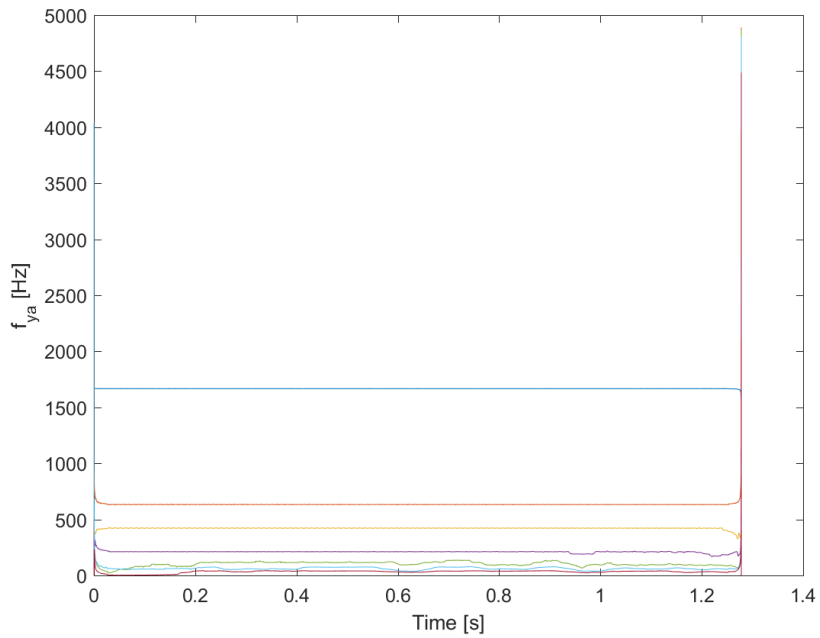
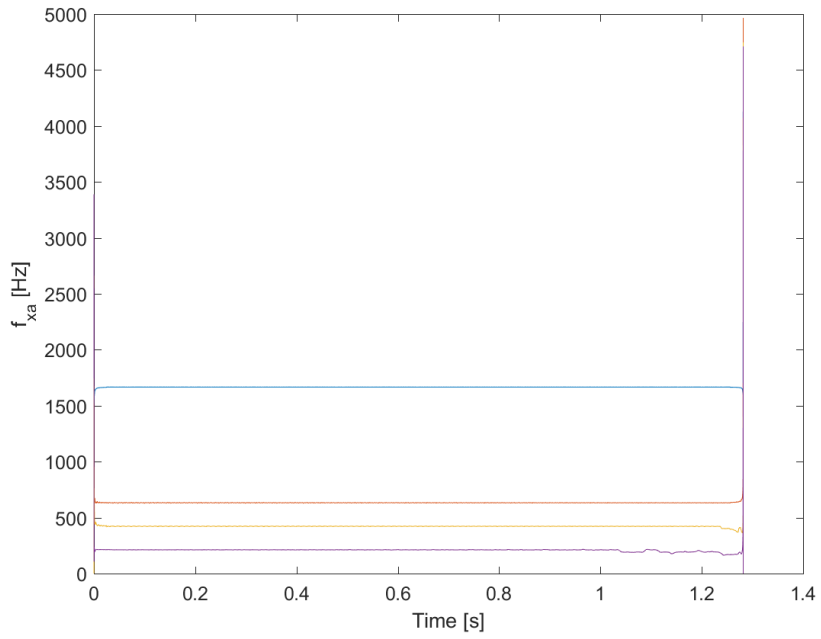Figure 3.70: WFXLMS test 3: bearing A IF response for *y*-axis.

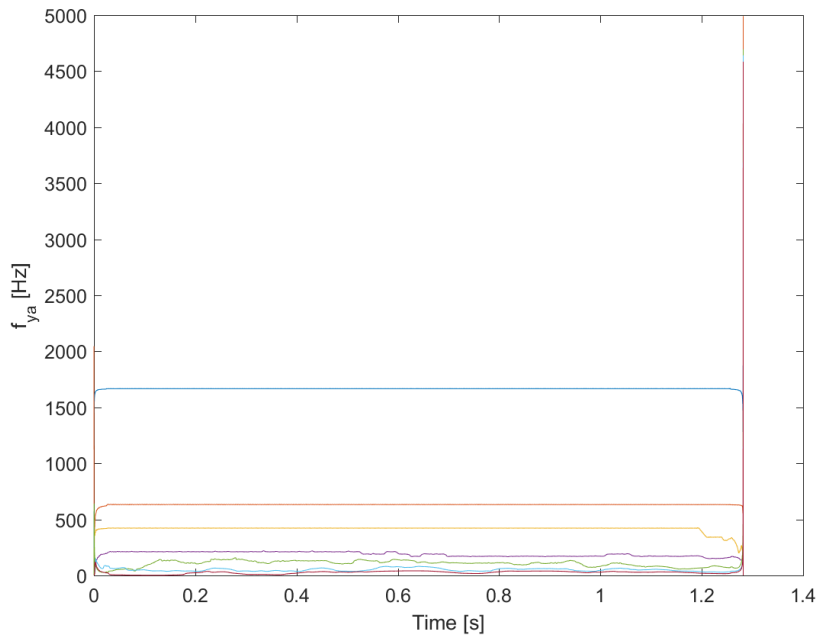Figure 3.71: WFXLMS test 3: bearing A IF response for *x*-axis.

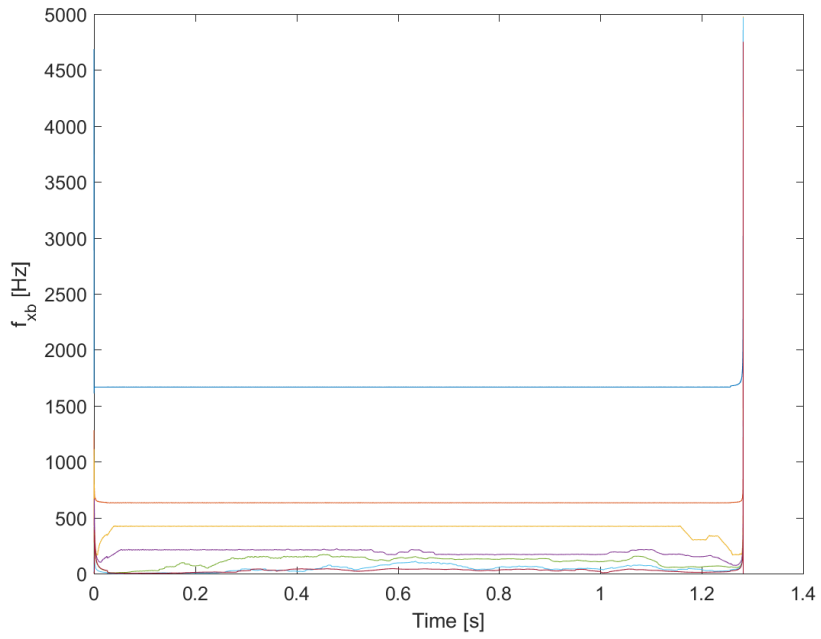Figure 3.72: WFXLMS test 3: bearing B IF response for *y*-axis.

Figure 3.73: WFXLMS test 3: bearing B IF response for *x*-axis.
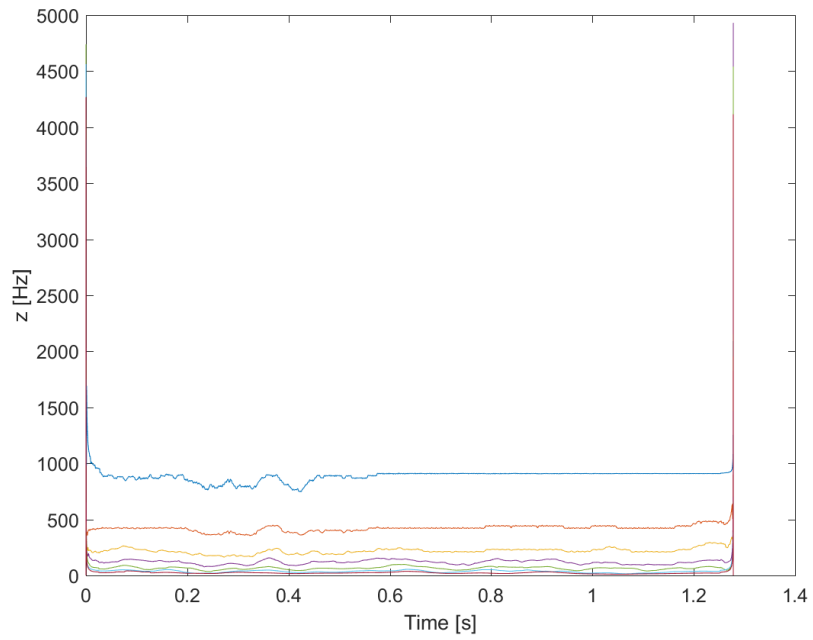
Figure 3.74: WFXLMS test 3: thrust bearing IF response.

This test was run to isolate the impact that the error gain parameters (eG and eGz) have on the dynamic stability of the FES system. After running the test, the temporal and frequency responses looked very similar to the last test's results. Looking at the actual displacement numbers in Table 3.20 and comparing them with Table 3.18 confirms this suspicion with a maximum relative error of about 1% between them. The lower-frequency modes in Figures 3.62 through 3.66 also match those from the last test (Figures 3.70 through 3.74). Apparently, the controller is impervious to the error gain parameters.

3.3.4 Test 4

The flywheel parameters used for this test are listed in Table 3.21. From these testing conditions, the average and maximum values for the current and position in Table 3.22 were determined.

Table 3.21: WFXLMS test 4 conditions.

Term	Value	Units
ω	100000	rpm
	1667	Hz
dt	1×10^{-6}	s
I_{0r}	4	A
I_{0z}	4	A
i_{supply}	16	A
$i_{supplyz}$	16	A
N	512	
eG	1	
eGz	1	
W1	5	
W1z	5	
μ_1	1×10^{-16}	
μ_2	1×10^{-16}	
μ_{1z}	1×10^{-16}	
μ_{2z}	1×10^{-16}	
t_{end}	1.515	

Table 3.22: WFXLMS test 4 results.

Term	Axis	Average	Maximum
Current (A)	x	4.37×10^{-1}	2.45×10^{0}
	y	4.65×10^{-1}	2.55×10^{0}
	z	2.16×10^{-8}	2.04×10^{-7}
Magnitude (m)	x	1.54×10^{-6}	8.65×10^{-6}
	y	1.65×10^{-6}	9.03×10^{-6}
	z	9.56×10^{-14}	9.02×10^{-13}

The time domain response of the FES system at the three bearings are shown in Figures 3.75 through 3.77.

Figure 3.75: WFXLMS test 4: independent bearing A temporal responses.

An instantaneous frequency (IF) plot of each temporal response was generated to evaluate the stability in the frequency domain and is shown in Figures 3.78 through 3.82.
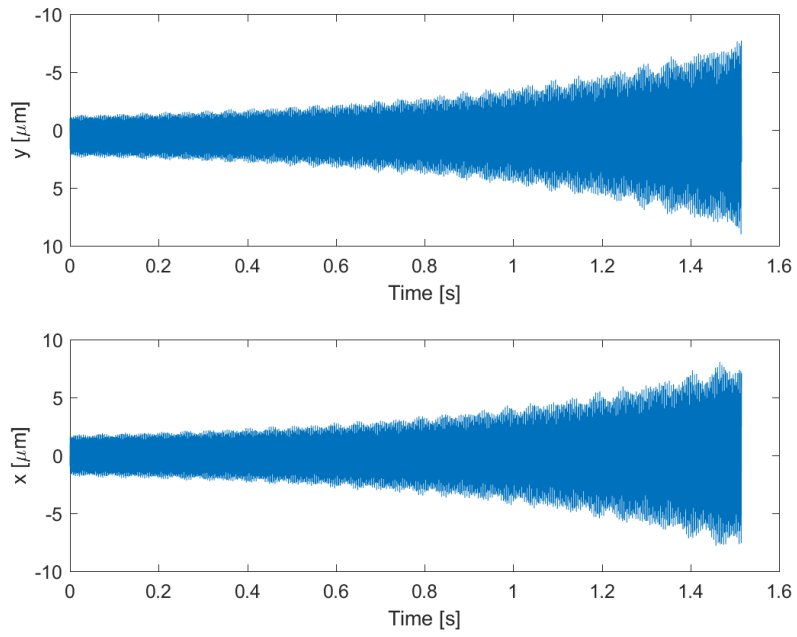
Figure 3.76: WFXLMS test 4: independent bearing B temporal responses.
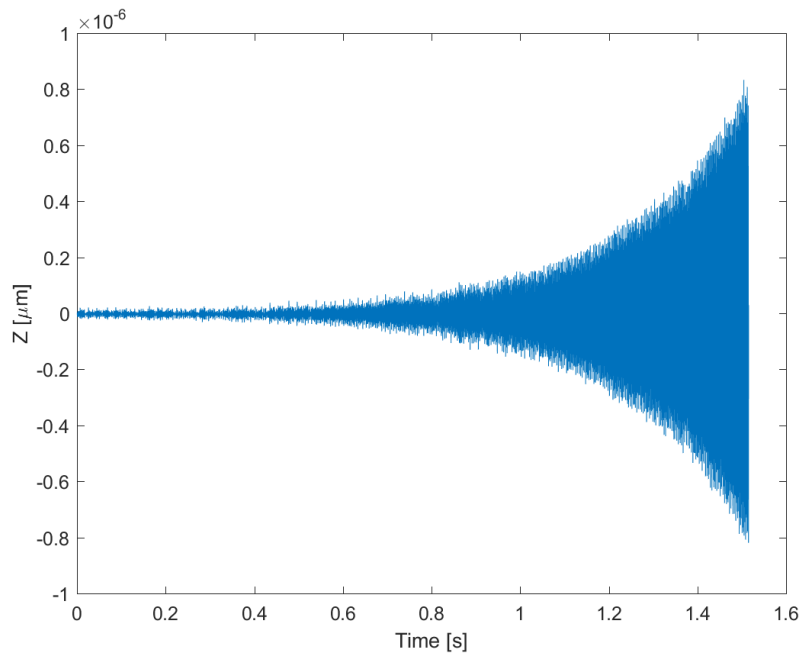
Figure 3.77: WFXLMS test 4: thrust bearing.

The raw data generated for each bearing had significant signal processing noise due to the nature of the IF calculations process. Therefore, a smoothing function was applied to this data to reveal the frequency trends and omit unnecessary data outliers. When comparing the raw plot with the smoothed plot, there was not a noticeable difference in the general trend of the data. Therefore, it is reasonable to assume that these plots do an adequate job depicting the controller's stability in the frequency domain.
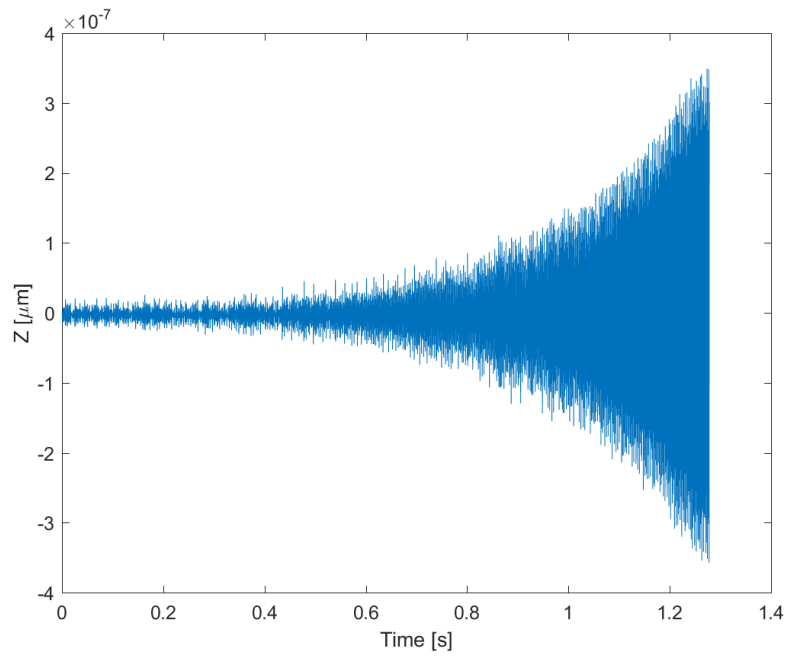

Figure 3.78: WFXLMS test 4: bearing A IF response for *y*-axis.

Again, only one change was made to this system since the last test. This time the filter steps (μ_1, μ_2, μ_{1z}, and μ_{2z}) were made much smaller. Take caution when comparing the current draw and deflections in Table 3.22 with the previous tests because this test ran for about 0.23 seconds longer and continued to diverge. However, this test does show that
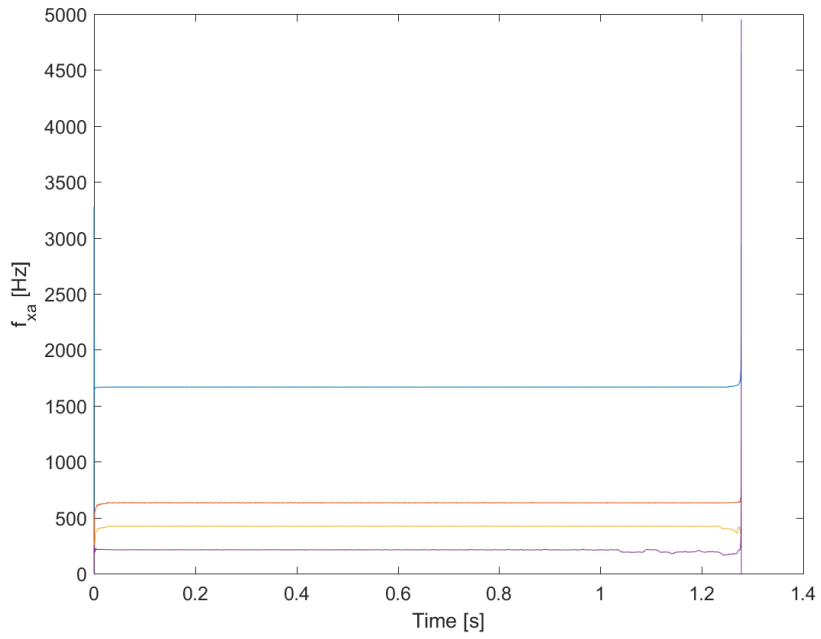
Figure 3.79: WFXLMS test 4: bearing A IF response for *x*-axis.
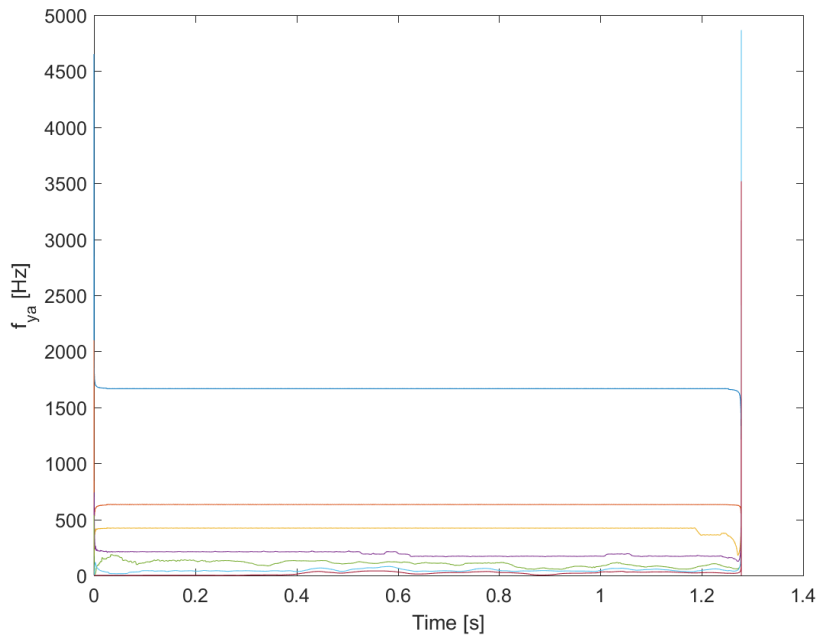

Figure 3.80: WFXLMS test 4: bearing B IF response for *y*-axis.
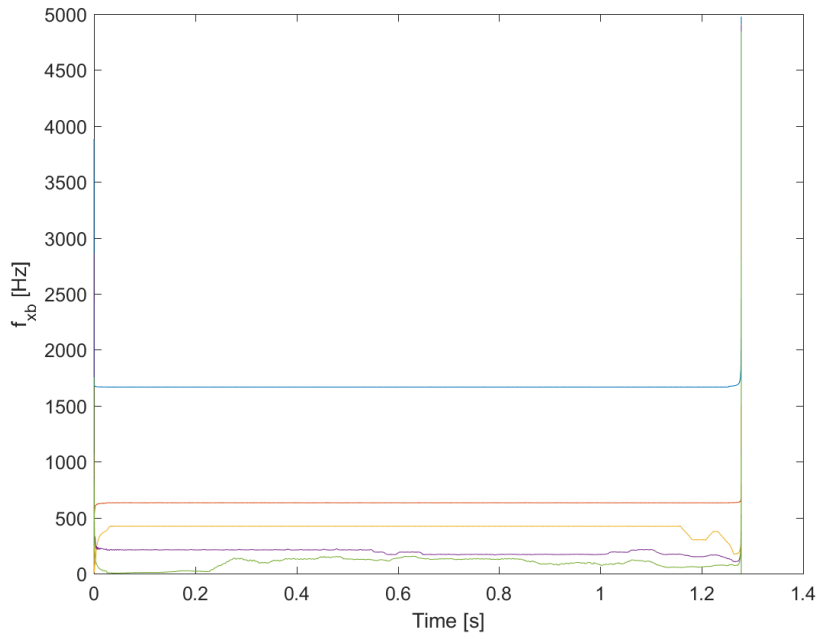
Figure 3.81: WFXLMS test 4: bearing B IF response for *x*-axis.

Figure 3.82: WFXLMS test 4: thrust bearing IF response.

drastically decreasing the filter step sizes does not significantly alter the dynamics of the system in the time or frequency domain. At this point, it is important to remember that the IF plots do not accurately represent the real dynamics of the system at the beginning or end of the plot as the process for obtaining these plots requires a reasonable sample size to extract the frequencies from the time domain plot. This is why there are large spikes in the IF plots at the end of the data.

3.3.5 Test 5

The flywheel parameters used for this test are listed in Table 3.23. From these testing conditions, the average and maximum values for the current and position in Table 3.24 were determined.

Table 3.23: WFXLMS test 5 conditions.

Term	Value	Units
ω	100000	rpm
	1667	Hz
dt	1×10^{-6}	s
I_{0r}	4	A
I_{0z}	4	A
i_{supply}	16	A
$i_{supplyz}$	16	A
N	512	
eG	1	
eGz	1	
W1	5	
W1z	5	
μ_1	1×10^{-8}	
μ_2	1×10^{-2}	
μ_{1z}	1×10^{-8}	
μ_{2z}	1×10^{-2}	
t_{end}	2.5	

Table 3.24: WFXLMS test 5 results.

Term	Axis	Average	Maximum
Current (A)	x	2.10×10^{-1}	5.91×10^{-1}
	y	2.42×10^{-1}	7.75×10^{-1}
	z	2.19×10^{-7}	2.96×10^{-6}
Magnitude (m)	x	7.53×10^{-7}	2.09×10^{-6}
	y	8.92×10^{-7}	2.76×10^{-6}
	z	9.66×10^{-13}	1.31×10^{-11}

The time domain response of the FES system at the three bearings are shown in Figures 3.83 through 3.85.
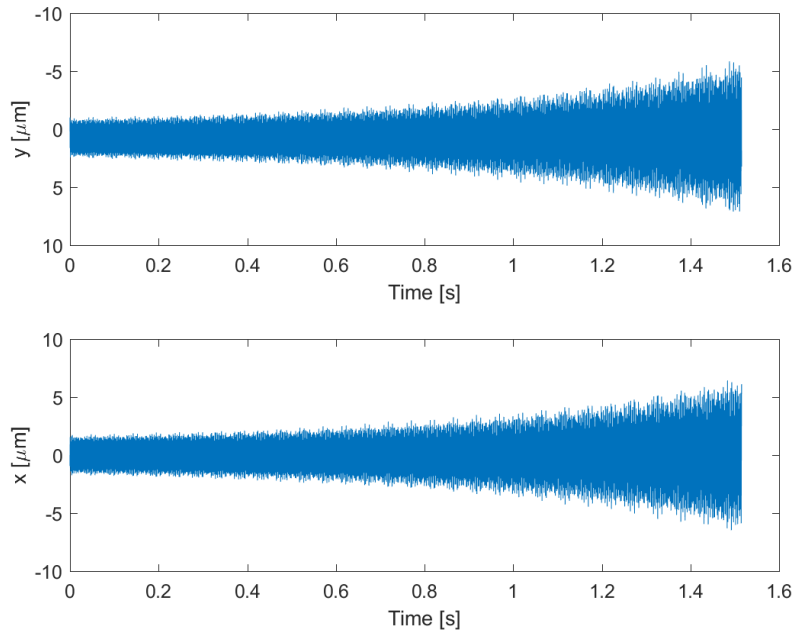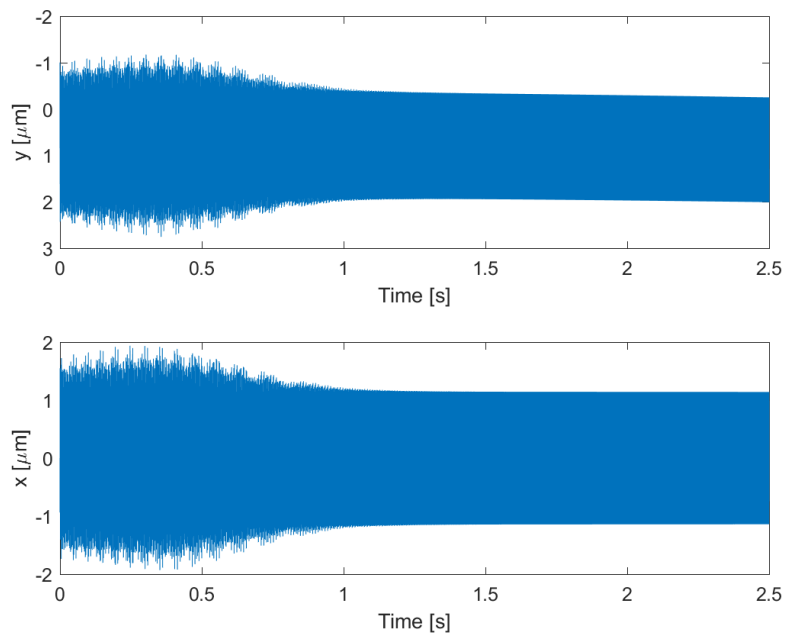

Figure 3.83: WFXLMS test 5: independent bearing A temporal responses.

An instantaneous frequency (IF) plot of each temporal response was generated to evaluate the stability in the frequency domain and is shown in Figures 3.86 through 3.90. The raw data generated for each bearing had significant signal processing noise due to the
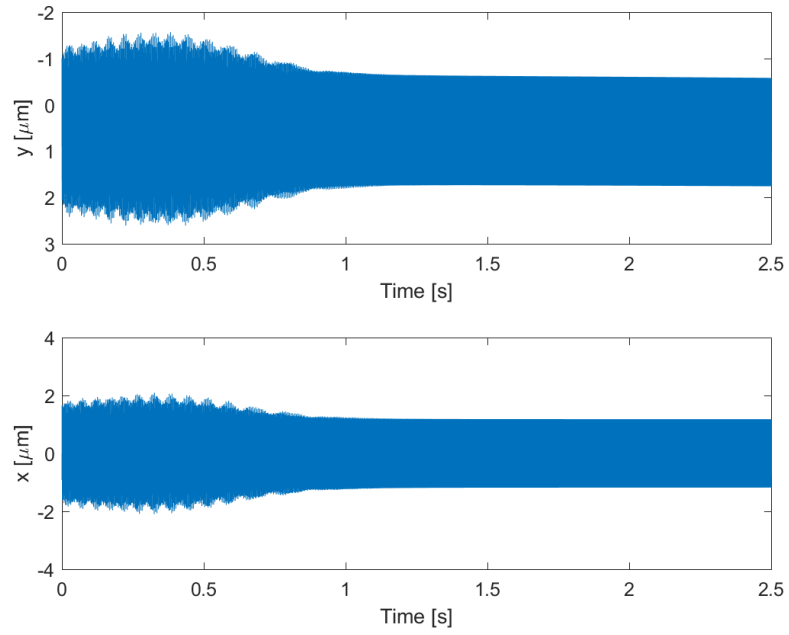
Figure 3.84: WFXLMS test 5: independent bearing B temporal responses.
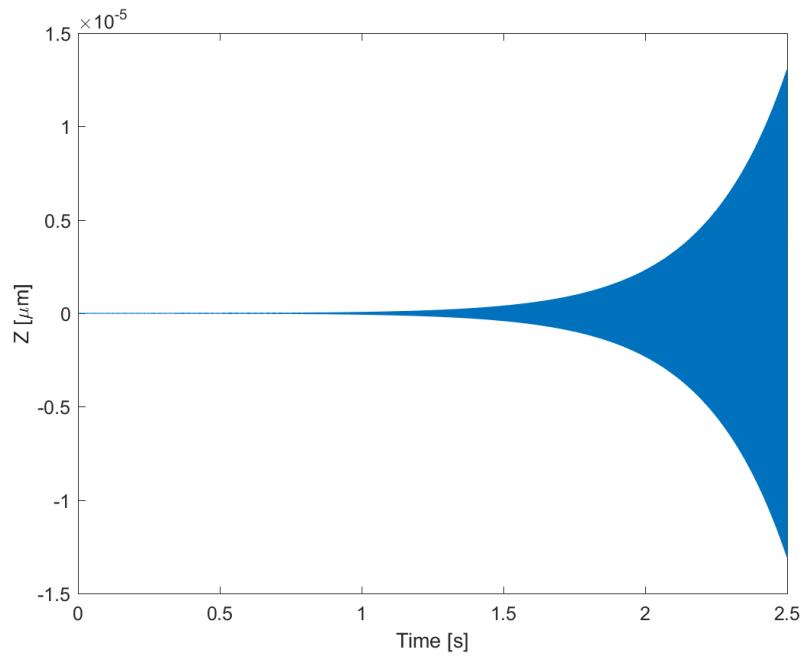
Figure 3.85: WFXLMS test 5: thrust bearing.

nature of the IF calculations process. Therefore, a smoothing function was applied to this data to reveal the frequency trends and omit unnecessary data outliers. When comparing the raw plot with the smoothed plot, there was not a noticeable difference in the general trend of the data. Therefore, it is reasonable to assume that these plots do an adequate job depicting the controller's stability in the frequency domain.
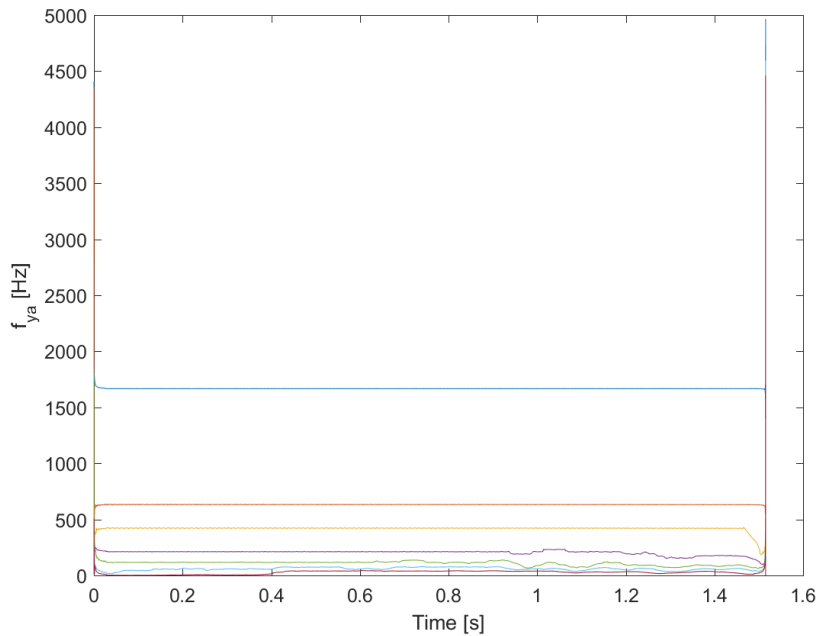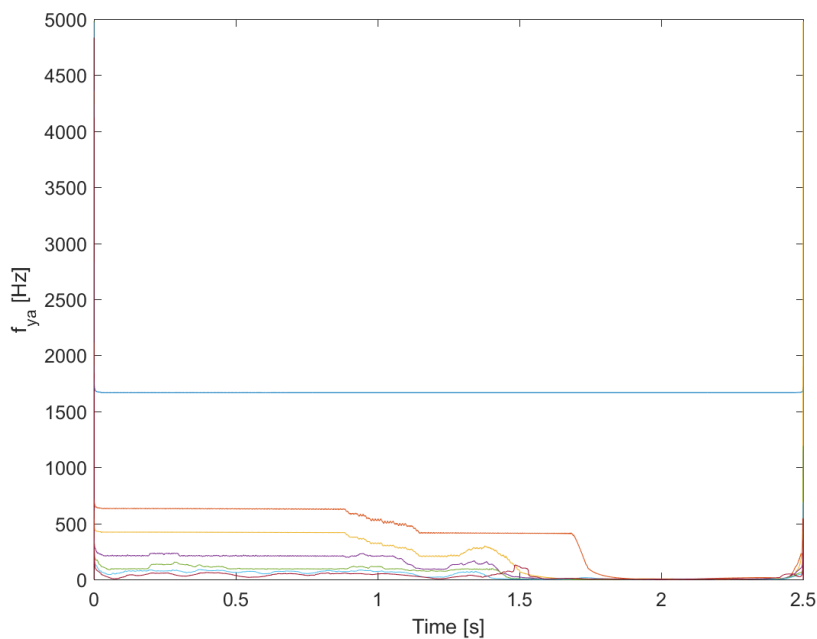

Figure 3.86: WFXLMS test 5: bearing A IF response for *y*-axis.

This test examined the impact that drastically different filter step sizes for the inner and outer loops of the WFXLMS controller had on the dynamics of the FES system. The inner loop, which is governed by μ_1 and μ_{1z}, was set to a small number to allow it to try and capture any high frequency noise in the system while the outer loop step sizes, (μ_2 and μ_{2z}), were made much bigger to allow the controller to make more drastic filter coefficient
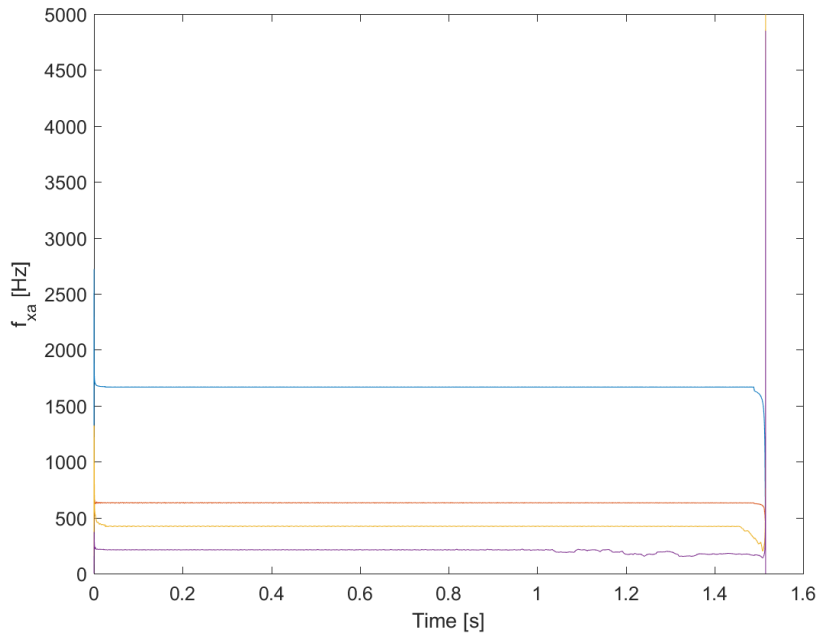
Figure 3.87: WFXLMS test 5: bearing A IF response for *x*-axis.
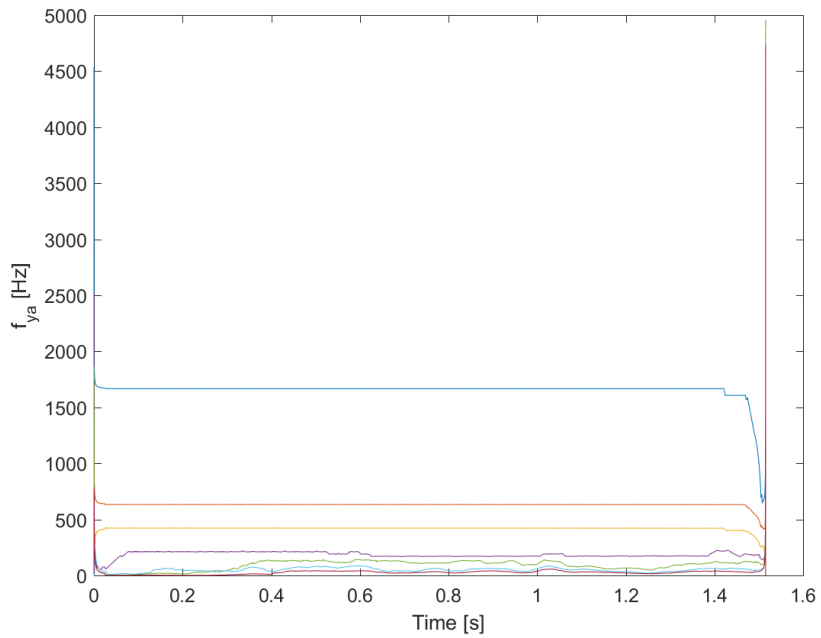

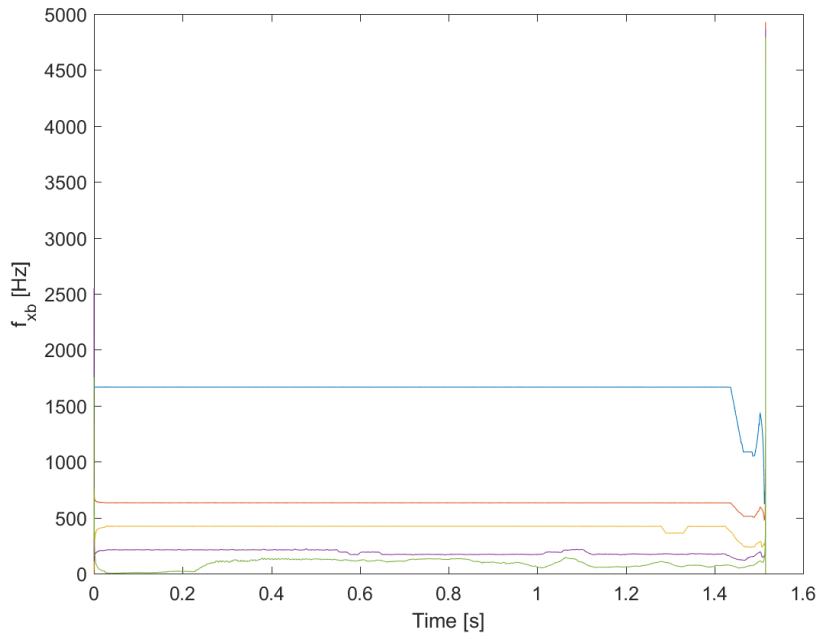Figure 3.88: WFXLMS test 5: bearing B IF response for *y*-axis.

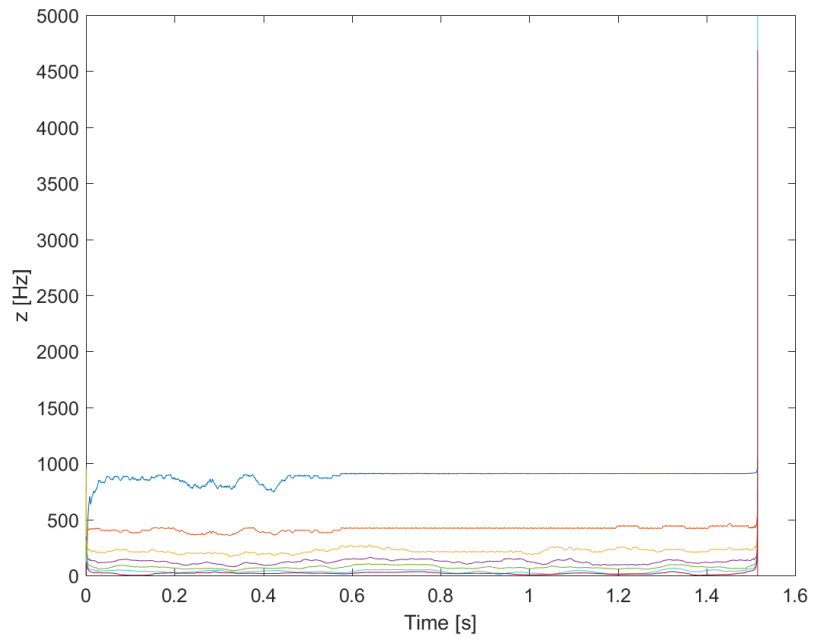Figure 3.89: WFXLMS test 5: bearing B IF response for *x*-axis.

Figure 3.90: WFXLMS test 5: thrust bearing IF response.

changes from step to step.

As the time plots show in Figures 3.83 through 3.85, the *x*- and *y*-axis converged in about one second just like in the first test, but it still demonstrated a slight drift away from 0 due to the effects of gravity. Again, the *z*-axis temporal response shows a diverging behavior. While the IF plots still show stability through the duration of the test, it is impossible to say that the controller achieved full dynamic stability as all of the axes demonstrate some trend that, if projected into the future, would eventually collide with the bearing housing.

Notably, this controller is working almost exactly as required in the *x*- and *y*-axis (beside the small drift away from 0) but is only drawing about 0.24 Amps on average compared to PID's 0.69 Amps and fuzzy-logic's 0.84 Ams at 100,000 rpm. Therefore, it is possible that increasing the supply current to try and match the PID and fuzzy-logic controller will reduce the drifting behavior of the controller.

3.3.6   Test 6

The flywheel parameters used for this test are listed in Table 3.25. From these testing conditions, the average and maximum values for the current and position in Table 3.26 were determined.

The time domain response of the FES system at the three bearings are shown in Figures 3.91 through 3.93.

An instantaneous frequency (IF) plot of each temporal response was generated to evaluate the stability in the frequency domain and is shown in Figures 3.94 through 3.98. The raw data generated for each bearing had significant signal processing noise due to the

Table 3.25: WFXLMS test 6 conditions.

Term	Value	Units
ω	100000	rpm
	1667	Hz
dt	1×10^{-6}	s
I_{0r}	4	A
I_{0z}	4	A
i_{supply}	20	A
$i_{supplyz}$	20	A
N	512	
eG	1	
eGz	1	
W1	5	
W1z	5	
μ_1	5×10^{-3}	
μ_2	5×10^{-3}	
μ_{1z}	1×10^{-8}	
μ_{2z}	1×10^{-8}	
t_{end}	2.5	

Figure 3.91: WFXLMS test 6: independent bearing A temporal responses.

Table 3.26: WFXLMS test 6 results.

Term	Axis	Average	Maximum
	x	2.59×10^{-1}	6.95×10^{-1}
Current (A)	y	2.80×10^{-1}	8.33×10^{-1}
	z	3.81×10^{-13}	1.48×10^{-12}
	x	7.70×10^{-7}	1.97×10^{-6}
Magnitude (m)	y	8.58×10^{-7}	2.37×10^{-6}
	z	6.74×10^{-18}	2.62×10^{-17}
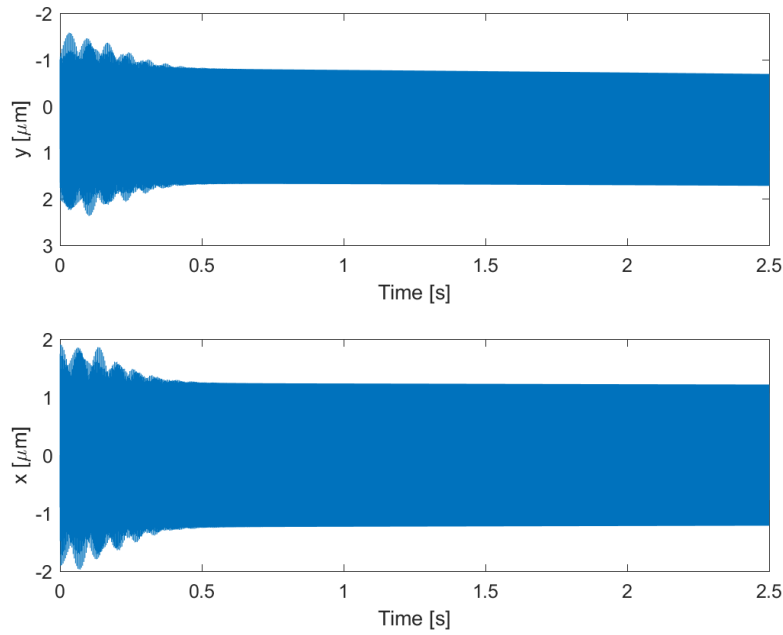
Figure 3.92: WFXLMS test 6: independent bearing B temporal responses.

nature of the IF calculations process. Therefore, a smoothing function was applied to this data to reveal the frequency trends and omit unnecessary data outliers. When comparing the raw plot with the smoothed plot, there was not a noticeable difference in the general trend of the data. Therefore, it is reasonable to assume that these plots do an adequate job depicting the controller's stability in the frequency domain.

This time, the step size for the journal bearing controllers (μ_1 and μ_2) and the thrust
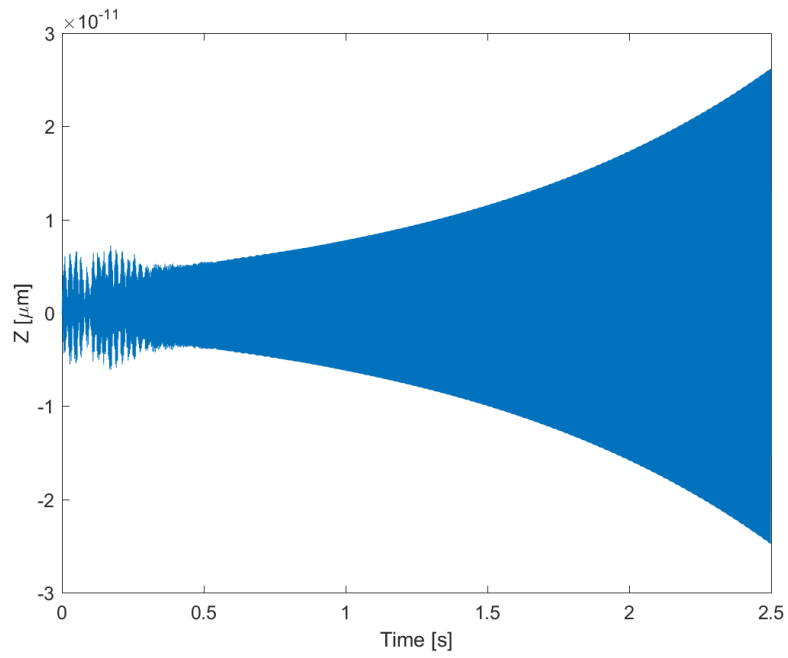
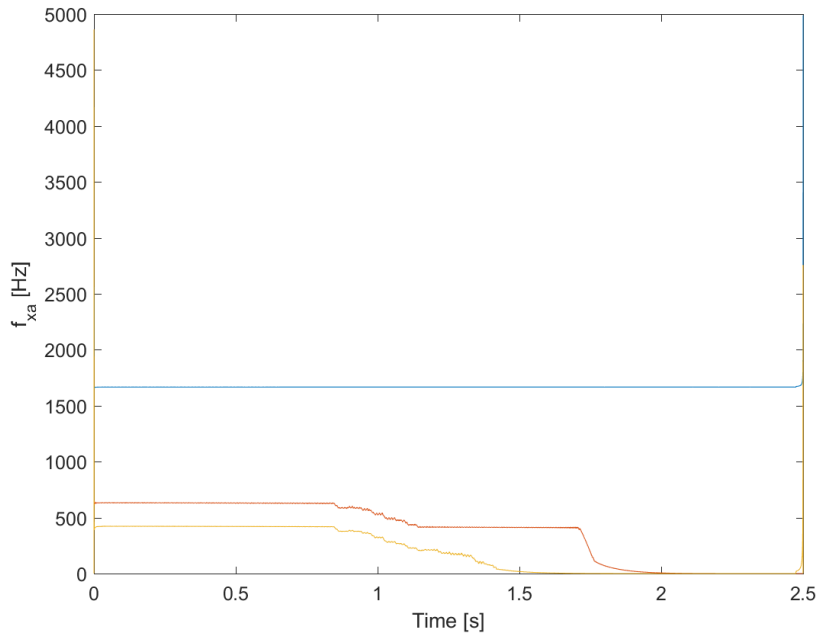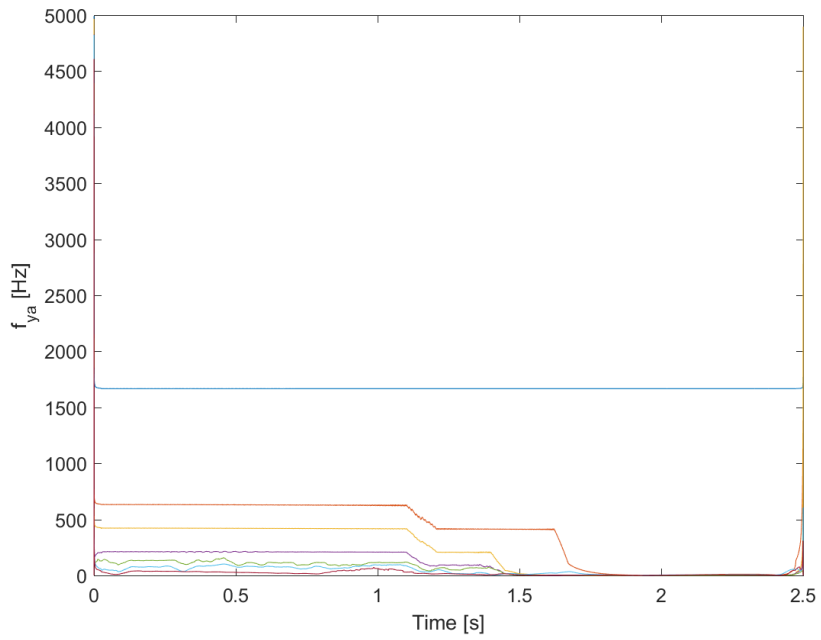Figure 3.93: WFXLMS test 6: thrust bearing.

Figure 3.94: WFXLMS test 6: bearing A IF response for *y*-axis.

Figure 3.95: WFXLMS test 6: bearing A IF response for *x*-axis.

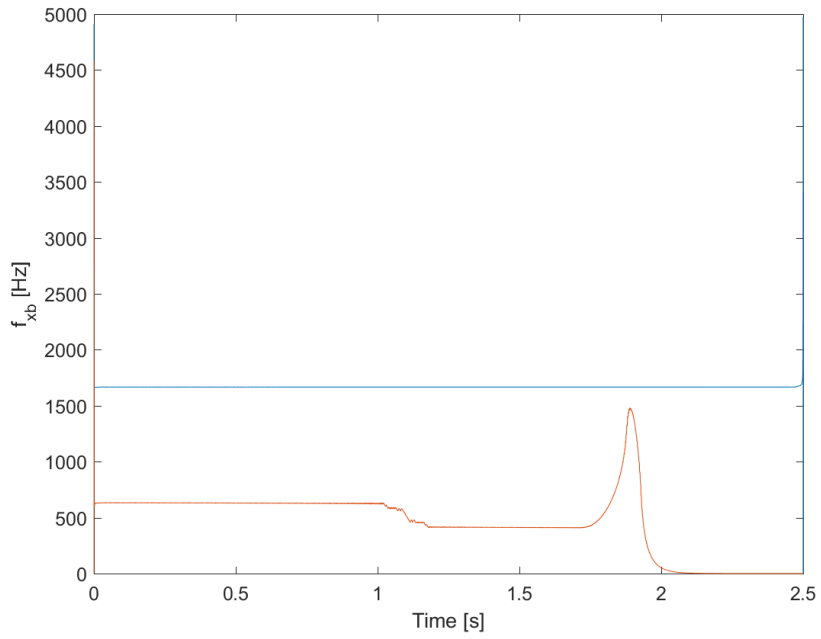Figure 3.96: WFXLMS test 6: bearing B IF response for *y*-axis.

106

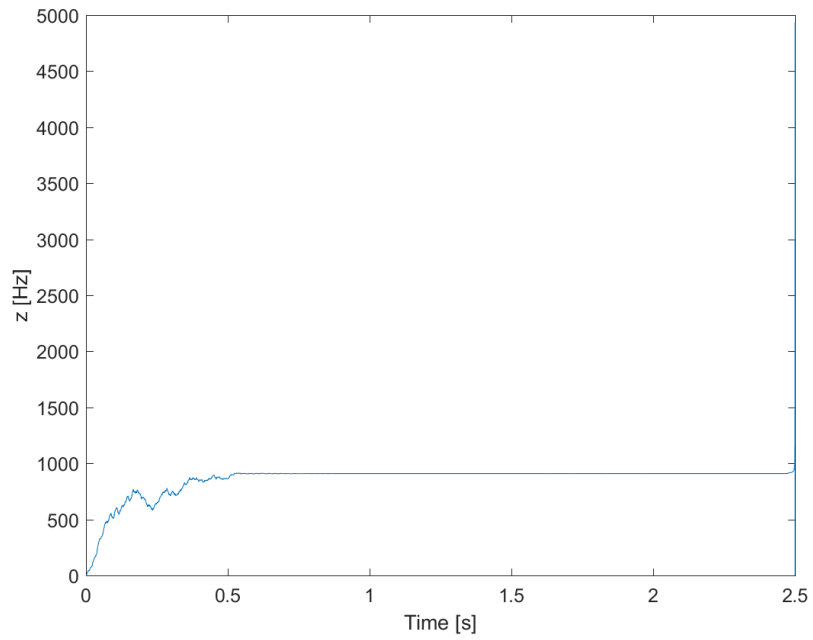Figure 3.97: WFXLMS test 6: bearing B IF response for *x*-axis.
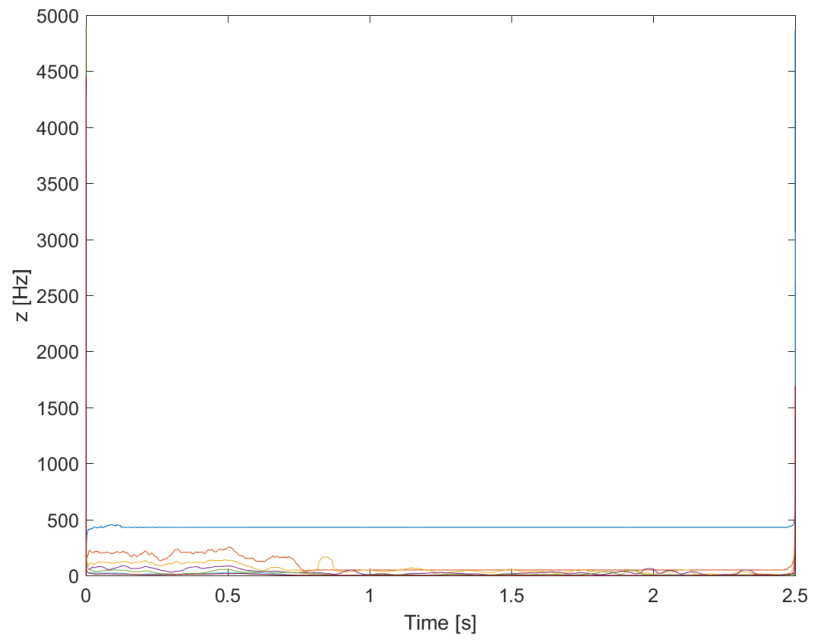
Figure 3.98: WFXLMS test 6: thrust bearing IF response.

bearing (μ_{1z} and μ_{2z}) were set to different values. These parameters were set to different values because the dynamics of the journal bearings and the thrust bearing are unique and, therefore, possibly need to be treated differently by the controller. Based on the previous tests, a relatively big value for the journal bearings filter step size was used because it showed the best results, the ideal filter step values for the thrust bearing was still unknown; thus, an arbitrarily smaller value was used. A smaller value for mu_{1z} and μ_{2z} was selected because using a value larger than μ_1 and μ_2 caused the simulation to crash immediately.

Figure 3.98 shows that the main IF mode of the thrust bearing settled at a little under 500 Hz while all the other, lower modes essentially disappeared. Despite operating at a stead frequency in the z-axis, the amplitude again showed diverging behavior in the time domain (Figure 3.93) for the first 2.5 seconds of operation; which, at the very least, is far worse behavior than either the PID or fuzzy-logic controllers. IF plots for the journal bearings (Figures 3.94 through 3.97) show that the main mode is steady at the operating speed while the lower modes all eventually head towards 0. This indicates that the system is predictable and steady in the frequency domain. However, the system still shows a tiny divergence away from 0 due to the effects of gravity in the time domain (see the y-axis is Figures 3.91 and 3.92). Also, increasing the supply current from 16 Amps to 20 Amps barely changed the average current draw from the previous test (0.28 Amps vs. 0.24 Amps in test 5).

3.3.7 Test 7

The flywheel parameters used for this test are listed in Table 3.27. From these testing conditions, the average and maximum values for the current and position in Table 3.28 were determined.

Table 3.27: WFXLMS test 7 conditions.

Term	Value	Units
ω	100000	rpm
	1667	Hz
dt	1×10^{-6}	s
I_{0r}	4	A
I_{0z}	4	A
i_{supply}	20	A
$i_{supplyz}$	20	A
N	512	
eG	1	
eGz	1	
W1	5	
W1z	5	
μ_1	5×10^{-4}	
μ_2	5×10^{-4}	
μ_{1z}	1×10^{-8}	
μ_{2z}	1×10^{-8}	
t_{end}	2.03	

Table 3.28: WFXLMS test 7 results.

Term	Axis	Average	Maximum
Current (A)	x	2.60×10^{-1}	7.99×10^{-1}
	y	3.53×10^{-1}	1.11×10^{0}
	z	7.03×10^{-9}	2.01×10^{-8}
Magnitude (m)	x	7.40×10^{-7}	2.26×10^{-6}
	y	1.01×10^{-6}	3.15×10^{-6}
	z	1.24×10^{-13}	3.56×10^{-13}

The time domain response of the FES system at the three bearings are shown in Figures 3.99 through 3.101.

Figure 3.99: WFXLMS test 7: independent bearing A temporal responses.

An instantaneous frequency (IF) plot of each temporal response was generated to evaluate the stability in the frequency domain and is shown in Figures 3.102 through 3.106. The raw data generated for each bearing had significant signal processing noise due to the nature of the IF calculations process. Therefore, a smoothing function was applied to this data to reveal the frequency trends and omit unnecessary data outliers. When comparing the raw plot with the smoothed plot, there was not a noticeable difference in the general trend of the data. Therefore, it is reasonable to assume that these plots do an adequate job depicting the controller's stability in the frequency domain.

Figure 3.100: WFXLMS test 7: independent bearing B temporal responses.
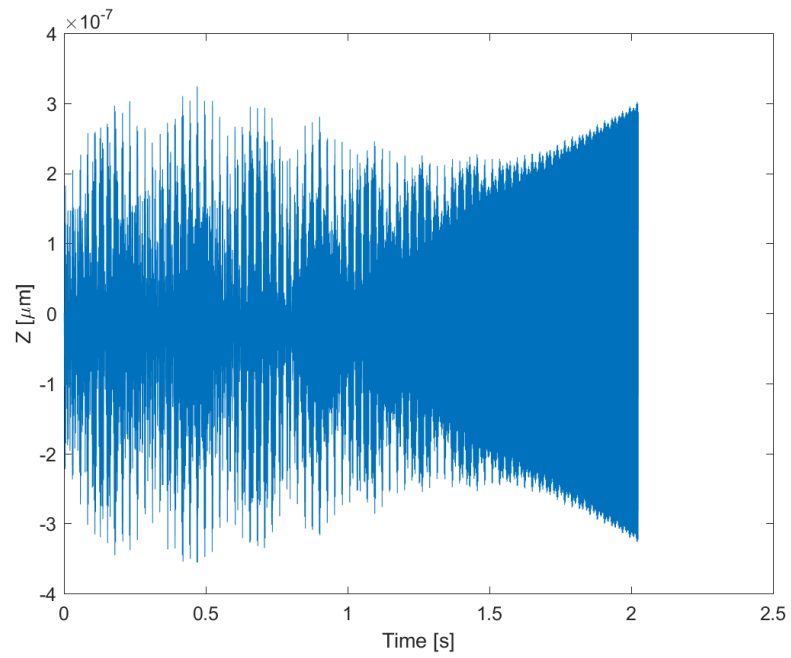
Figure 3.101: WFXLMS test 7: thrust bearing.

Figure 3.102: WFXLMS test 7: bearing A IF response for *y*-axis.

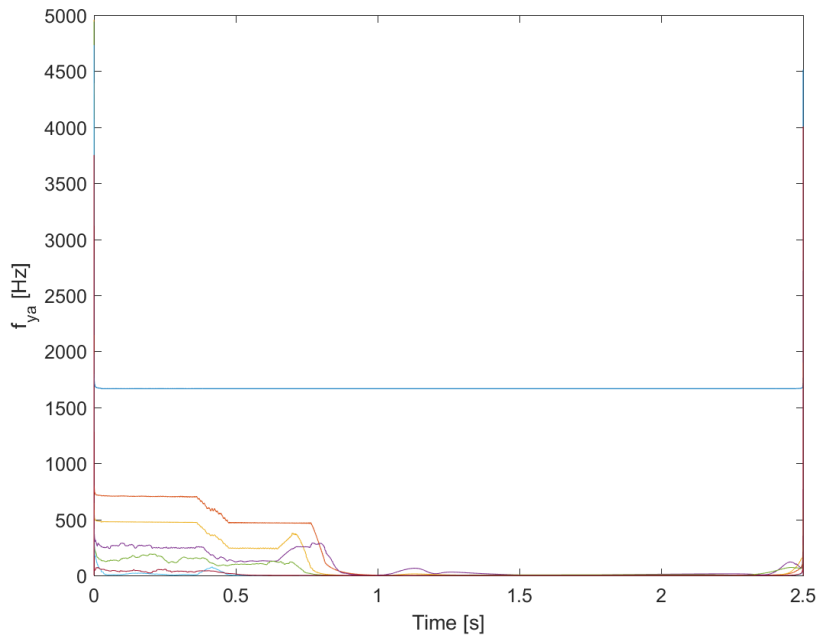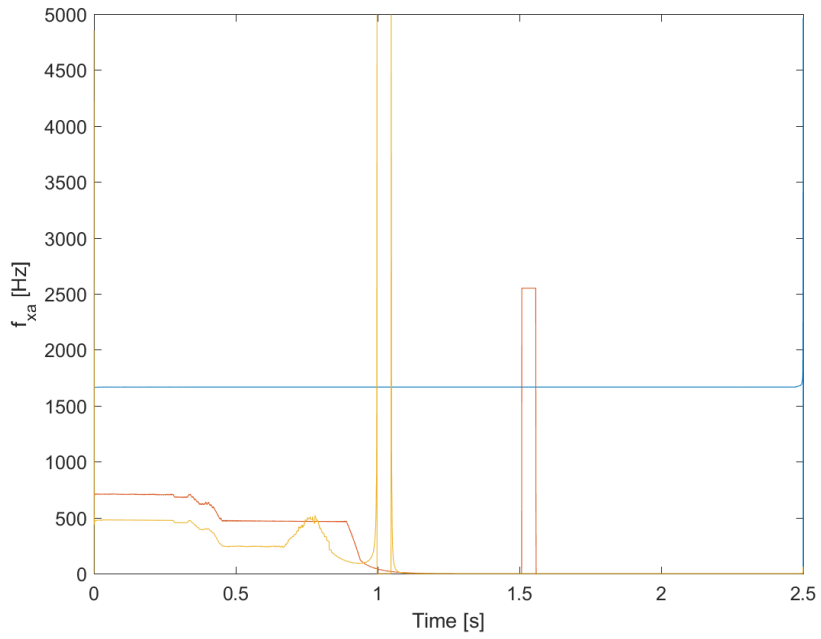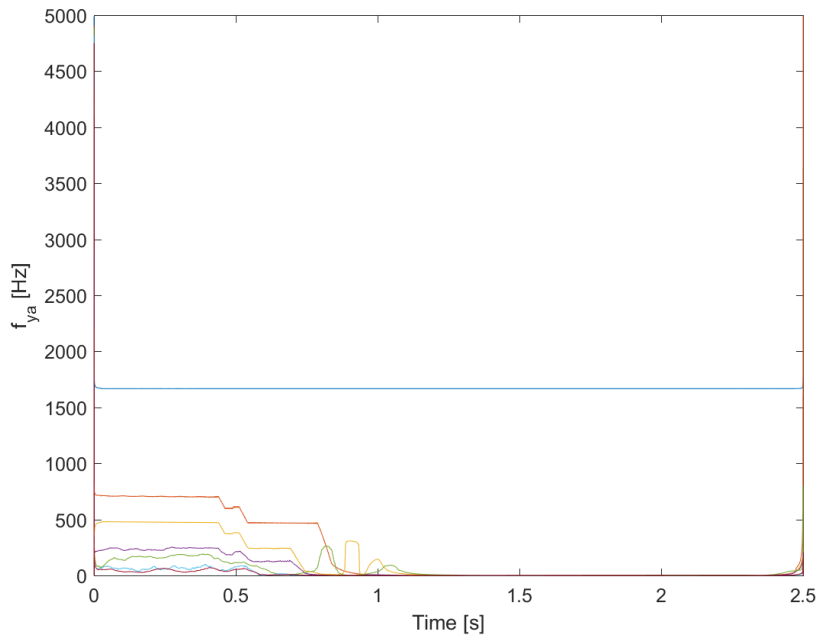Figure 3.103: WFXLMS test 7: bearing A IF response for *x*-axis.
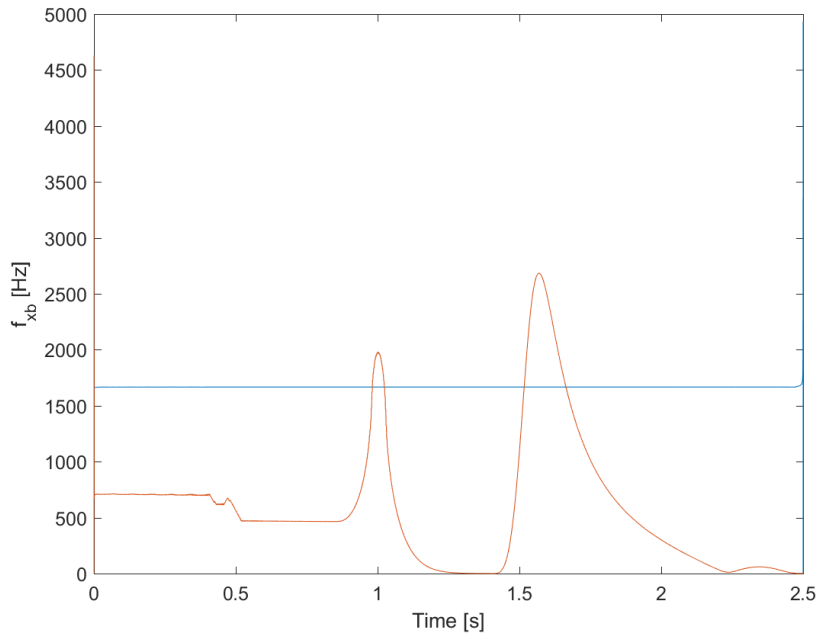
Figure 3.104: WFXLMS test 7: bearing B IF response for *y*-axis.

Figure 3.105: WFXLMS test 7: bearing B IF response for *x*-axis.

Figure 3.106: WFXLMS test 7: thrust bearing IF response.

In this test, the only change was a reduction of the filter step sizes for the journal

bearings (μ_1 and μ_2) from 5×10^{-3} to 5×10^{-4}. This was done primarily to see if it changed

how changing only the journal bearing dynamics changed the entire system dynamics. As

it turns out, a reduction by an order of magnitude did not change much. The average and

maximum current and displacement values were nearly identical for the x-axis, but saw

notable increases in the y- and z-axis; confirming that a larger filter step size for the journal

bearings improves the level of control.

The time domain shapes look nearly identical when comparing this test to the last,

but the IF responses look unique (Figures 3.102 through 3.106). In this test, all fundamen-

tal modes in every plot seem to hold steady for the duration of the test while in the last

test (Figures 3.94 through 3.98), all modes except for the operating frequency seem to be

eliminated after one second.

3.3.8 Test 8

The flywheel parameters used for this test are listed in Table 3.29. From these testing conditions, the average and maximum values for the current and position in Table 3.30 were determined.

Table 3.29: WFXLMS test 8 conditions.

Term	Value	Units
ω	100000	rpm
	1667	Hz
dt	5×10^{-7}	s
I_{0r}	4	A
I_{0z}	4	A
i_{supply}	20	A
$i_{supplyz}$	20	A
N	512	
eG	1	
eGz	1	
W1	5	
W1z	5	
μ_1	5×10^{-4}	
μ_2	5×10^{-4}	
μ_{1z}	1×10^{-8}	
μ_{2z}	1×10^{-8}	
t_{end}	2.03	

Table 3.30: WFXLMS test 8 results.

Term	Axis	Average	Maximum
	x	2.52×10^{-1}	7.34×10^{-1}
Current (A)	y	3.43×10^{-1}	1.06×10^{0}
	z	7.53×10^{-9}	2.04×10^{-8}
	x	7.23×10^{-7}	2.08×10^{-6}
Magnitude (m)	y	1.00×10^{-6}	3.01×10^{-6}
	z	1.33×10^{-13}	3.60×10^{-13}

The time domain response of the FES system at the three bearings are shown in Figures 3.107 through 3.109.
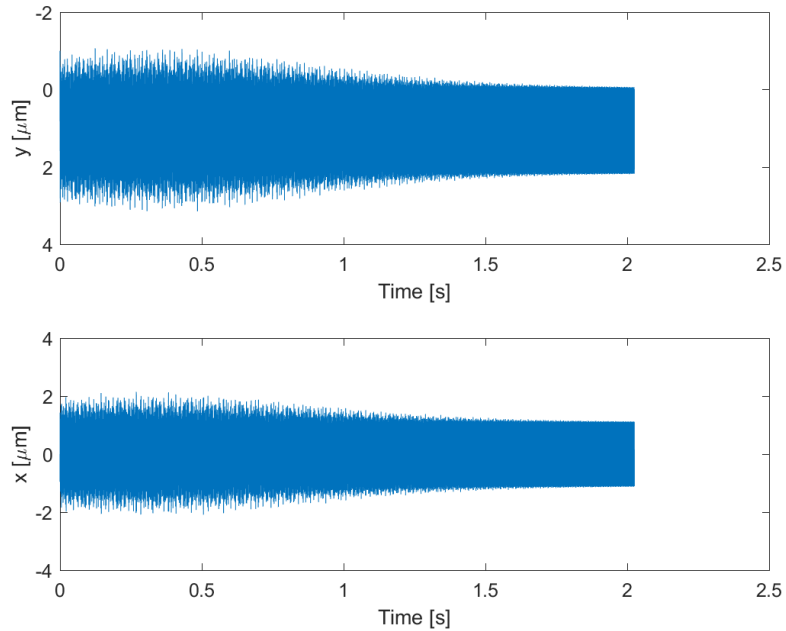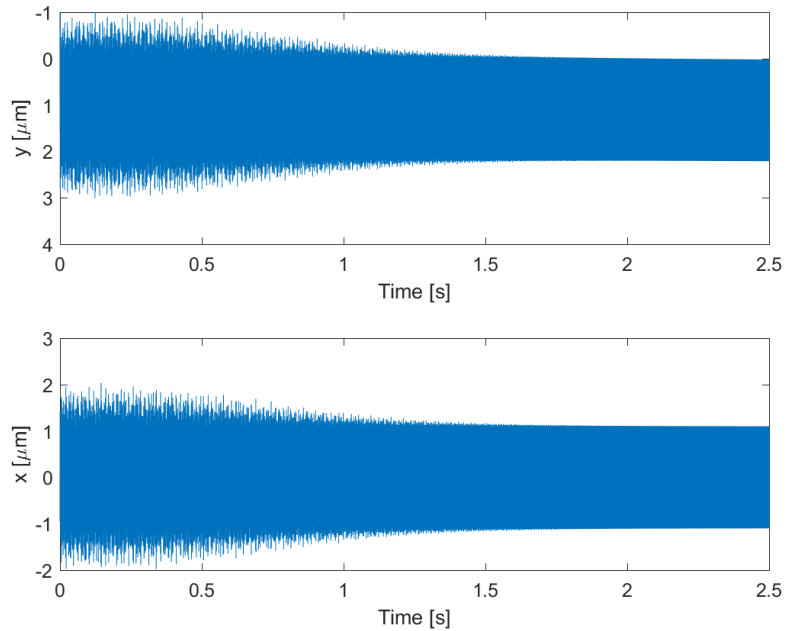

Figure 3.107: WFXLMS test 8: independent bearing A temporal responses.

An instantaneous frequency (IF) plot of each temporal response was generated to evaluate the stability in the frequency domain and is shown in Figures 3.110 through 3.114. The raw data generated for each bearing had significant signal processing noise due to the nature of the IF calculations process. Therefore, a smoothing function was applied to this data to reveal the frequency trends and omit unnecessary data outliers. When comparing the raw plot with the smoothed plot, there was not a noticeable difference in the general trend of the data. Therefore, it is reasonable to assume that these plots do an adequate job depicting the controller's stability in the frequency domain.
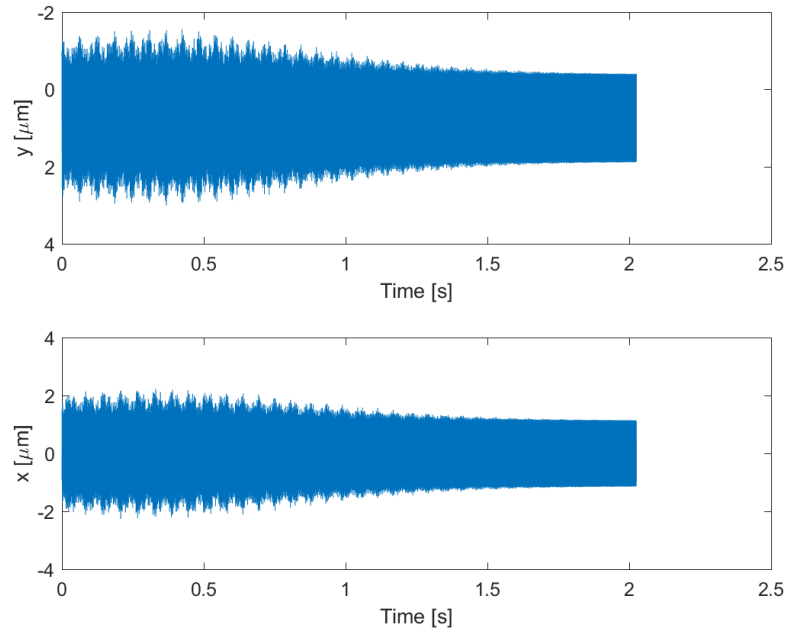
Figure 3.108: WFXLMS test 8: independent bearing B temporal responses.
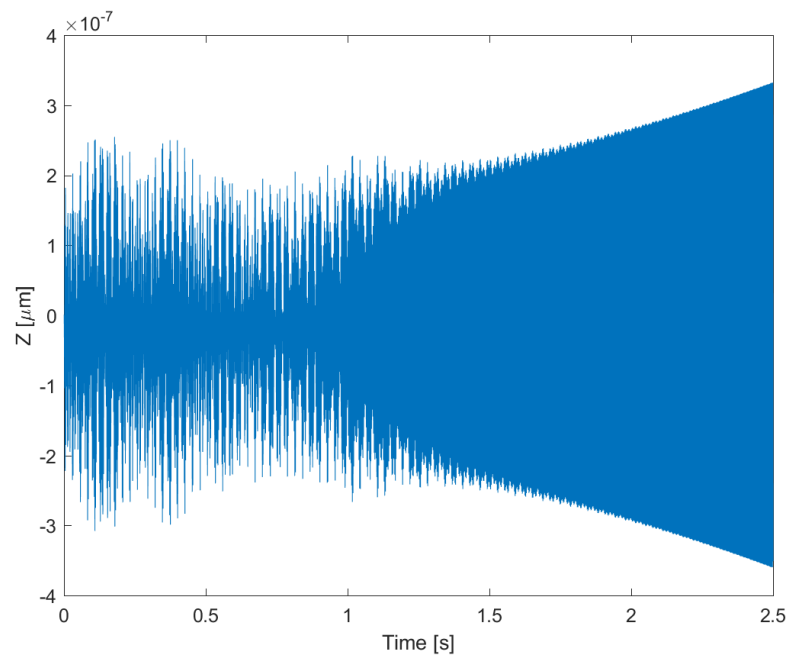
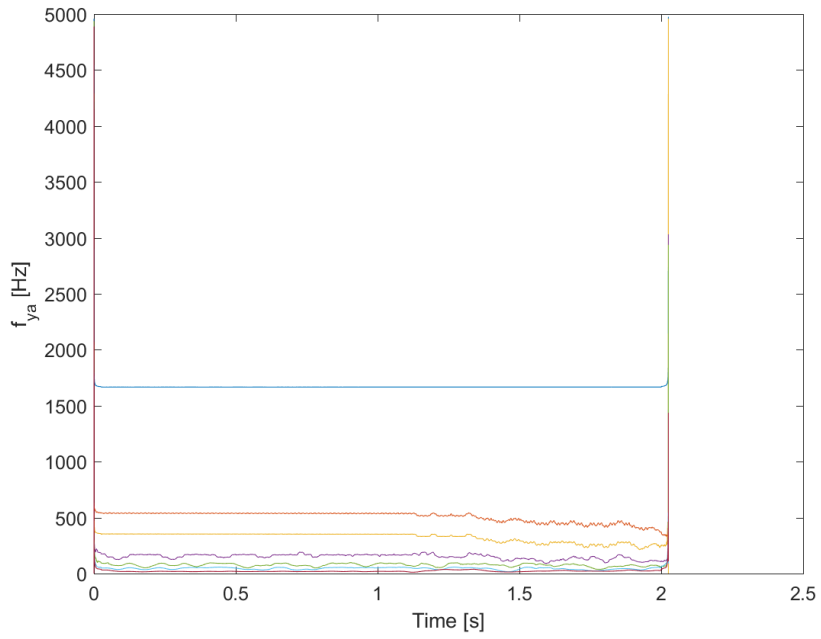Figure 3.109: WFXLMS test 8: thrust bearing.

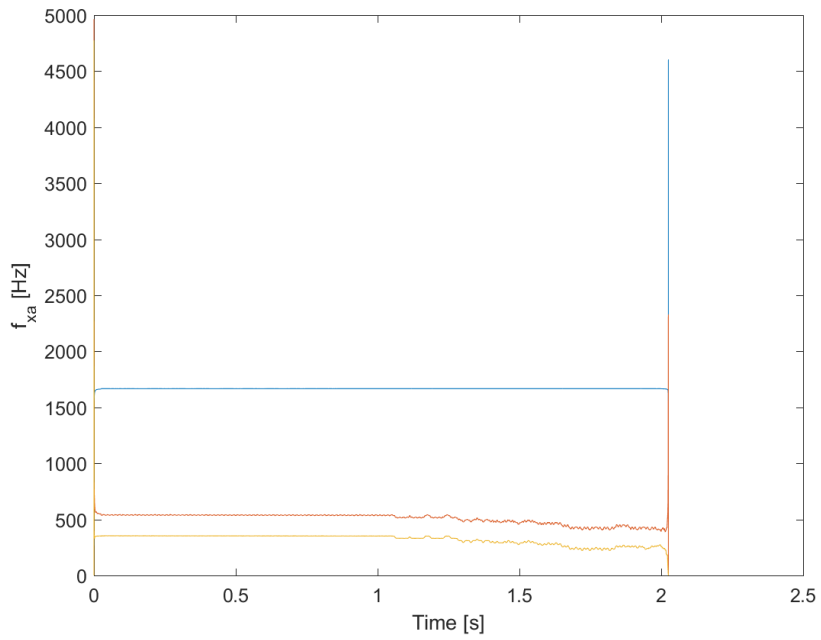Figure 3.110: WFXLMS test 8: bearing A IF response for *y*-axis.

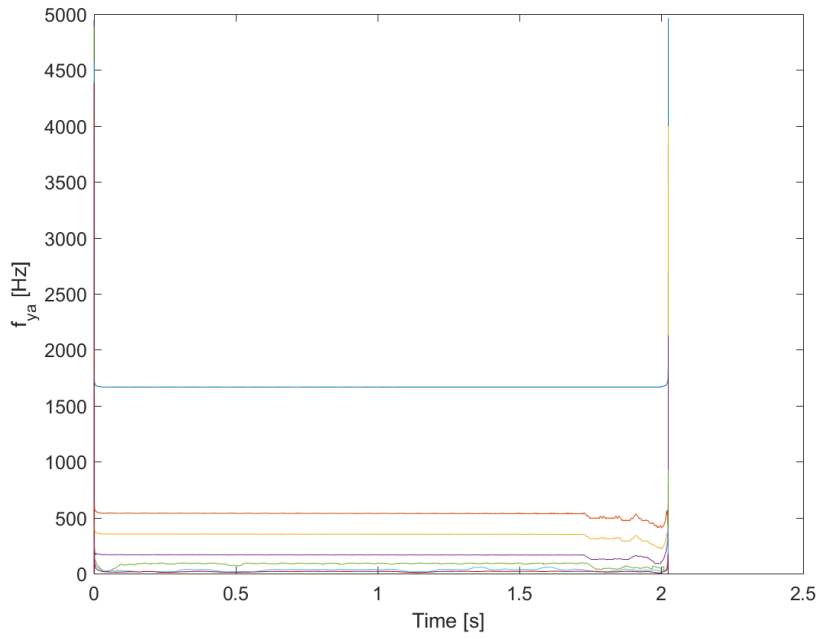Figure 3.111: WFXLMS test 8: bearing A IF response for *x*-axis.

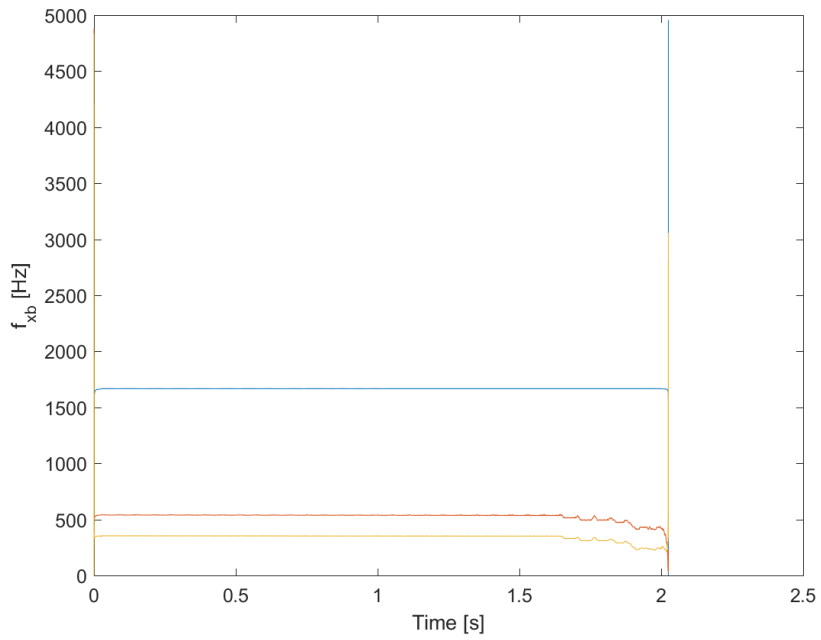Figure 3.112: WFXLMS test 8: bearing B IF response for *y*-axis.

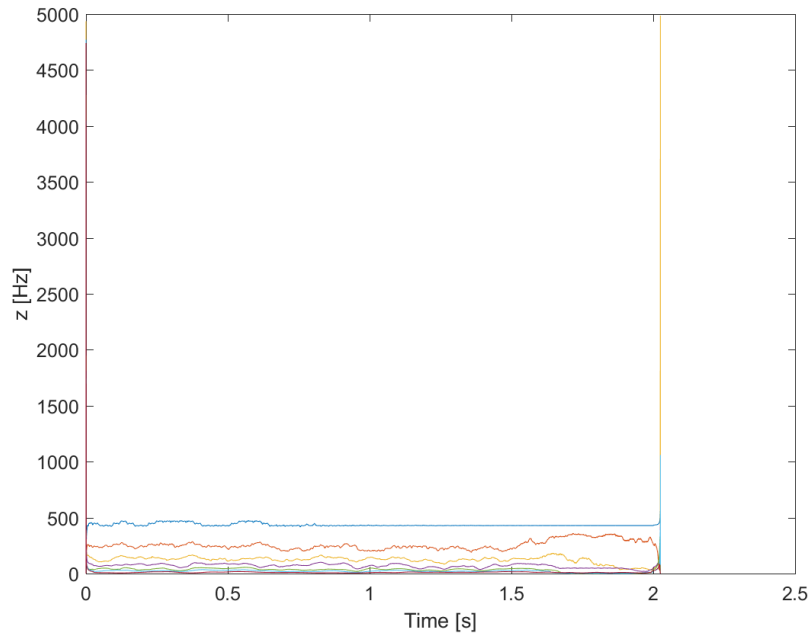Figure 3.113: WFXLMS test 8: bearing B IF response for *x*-axis.

119

Figure 3.114: WFXLMS test 8: thrust bearing IF response.

The only difference between this test and the last is the simulation step size; it was halved to 5×10^{-7} seconds. As was revealed in the fuzzy-logic controller, simulation step size could play a big role in how effective the controller is. Comparing the average and maximum displacement and current from the last test shows no significant changes. Looking at the time domain responses from Figures 3.107 through 3.109 possibly shows a small change in the manner that the controller converges. In the previous test (Figures 3.99 through 3.101), there was a small swell in the peak displacements up until about 0.5 seconds before it trended towards its final steady state value. In contrast, this test showed an almost continuous decline towards its steady state value. The IF plots (Figures 3.110 through 3.114) show similar values compared to the last test; including the downward trend of the low-frequency modes. Therefore, decreasing simulation step size improves

WFXLMS controller rate of convergence, but does not change the overall stability of the system like the fuzzy-logic controller.

3.3.9 Test 9

The flywheel parameters used for this test are listed in Table 3.31. From these testing conditions, the average and maximum values for the current and position in Table 3.32 were determined.

Table 3.31: WFXLMS test 9 conditions.

Term	Value	Units
ω	100000	rpm
	1667	Hz
dt	5×10^{-6}	s
I_{0r}	4	A
I_{0z}	4	A
i_{supply}	20	A
$i_{supplyz}$	20	A
N	512	
eG	1	
eGz	1	
W1	5	
W1z	5	
μ_1	5×10^{-4}	
μ_2	5×10^{-4}	
μ_{1z}	1×10^{-8}	
μ_{2z}	1×10^{-8}	
t_{end}	1.25	

The time domain response of the FES system at the three bearings are shown in Figures 3.115 through 3.117.

An instantaneous frequency (IF) plot of each temporal response was generated to evaluate the stability in the frequency domain and is shown in Figures 3.118 through 3.122.

Table 3.32: WFXLMS test 9 results.

Term	Axis	Average	Maximum
	x	4.67×10^{-1}	3.08×10^{0}
Current (A)	y	5.39×10^{-1}	3.54×10^{0}
	z	3.35×10^{-7}	2.82×10^{-6}
	x	1.32×10^{-6}	8.72×10^{-6}
Magnitude (m)	y	1.53×10^{-6}	1.00×10^{-5}
	z	5.93×10^{-12}	4.98×10^{-11}
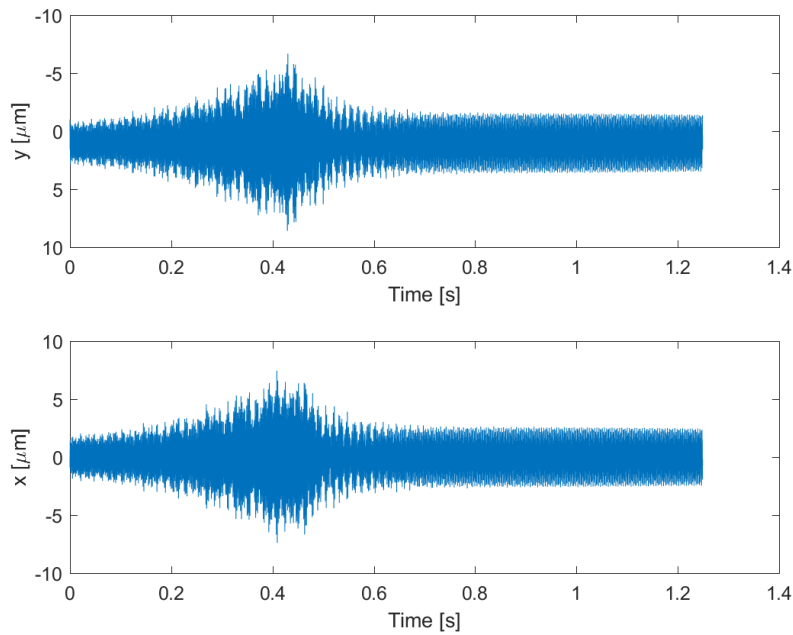
Figure 3.115: WFXLMS test 9: independent bearing A temporal responses.

The raw data generated for each bearing had significant signal processing noise due to the nature of the IF calculations process. Therefore, a smoothing function was applied to this data to reveal the frequency trends and omit unnecessary data outliers. When comparing the raw plot with the smoothed plot, there was not a noticeable difference in the general trend of the data. Therefore, it is reasonable to assume that these plots do an adequate job depicting the controller's stability in the frequency domain.
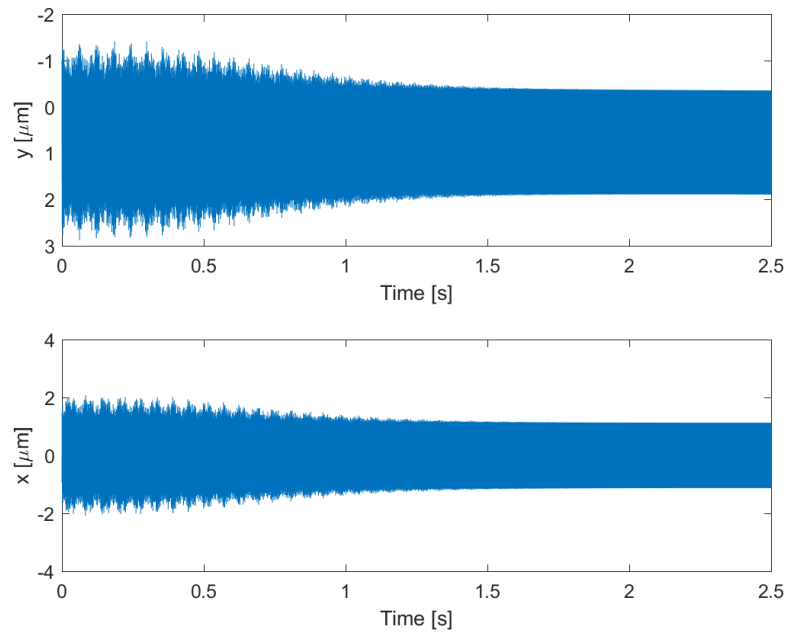
Figure 3.116: WFXLMS test 9: independent bearing B temporal responses.
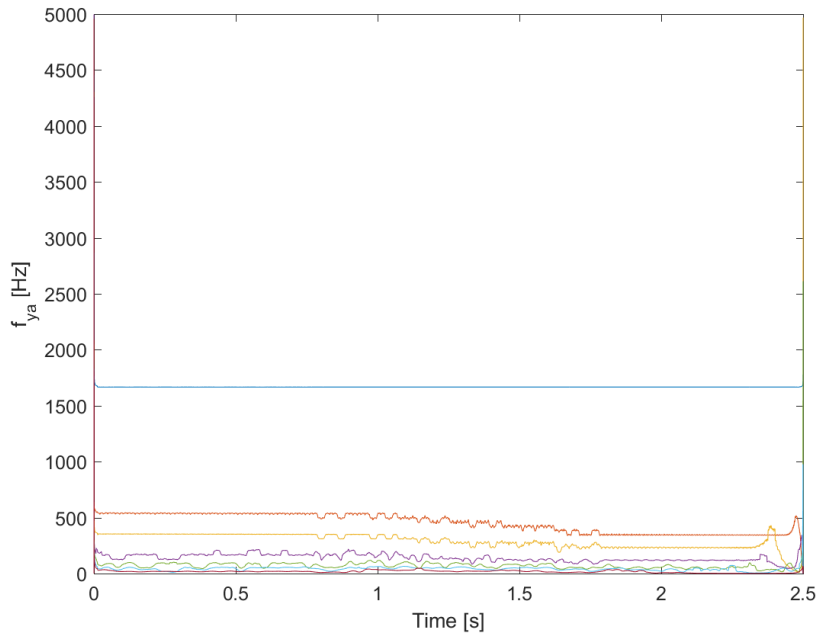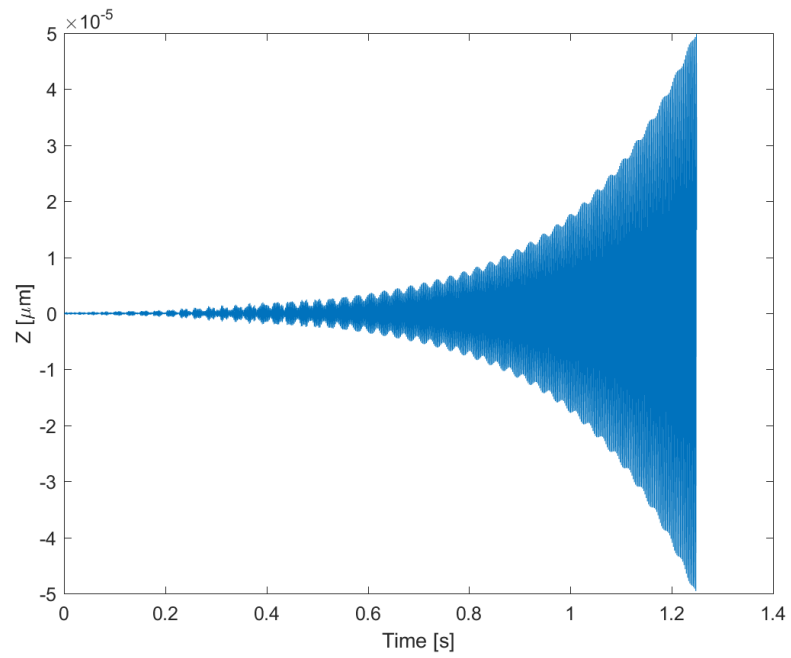

Figure 3.117: WFXLMS test 9: thrust bearing.

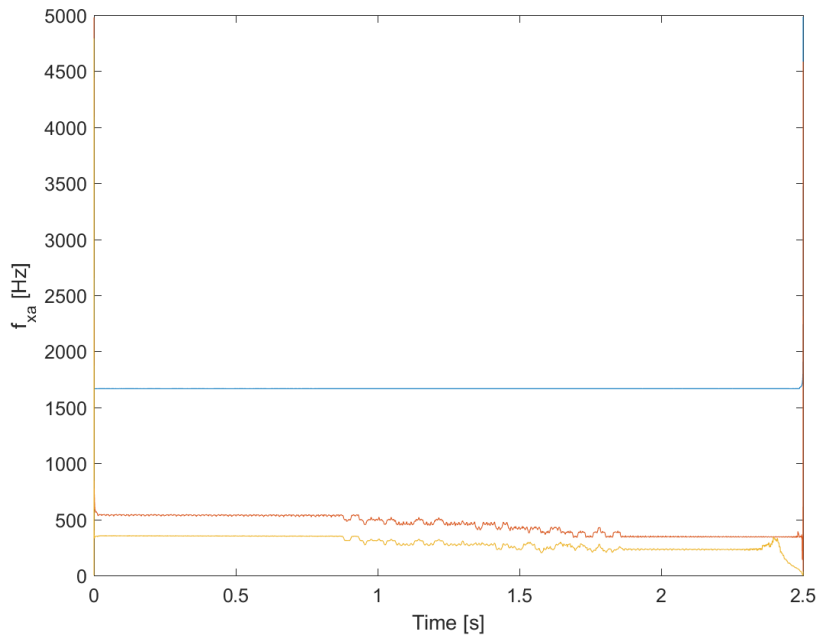Figure 3.118: WFXLMS test 9: bearing A IF response for *y*-axis.

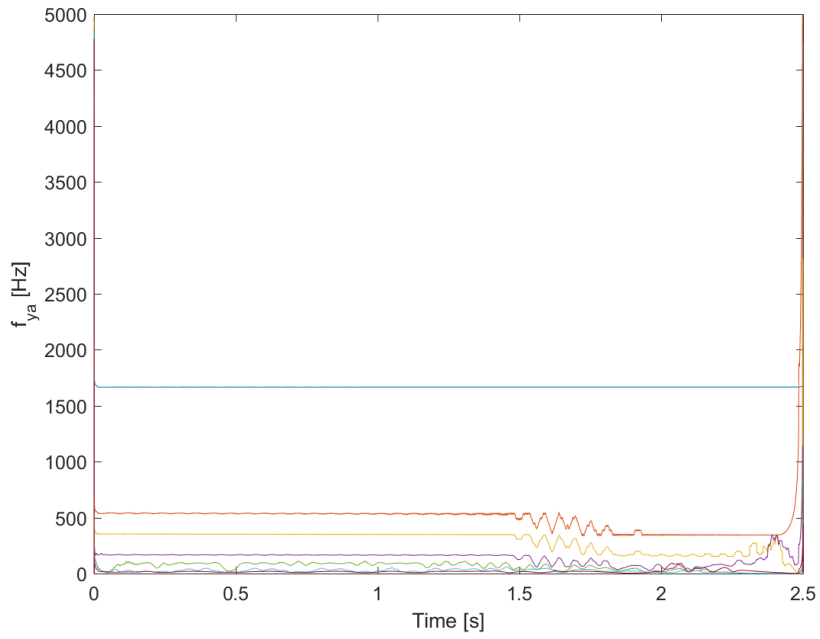Figure 3.119: WFXLMS test 9: bearing A IF response for *x*-axis.

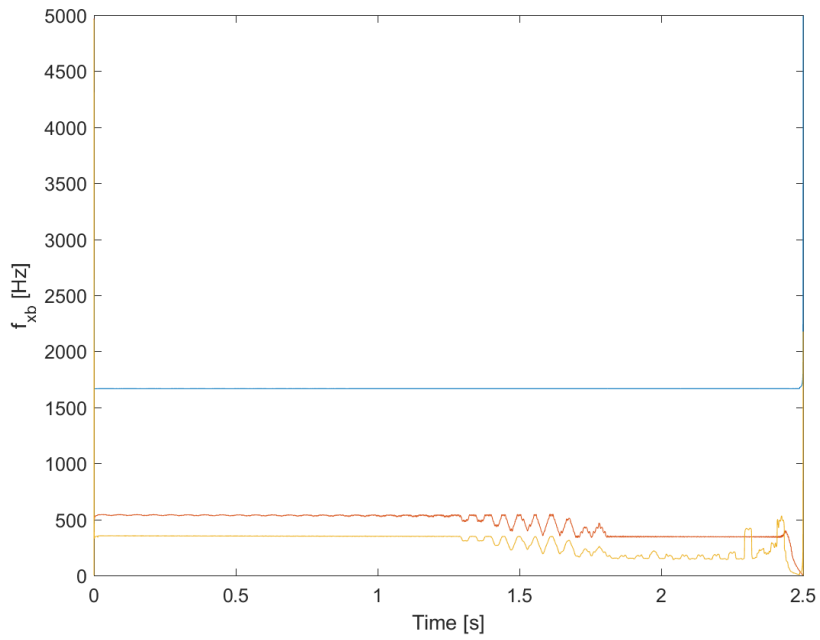Figure 3.120: WFXLMS test 9: bearing B IF response for *y*-axis.

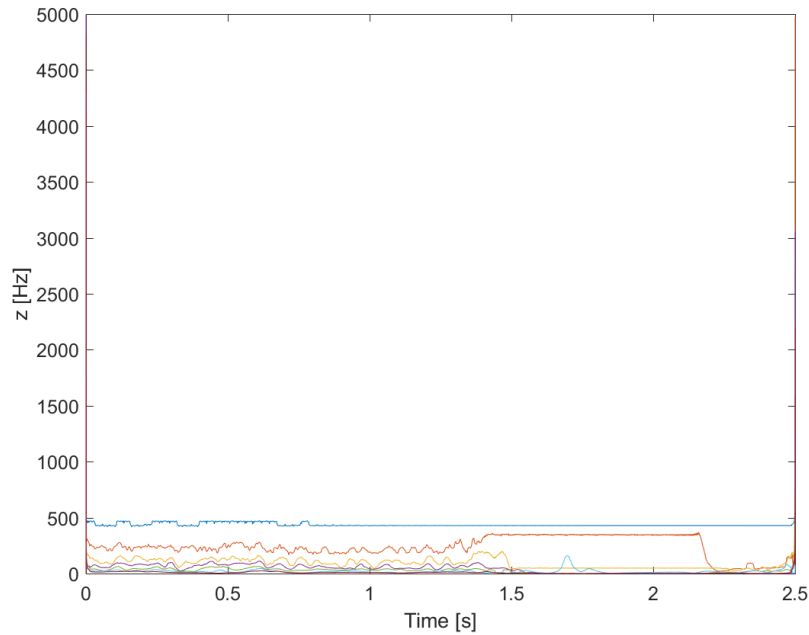Figure 3.121: WFXLMS test 9: bearing B IF response for *x*-axis.

Figure 3.122: WFXLMS test 9: thrust bearing IF response.

This test increased the step size by an order of magnitude from the last test to 5×10^{-6} seconds. This test was not run to completion because, again, divergence was observed in the z-axis, and this time it happened much quicker. Interestingly, this simulation drew over three times more maximum current than the previous test. This is likely caused by the controller reacting quickly to less data; causing it to overshoot the necessary value. The IF plots for this test (Figures 3.118 through 3.122) seem to match up with the previous test except the low-frequency modes seem smoother and went away completely in the z-axis. Therefore, it is reasonable to assume that larger simulation step sizes will result in similar dynamic behavior in the time and frequency domains, but will have larger peak and average current and displacements values.

3.3.10 Test 10

The flywheel parameters used for this test are listed in Table 3.33. From these testing conditions, the average and maximum values for the current and position in Table 3.34 were determined.

Table 3.33: WFXLMS test 10 conditions.

Term	Value	Units
ω	100	rpm
	1.67	Hz
dt	1×10^{-6}	s
I_{0r}	4	A
I_{0z}	4	A
i_{supply}	20	A
$i_{supplyz}$	20	A
N	512	
eG	1	
eGz	1	
W1	5	
W1z	5	
μ_1	5×10^{-4}	
μ_2	5×10^{-4}	
μ_{1z}	1×10^{-8}	
μ_{2z}	1×10^{-8}	
t_{end}	2.5	

Table 3.34: WFXLMS test 10 results.

Term	Axis	Average	Maximum
Current (A)	x	3.10×10^{-2}	1.80×10^{-1}
	y	3.41×10^{-1}	1.24×10^{0}
	z	1.29×10^{-7}	4.90×10^{-7}
Magnitude (m)	x	8.76×10^{-8}	5.10×10^{-7}
	y	9.78×10^{-7}	3.51×10^{-6}
	z	2.29×10^{-12}	8.66×10^{-12}

The time domain response of the FES system at the three bearings are shown in Figures 3.123 through 3.125.
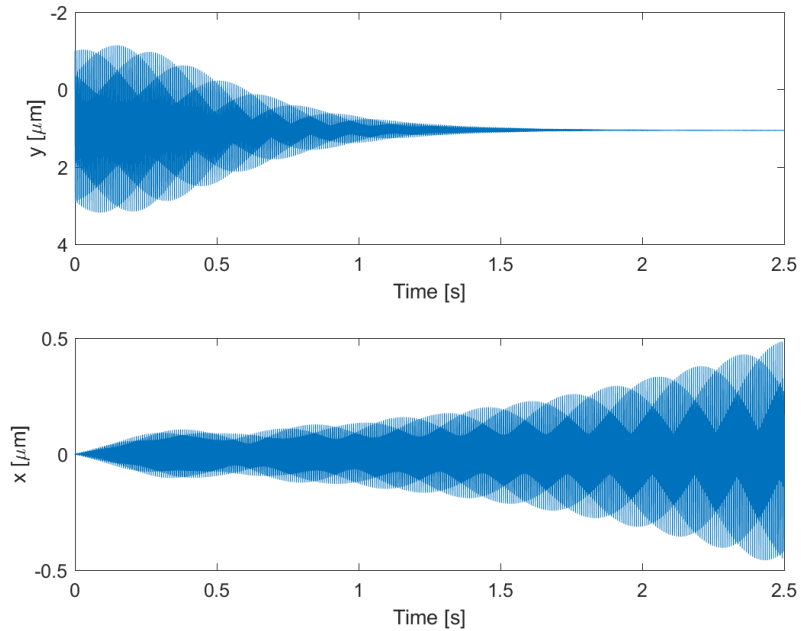
Figure 3.123: WFXLMS test 10: independent bearing A temporal responses.

An instantaneous frequency (IF) plot of each temporal response was generated to evaluate the stability in the frequency domain and is shown in Figures 3.126 through 3.130. The raw data generated for each bearing had significant signal processing noise due to the nature of the IF calculations process. Therefore, a smoothing function was applied to this data to reveal the frequency trends and omit unnecessary data outliers. When comparing the raw plot with the smoothed plot, there was not a noticeable difference in the general trend of the data. Therefore, it is reasonable to assume that these plots do an adequate job depicting the controller's stability in the frequency domain.
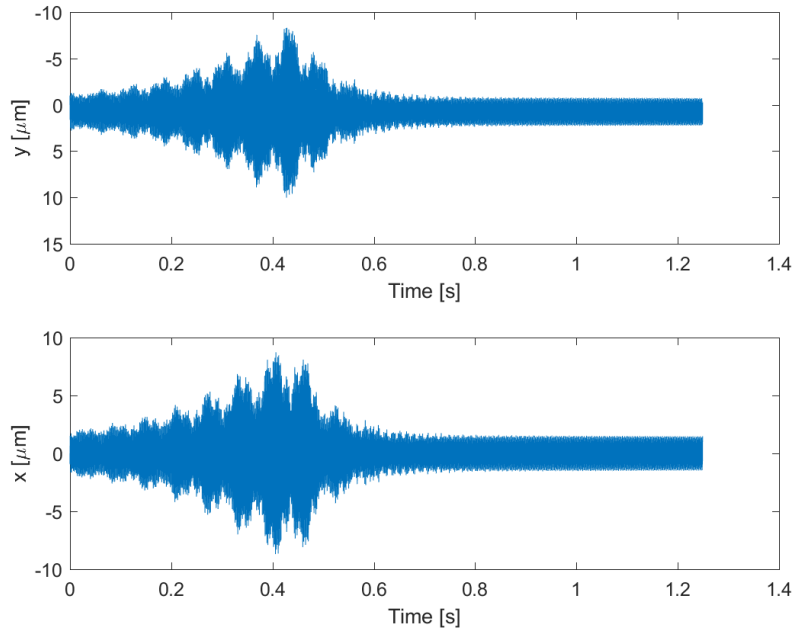
Figure 3.124: WFXLMS test 10: independent bearing B temporal responses.
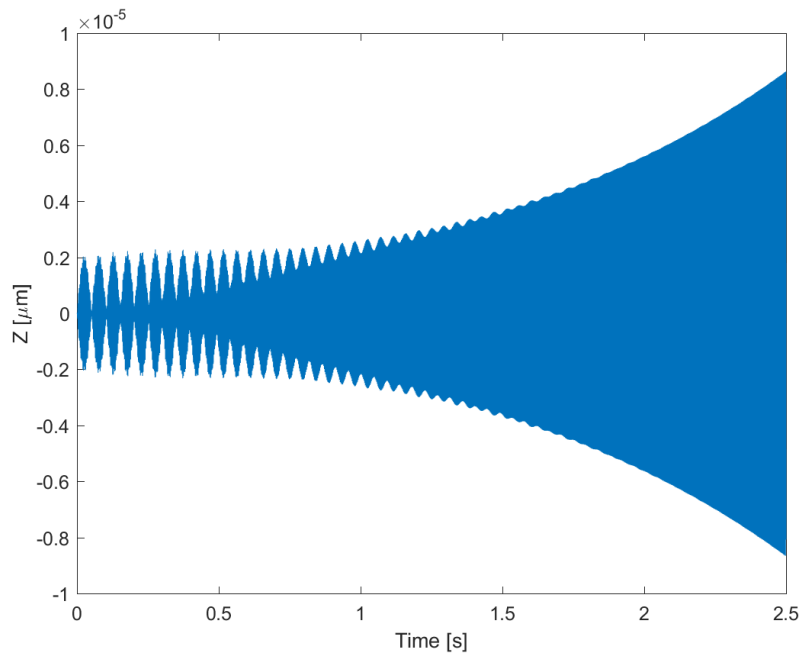
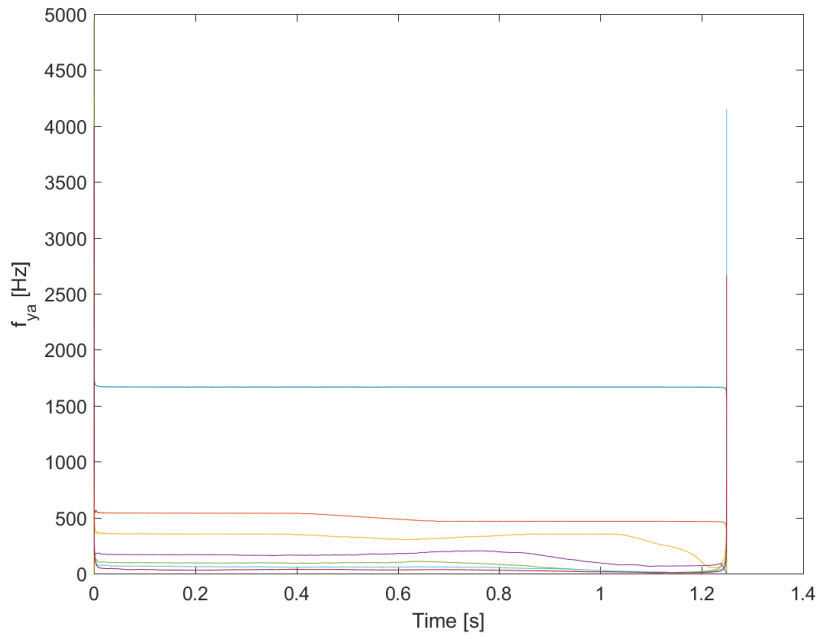Figure 3.125: WFXLMS test 10: thrust bearing.
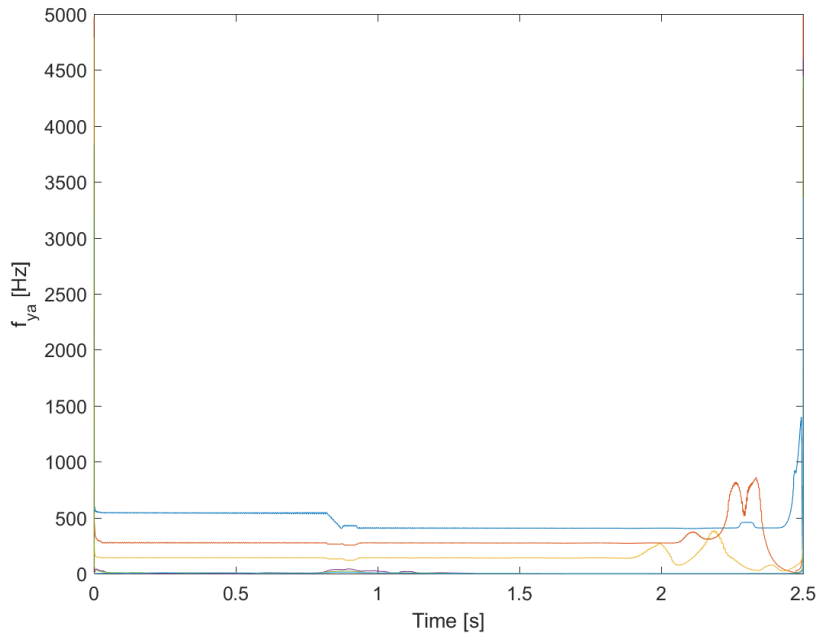
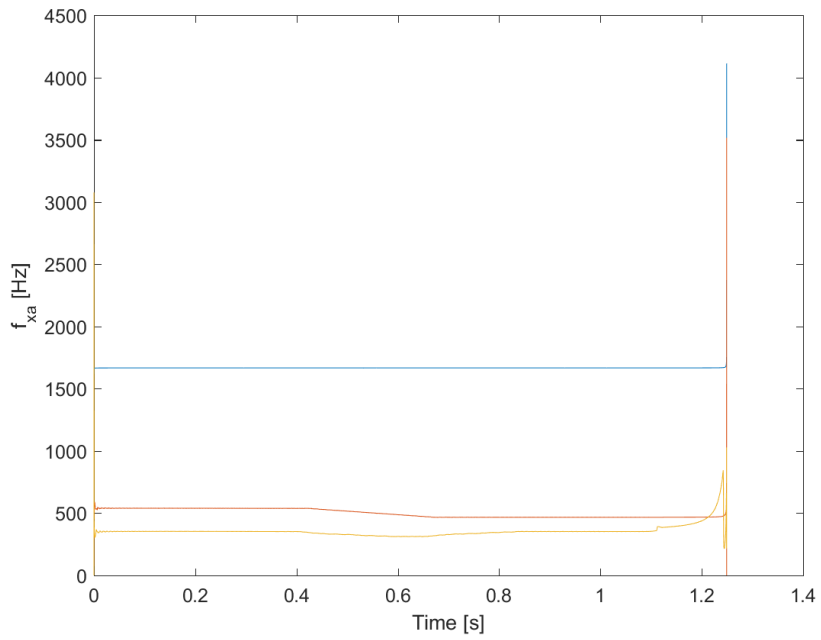Figure 3.126: WFXLMS test 10: bearing A IF response for *y*-axis.
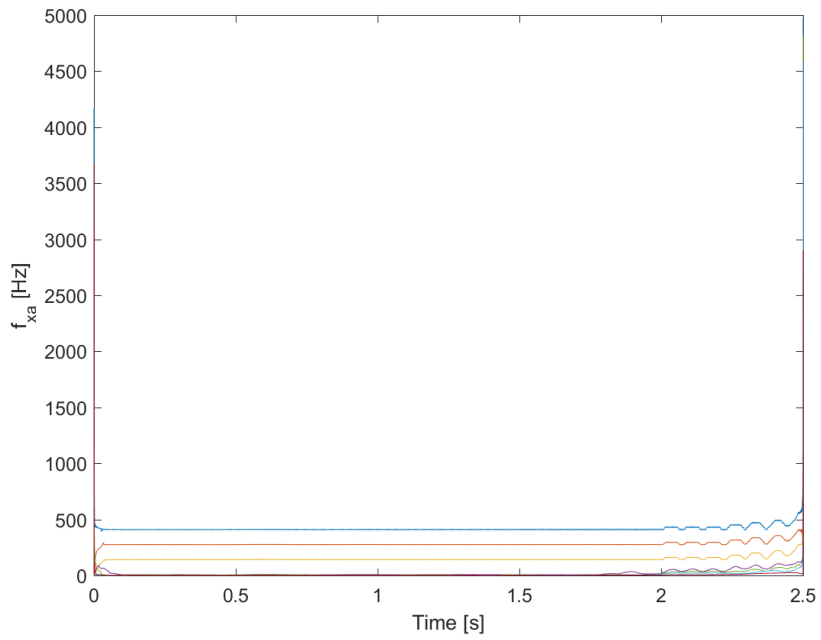
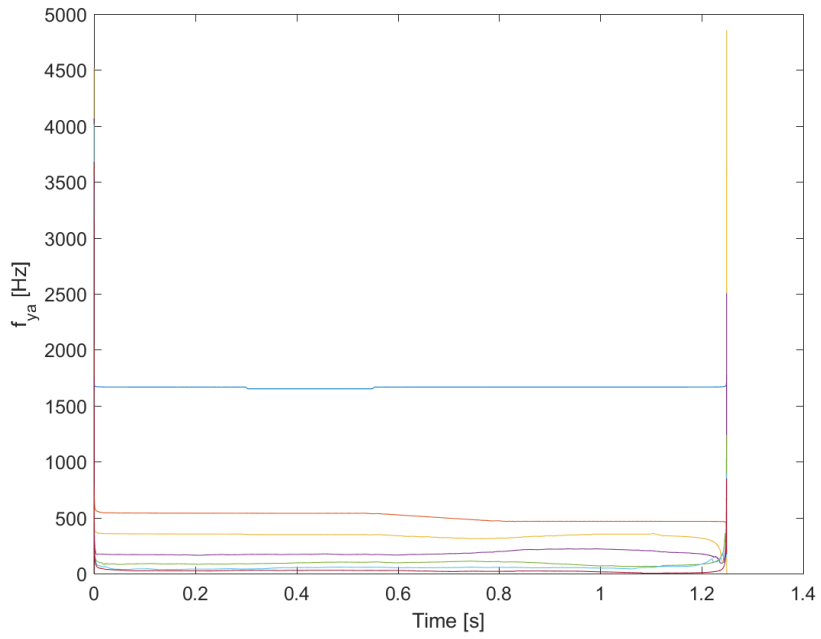Figure 3.127: WFXLMS test 10: bearing A IF response for *x*-axis.
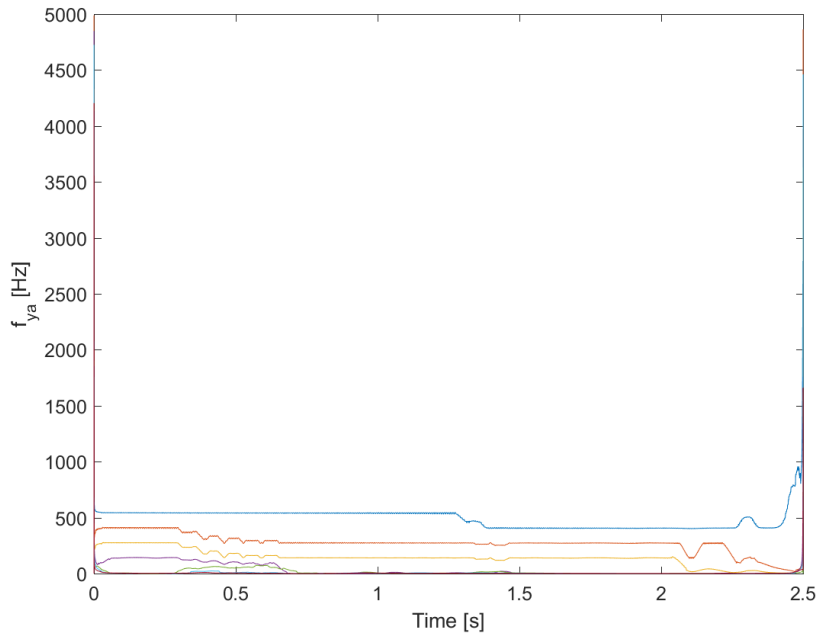
Figure 3.128: WFXLMS test 10: bearing B IF response for *y*-axis.

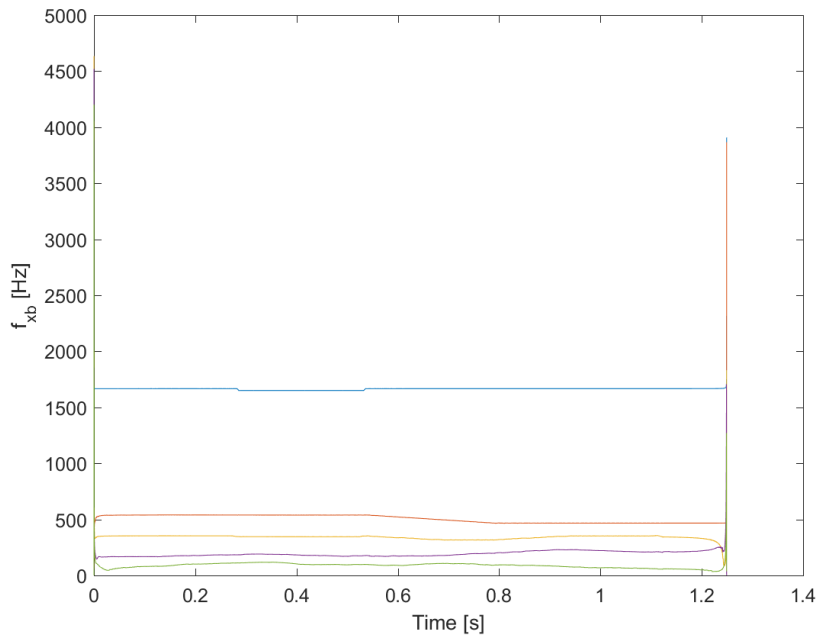

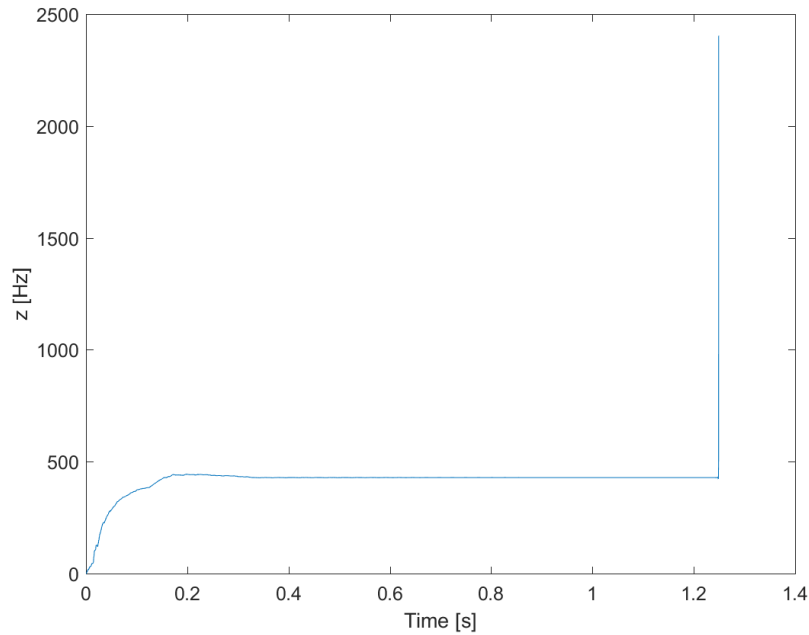Figure 3.129: WFXLMS test 10: bearing B IF response for *x*-axis.

Figure 3.130: WFXLMS test 10: thrust bearing IF response.

This test used the same parameters as test 7 except this time the rotor was slowed down to 100 rpm to see if the system was spinning too fast to control. While the new operating speed did dramatically alter the dynamic behavior of the FES system, it still did not converge. In fact, a new diverging behavior can be observed in the x-axis for bearing A and B (Figures 3.123 and 3.124). The most likely cause for this new behavior has to do with the geometric coupling effects. Because the controller brings the y-axis to a tighter level of control (a more consistent displacement), the force applied by the coupling effect becomes more constant in the x-axis with time. As the previous tests have shown, this controller takes nearly 0.5 seconds to learn the system and adapt its coefficients appropriately. Therefore, applying a force that becomes more constant with time would have a diverging effect in the x-axis until the coupling effect reached steady state.

Despite the instability in the time domain, the controller again demonstrates effective control in the frequency domain. Figures 3.126 through 3.130 depict steady state frequency modes throughout the simulation. This indicates both the strength and weakness of this controller. It is good at controlling in the frequency domain, but is slow to react in the time domain. Perhaps this suggests that it should be combined with a PID or fuzzy-logic controller for best results.

3.3.11   Test 11

The flywheel parameters used for this test are listed in Table 3.35. From these testing conditions, the average and maximum values for the current and position in Table 3.36 were determined.

Table 3.35: WFXLMS test 11 conditions.

Term	Value	Units
ω	100000	rpm
	1667	Hz
dt	1×10^{-5}	s
I_{0r}	4	A
I_{0z}	4	A
i_{supply}	100	A
$i_{supplyz}$	100	A
N	128	
eG	1	
eGz	1	
W1	0.5	
W1z	0.5	
μ_1	1×10^{-4}	
μ_2	1×10^{-4}	
μ_{1z}	1×10^{-4}	
μ_{2z}	1×10^{-4}	
t_{end}	2.5	

Table 3.36: WFXLMS test 11 results.

Term	Axis	Average	Maximum
	x	2.56×10^{-1}	2.29×10^{0}
Current (A)	y	4.12×10^{-1}	2.69×10^{0}
	z	1.47×10^{-1}	4.00×10^{0}
	x	1.46×10^{-6}	1.32×10^{-5}
Magnitude (m)	y	2.39×10^{-6}	1.54×10^{-5}
	z	1.05×10^{-6}	2.87×10^{-5}

The time domain response of the FES system at the three bearings are shown in Figures 3.131 through 3.133.
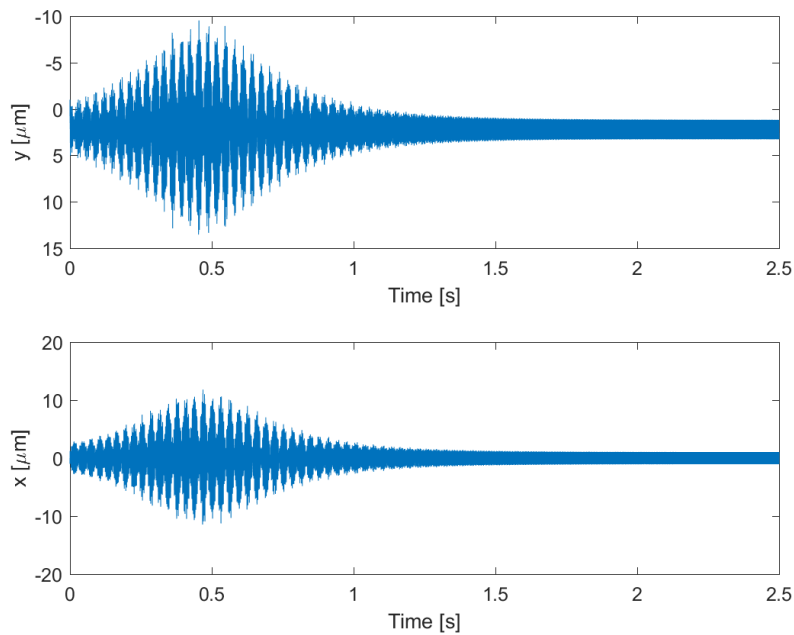
Figure 3.131: WFXLMS test 11: independent bearing A temporal responses.

An instantaneous frequency (IF) plot of each temporal response was generated to evaluate the stability in the frequency domain and is shown in Figures 3.134 through 3.138. The raw data generated for each bearing had significant signal processing noise due to the
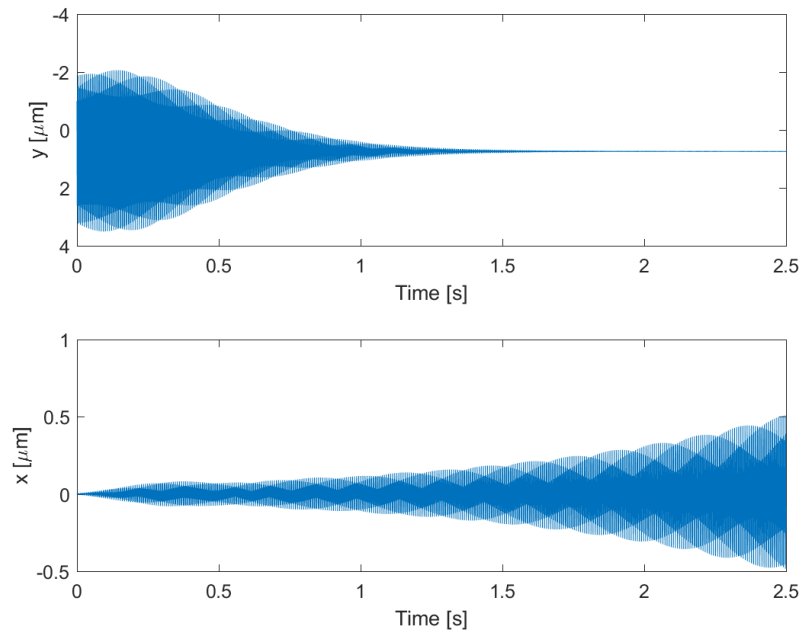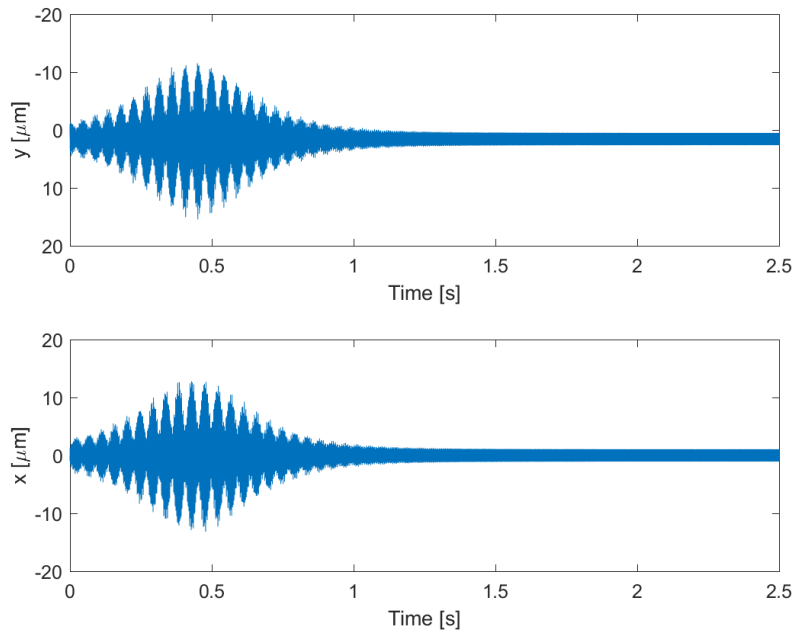
Figure 3.132: WFXLMS test 11: independent bearing B temporal responses.
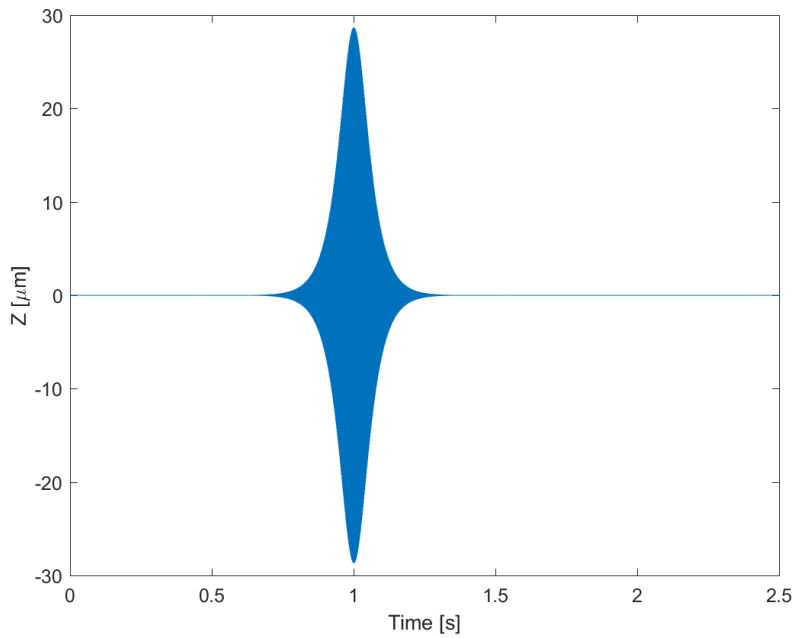
Figure 3.133: WFXLMS test 11: thrust bearing.

135

nature of the IF calculations process. Therefore, a smoothing function was applied to this data to reveal the frequency trends and omit unnecessary data outliers. When comparing the raw plot with the smoothed plot, there was not a noticeable difference in the general trend of the data. Therefore, it is reasonable to assume that these plots do an adequate job depicting the controller's stability in the frequency domain.
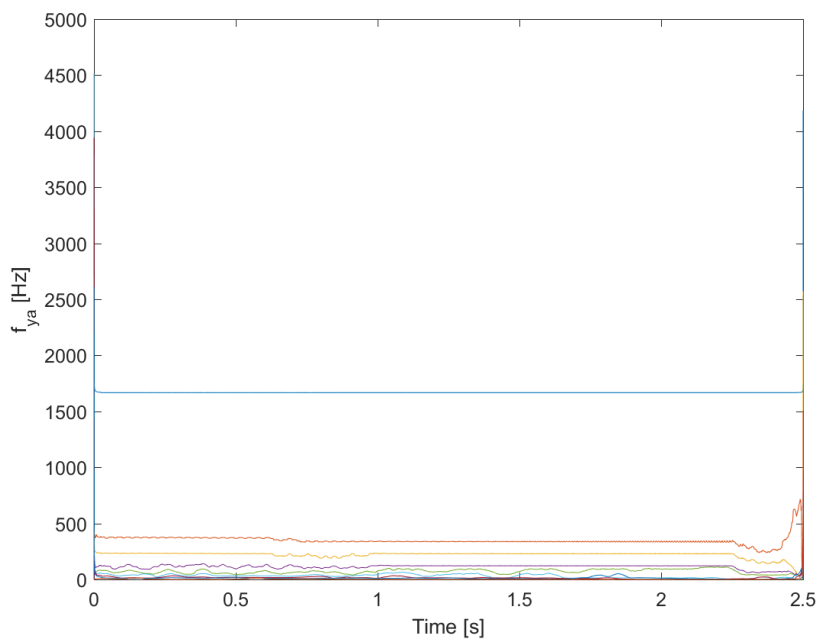
Figure 3.134: WFXLMS test 11: bearing A IF response for *y*-axis.

Since it is reasonable to run this simulation with a bigger step size - as verified in the previous test - the remaining tests were run with a bigger step size. The major change that this simulation had over others was a significant change in filter length (N) from 512 to 128. Many trials with this filter length created interested results. It seems that now, the *z*-axis does converge provided the oscillations get large enough first. Many simulations have

Figure 3.135: WFXLMS test 11: bearing A IF response for *x*-axis.

Figure 3.136: WFXLMS test 11: bearing B IF response for *y*-axis.
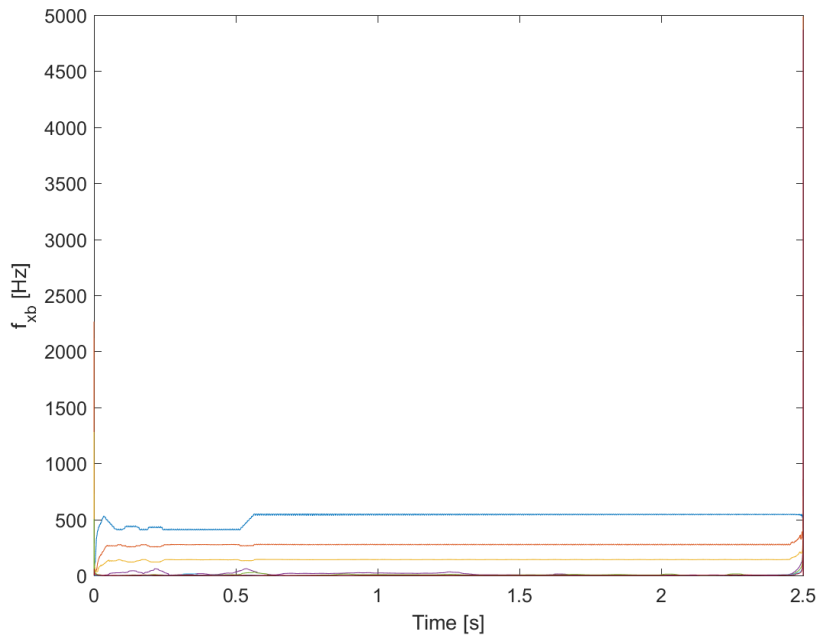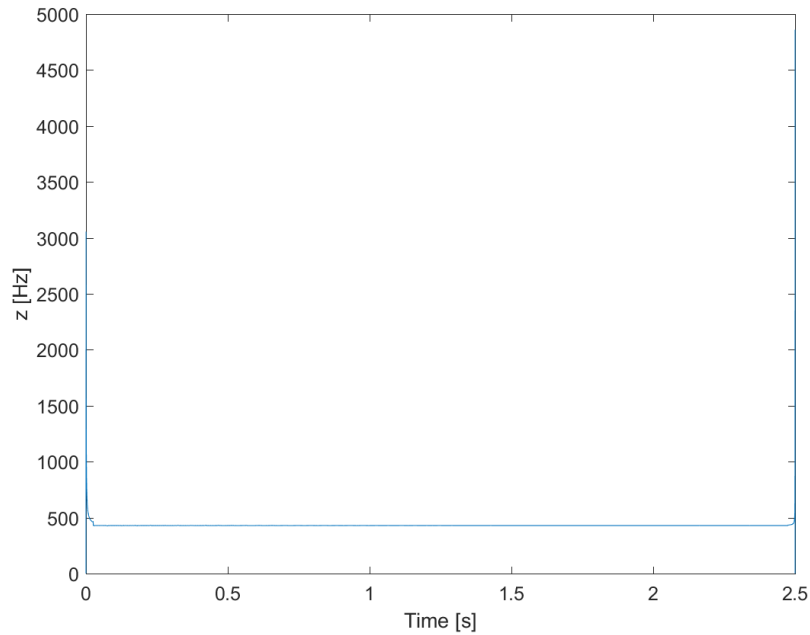
Figure 3.137: WFXLMS test 11: bearing B IF response for *x*-axis.

Figure 3.138: WFXLMS test 11: thrust bearing IF response.

revealed that this happens every time. Thus, it is reasonable to assume that this would have

happened in all the previous tests provided enough time was allowed.

Comparing values to the previous tests, the average current draw for this simulation

was much less than the PID and fuzzy-logic tests at 0.03 Amps in the *x*-axis and 0.3 Amps

in the *y*-axis. While this data looks like it converged, a linear trend line from 1.5 seconds

to the end of the simulation was created for the *y*-axis at bearing A and B to check for any

drifting away from 0 (Figures 3.139 and 3.140).

Figure 3.139: WFXLMS test 11: linear trend line for *y*-axis at bearing A.

Both linear trend lines depict a slight positive trend for the last second of the simu-

lation indicating that the controller is still sagging under the weight of gravity. This value

is so small that it could be considered 0. However, since the controller is pulling a small
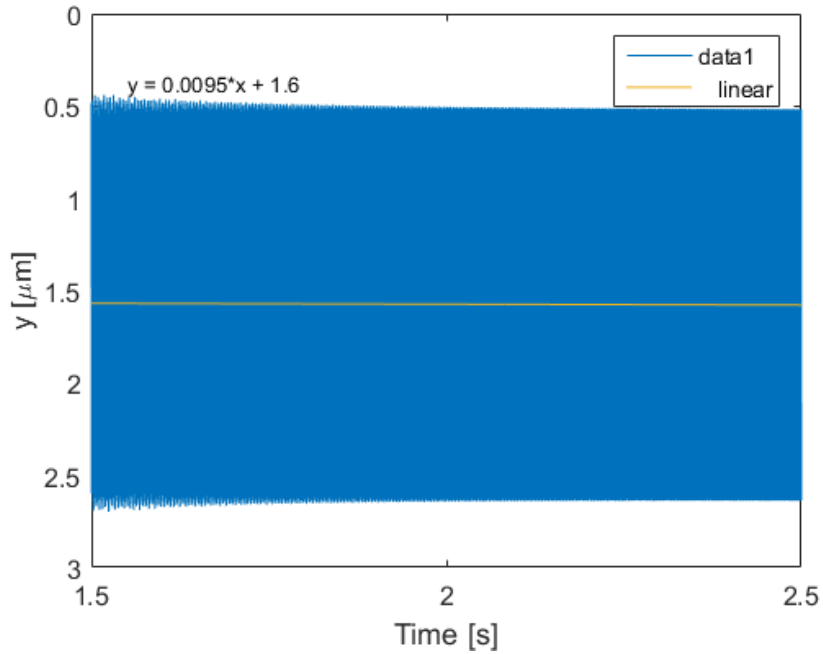
Figure 3.140: WFXLMS test 11: linear trend line for *y*-axis at bearing B.

current relative to the PID and fuzzy-logic controllers, the next step was to provide the controller with a larger supply current (i_{supply} and $i_{supplyz}$) or to increase the filter step size (μ_1, μ_2, μ_{1z}, and μ_{2z}) see if it will achieve stability quicker.

3.3.12 Test 12

The flywheel parameters used for this test are listed in Table 3.37. From these testing conditions, the average and maximum values for the current and position in Table 3.38 were determined.

The time domain response of the FES system at the three bearings are shown in Figures 3.141 through 3.143.

An instantaneous frequency (IF) plot of each temporal response was generated to evaluate the stability in the frequency domain and is shown in Figures 3.144 through 3.148.

140

Table 3.37: WFXLMS test 12 conditions.

Term	Value	Units
ω	100000	rpm
	1667	Hz
dt	1×10^{-5}	s
I_{0r}	4	A
I_{0z}	4	A
i_{supply}	100	A
$i_{supplyz}$	100	A
N	128	
eG	1	
eGz	1	
W1	0.5	
W1z	0.5	
μ_1	1×10^{-3}	
μ_2	1×10^{-3}	
μ_{1z}	1×10^{-3}	
μ_{2z}	1×10^{-3}	
t_{end}	2.5	

Figure 3.141: WFXLMS test 12: independent bearing A temporal responses.

Table 3.38: WFXLMS test 12 results.

Term	Axis	Average	Maximum
Current (A)	x	1.36×10^{-1}	7.98×10^{-1}
	y	3.30×10^{-1}	1.11×10^{0}
	z	4.68×10^{-2}	1.28×10^{0}
Magnitude (m)	x	7.71×10^{-7}	4.54×10^{-6}
	y	2.14×10^{-6}	6.38×10^{-6}
	z	3.36×10^{-7}	9.16×10^{-6}
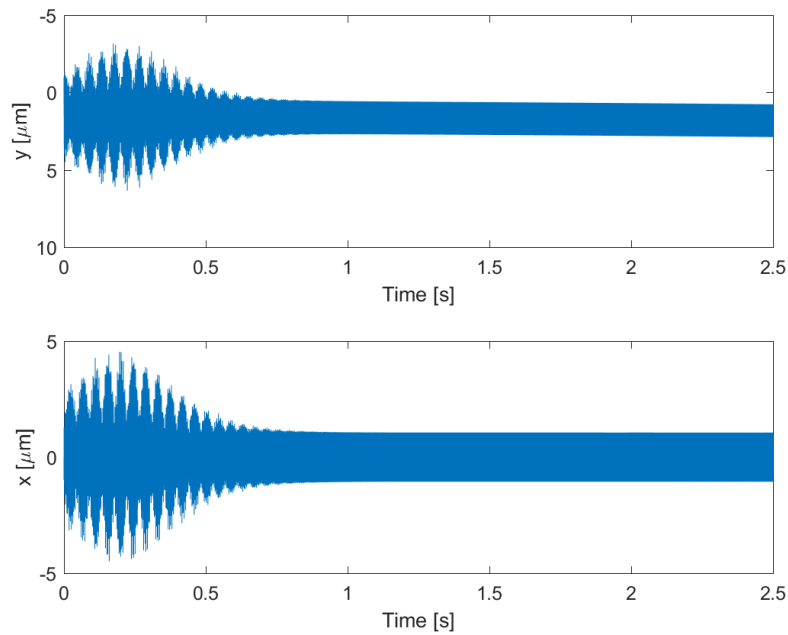
Figure 3.142: WFXLMS test 12: independent bearing B temporal responses.

The raw data generated for each bearing had significant signal processing noise due to the nature of the IF calculations process. Therefore, a smoothing function was applied to this data to reveal the frequency trends and omit unnecessary data outliers. When comparing the raw plot with the smoothed plot, there was not a noticeable difference in the general trend of the data. Therefore, it is reasonable to assume that these plots do an adequate job depicting the controller's stability in the frequency domain.

Figure 3.143: WFXLMS test 12: thrust bearing.

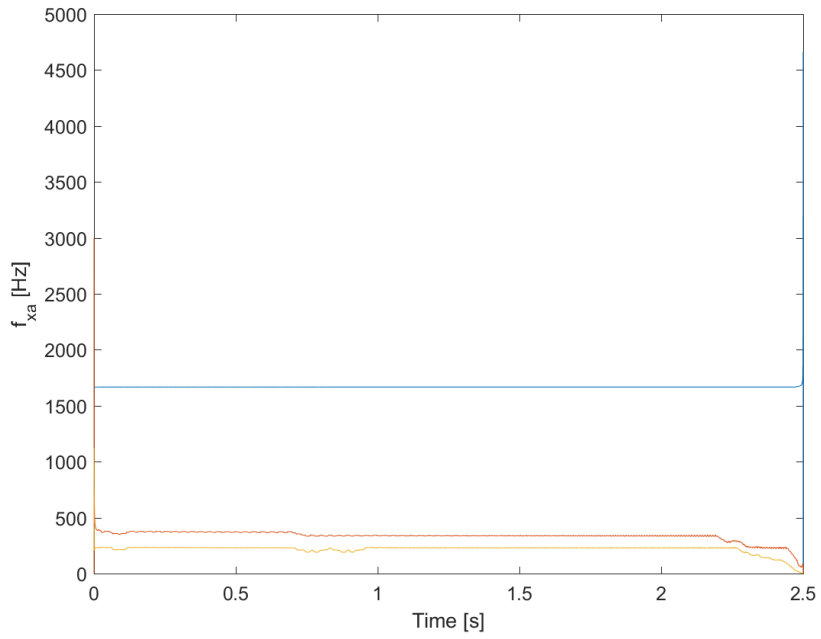Figure 3.144: WFXLMS test 12: bearing A IF response for *y*-axis.

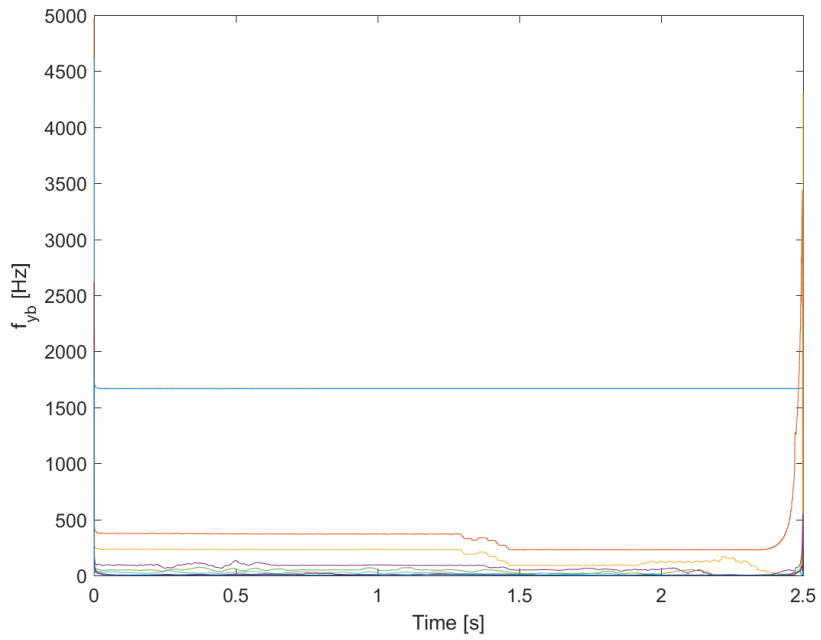Figure 3.145: WFXLMS test 12: bearing A IF response for *x*-axis.

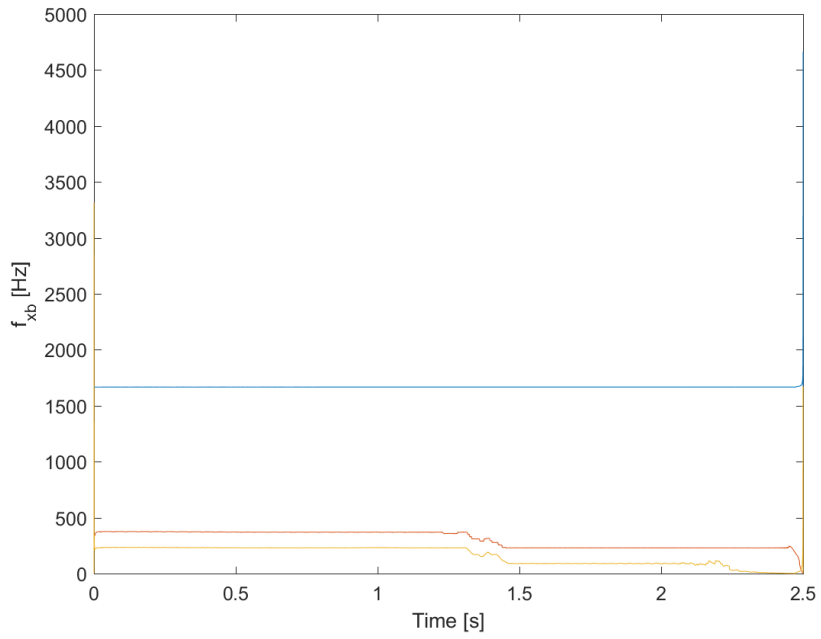Figure 3.146: WFXLMS test 12: bearing B IF response for *y*-axis.

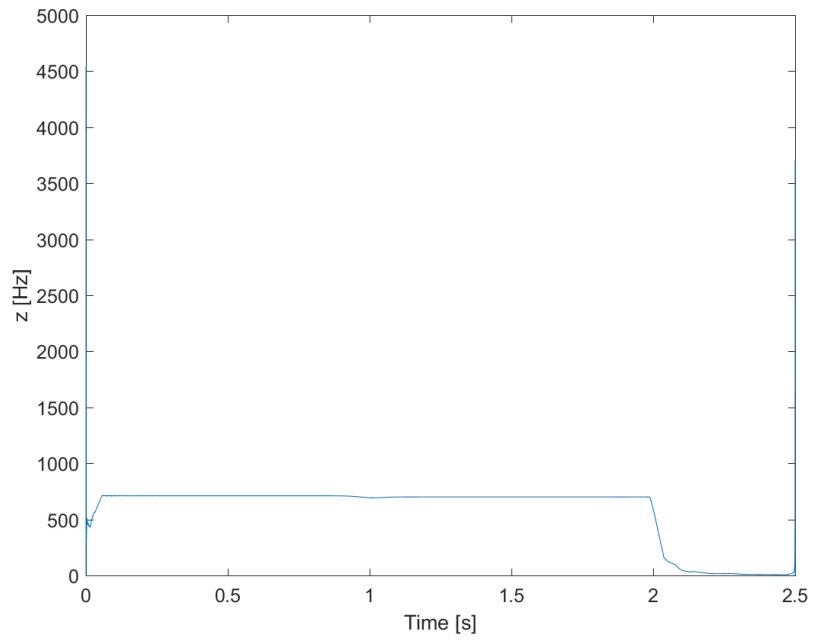Figure 3.147: WFXLMS test 12: bearing B IF response for *x*-axis.

Figure 3.148: WFXLMS test 12: thrust bearing IF response.

A linear trend line from 1.5 seconds to the end of the simulation was created for the *y*-axis at bearing A and B to quantify the drift away from 0 (Figures 3.149 and 3.150).
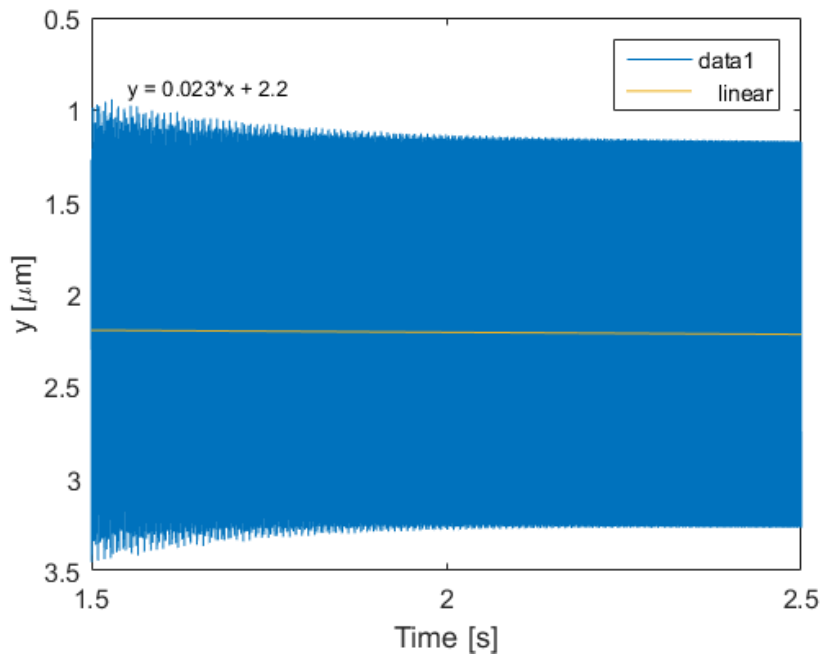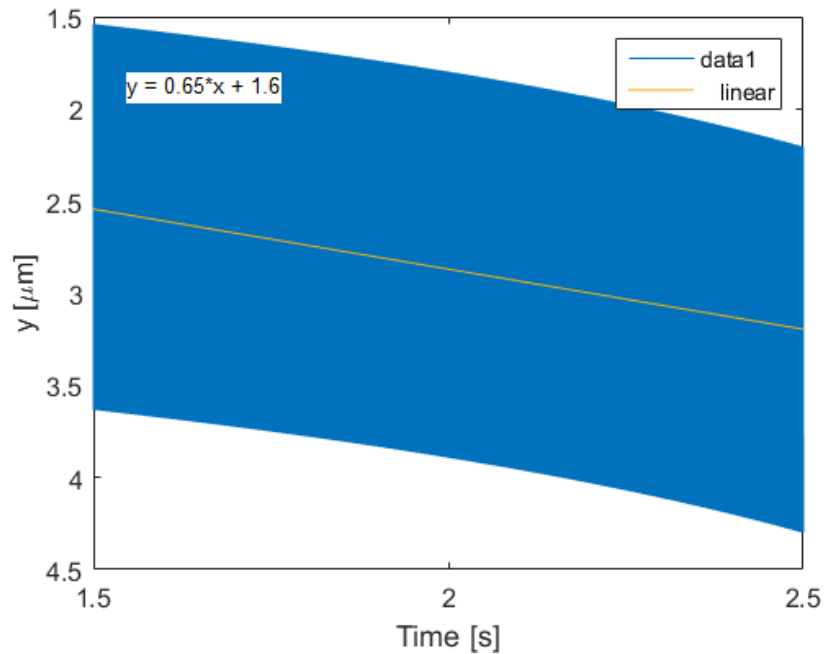

Figure 3.149: WFXLMS test 12: linear trend line for *y*-axis at bearing A.

In this case, increasing the filter step size actually decreased the active current draw from the controller by about 0.1 Amps for the journal bearing and 0.05 Amps for the thrust bearing. In addition, the mean and maximum displacements for both the journal and thrust bearings actually decreased as well. However, this new controller was much less stable 2.5 seconds into the simulation than the previous test with a maximum linear slope of about 0.65 $\mu m/s$. Drifting from 0 after 2.5 seconds is an undesirable trait for this controller as this indicates that any new load on the controller - such as an impulse force - would have a long settling time and could lead to a crash.

146
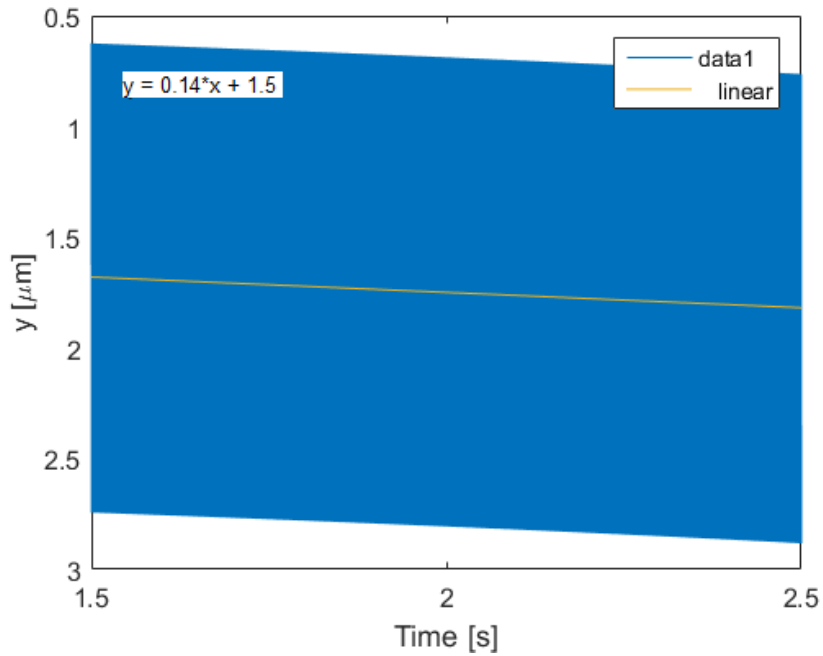
Figure 3.150: WFXLMS test 12: linear trend line for *y*-axis at bearing B.

3.3.13 Test 13

The flywheel parameters used for this test are listed in Table 3.39. From these testing conditions, the average and maximum values for the current and position in Table 3.40 were determined.

The time domain response of the FES system at the three bearings are shown in Figures 3.151 through 3.153.

An instantaneous frequency (IF) plot of each temporal response was generated to evaluate the stability in the frequency domain and is shown in Figures 3.154 through 3.158. The raw data generated for each bearing had significant signal processing noise due to the nature of the IF calculations process. Therefore, a smoothing function was applied to this

147

Table 3.39: WFXLMS test 13 conditions.

Term	Value	Units
ω	100000	rpm
	1667	Hz
dt	1×10^{-5}	s
I_{0r}	4	A
I_{0z}	4	A
i_{supply}	200	A
$i_{supplyz}$	200	A
N	128	
eG	1	
eGz	1	
W1	0.5	
W1z	0.5	
μ_1	1×10^{-3}	
μ_2	1×10^{-3}	
μ_{1z}	1×10^{-3}	
μ_{2z}	1×10^{-3}	
t_{end}	2.5	
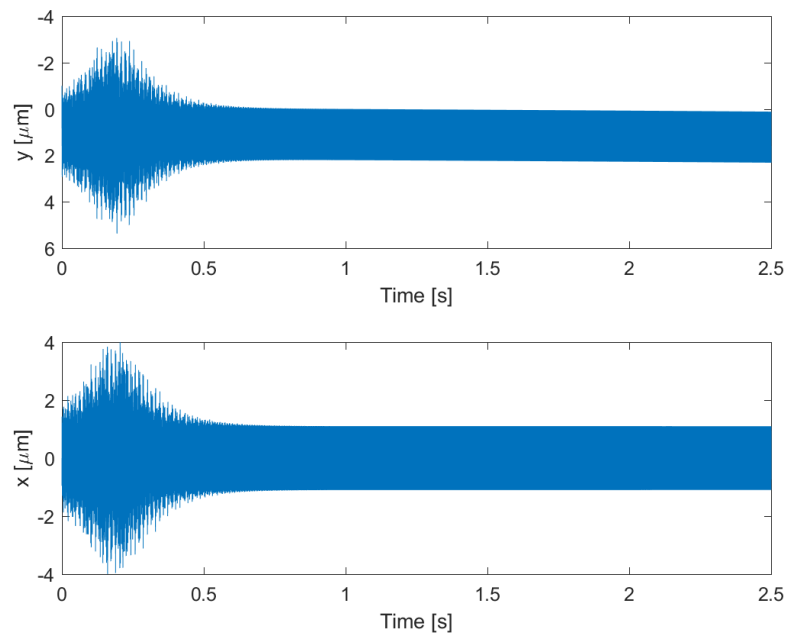
Figure 3.151: WFXLMS test 13: independent bearing A temporal responses.

Table 3.40: WFXLMS test 13 results.

Term	Axis	Average	Maximum
	x	2.73×10^{-1}	1.68×10^{0}
Current (A)	y	3.63×10^{-1}	2.04×10^{0}
	z	3.75×10^{-2}	5.07×10^{0}
	x	7.79×10^{-7}	4.80×10^{-6}
Magnitude (m)	y	1.08×10^{-6}	5.85×10^{-6}
	z	1.34×10^{-7}	1.82×10^{-5}
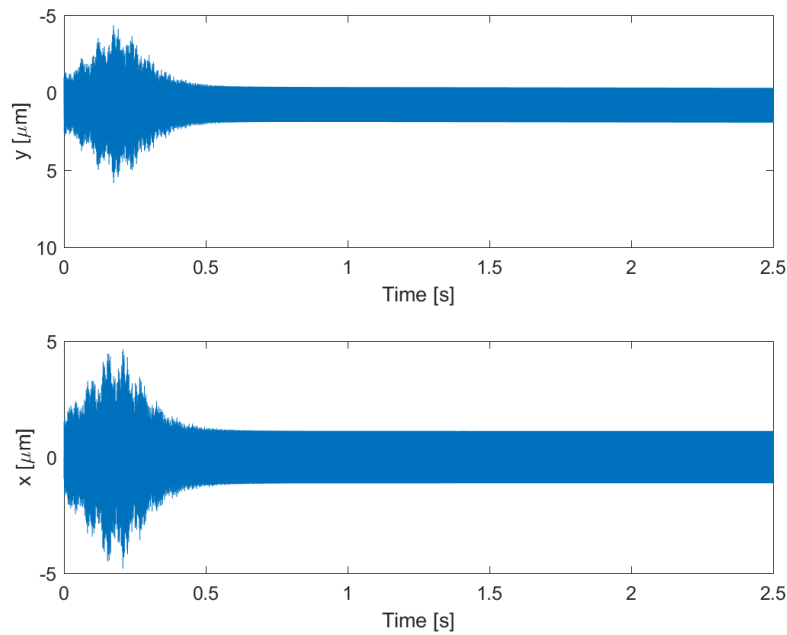
Figure 3.152: WFXLMS test 13: independent bearing B temporal responses.

data to reveal the frequency trends and omit unnecessary data outliers. When comparing the raw plot with the smoothed plot, there was not a noticeable difference in the general trend of the data. Therefore, it is reasonable to assume that these plots do an adequate job depicting the controller's stability in the frequency domain.
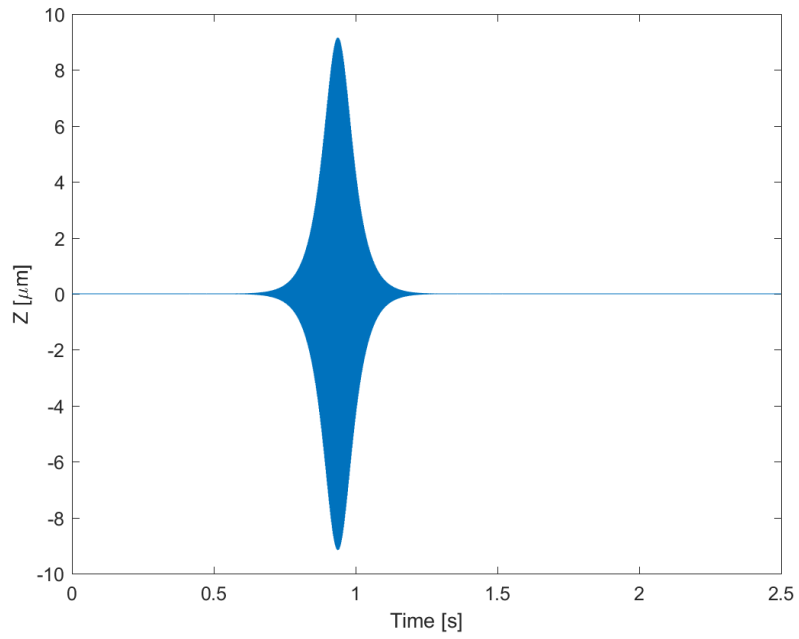
While this data looks like it converged, a linear trend line from 1.5 seconds to the end of the simulation was created for the y-axis at bearing A and B to quantify the drift
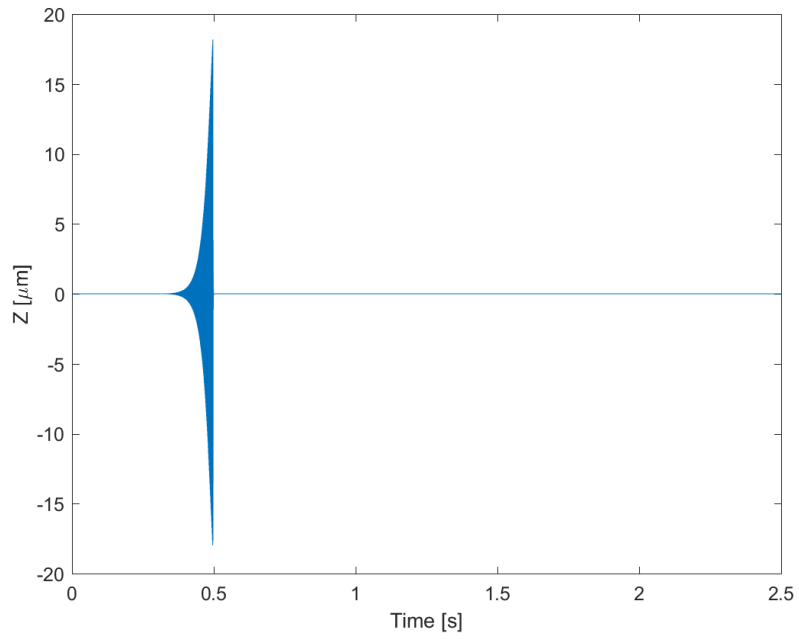
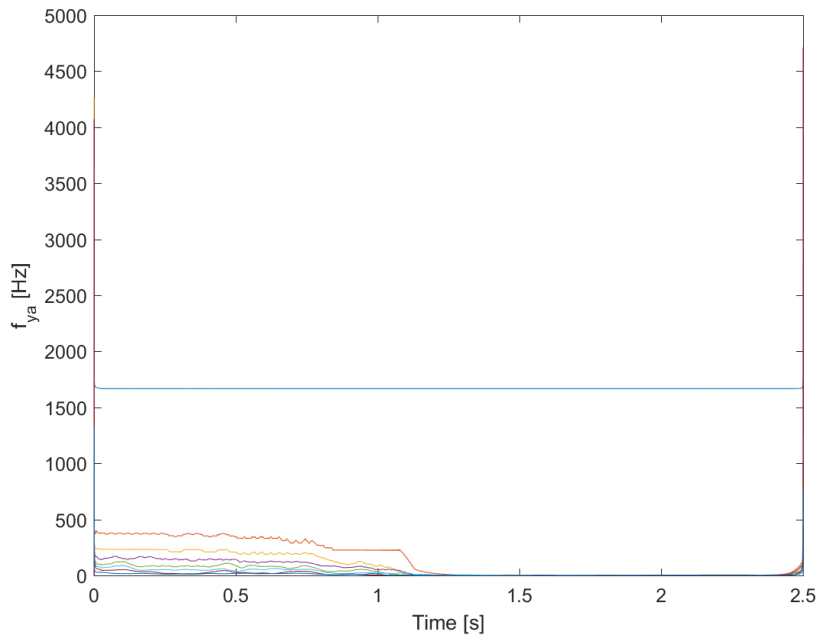Figure 3.153: WFXLMS test 13: thrust bearing.
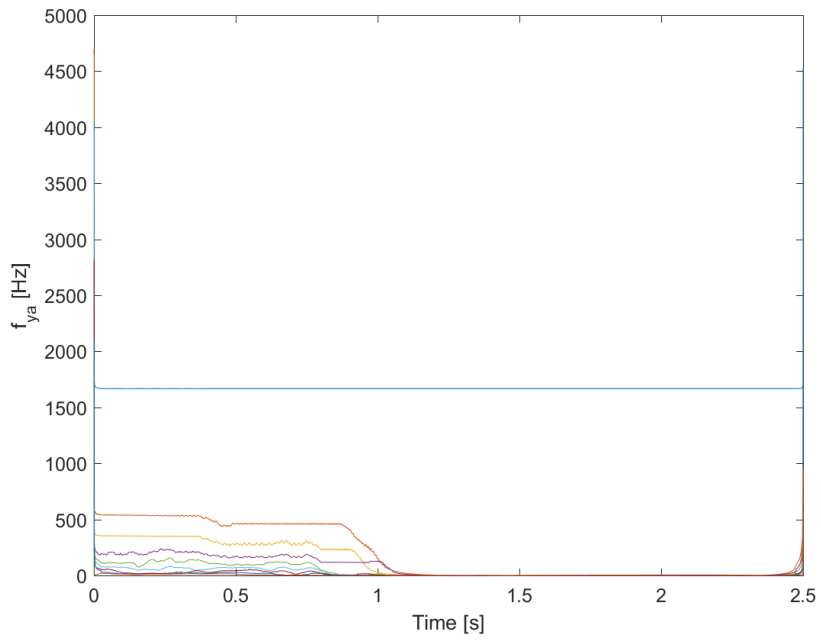
Figure 3.154: WFXLMS test 13: bearing A IF response for *y*-axis.
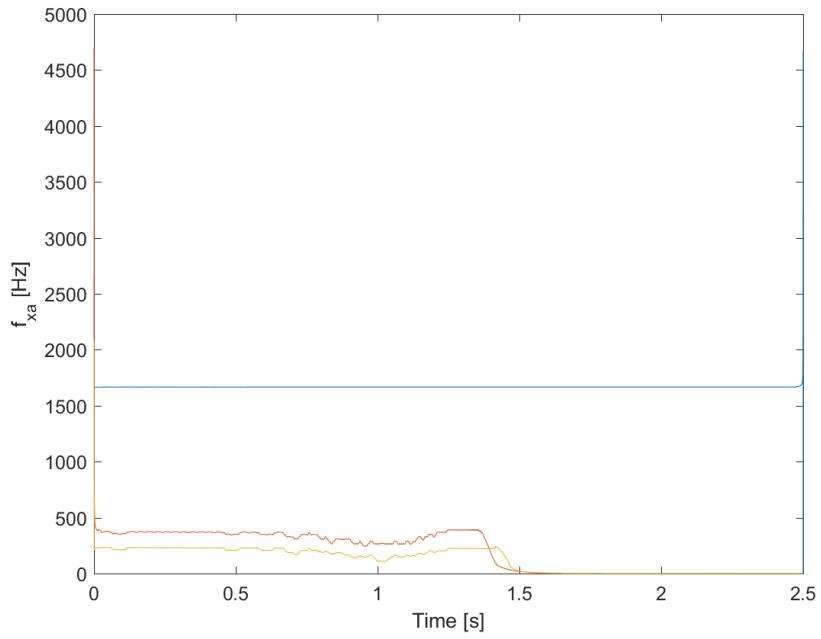
150
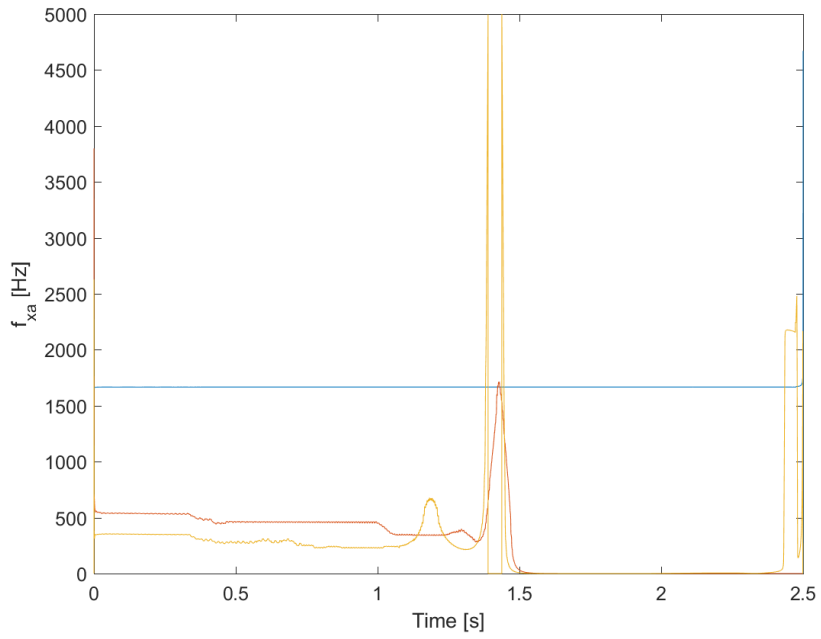
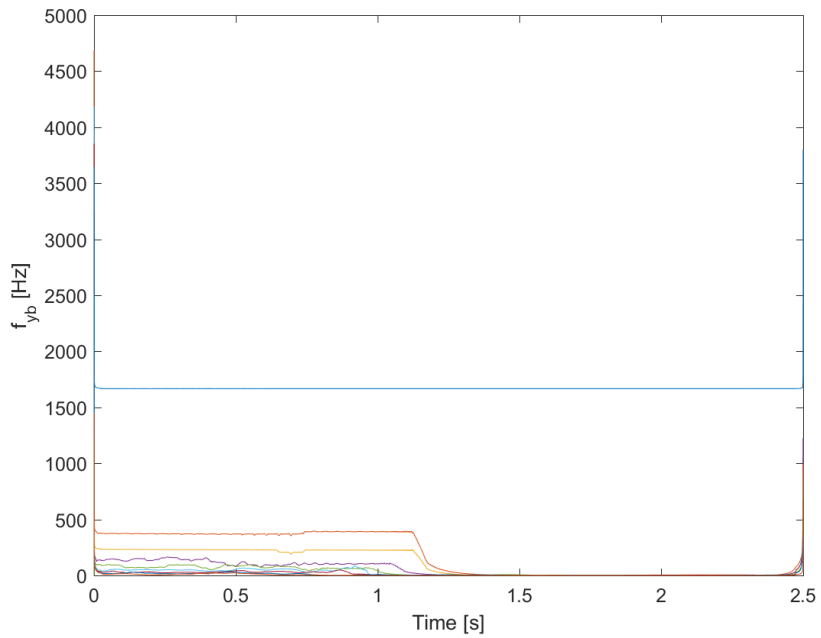Figure 3.155: WFXLMS test 13: bearing A IF response for *x*-axis.

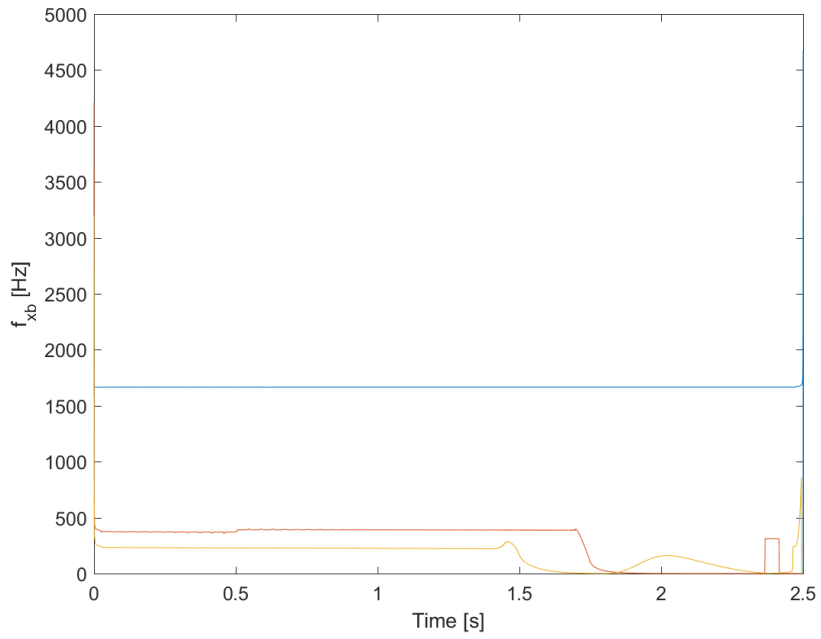Figure 3.156: WFXLMS test 13: bearing B IF response for *y*-axis.

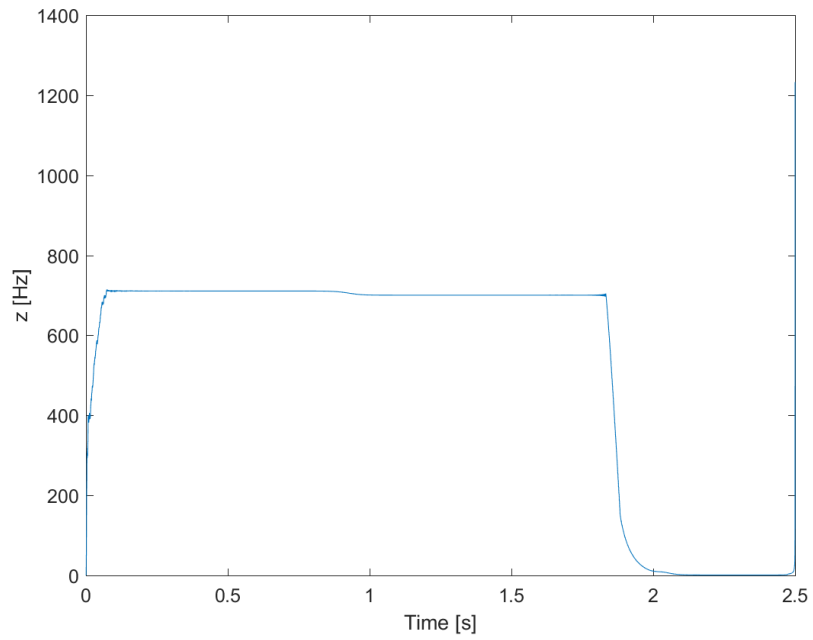Figure 3.157: WFXLMS test 13: bearing B IF response for *x*-axis.

Figure 3.158: WFXLMS test 13: thrust bearing IF response.

away from 0 and is shown in Figures 3.159 and 3.160.
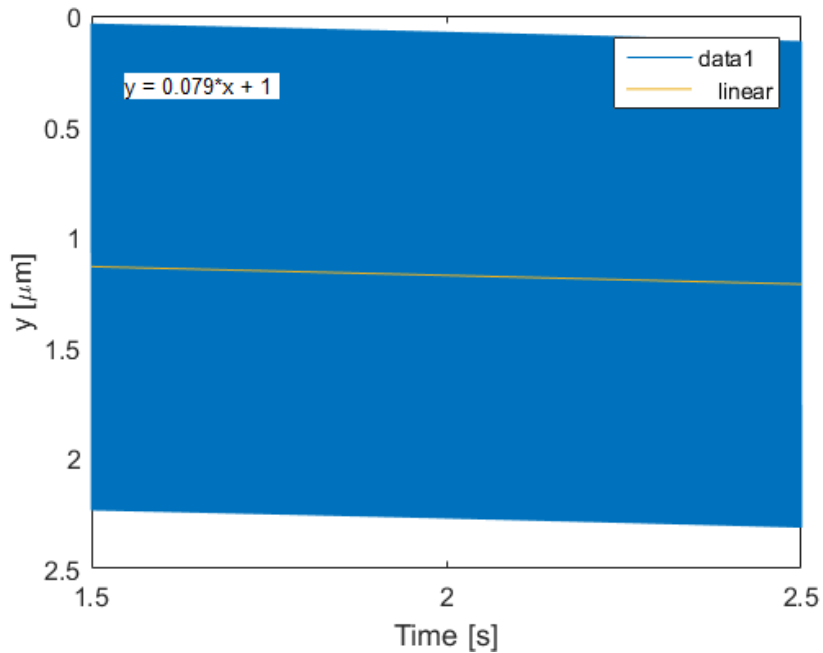
Figure 3.159: WFXLMS test 13: linear trend line for *y*-axis at bearing A.

The only thing that changed for this simulation from the last one was the supply current. It was increased from 100 Amps to 200 Amps. Increasing the supply current doubled the average and maximum current draw for the *x*-axis and doubled the maximum current draw for the *y*-axis but did not significantly increase the average current draw in the *y*-axis. The biggest change was observed in the maximum current draw in the *z*-axis which nearly increased by a factor of five.

However, a big change occurred with the average and maximum current and the magnitude of displacement for the *y*-axis. In particular, the average displacement of the *y*-axis was halved and the maximum displacement decreased by about 0.5 micrometers.
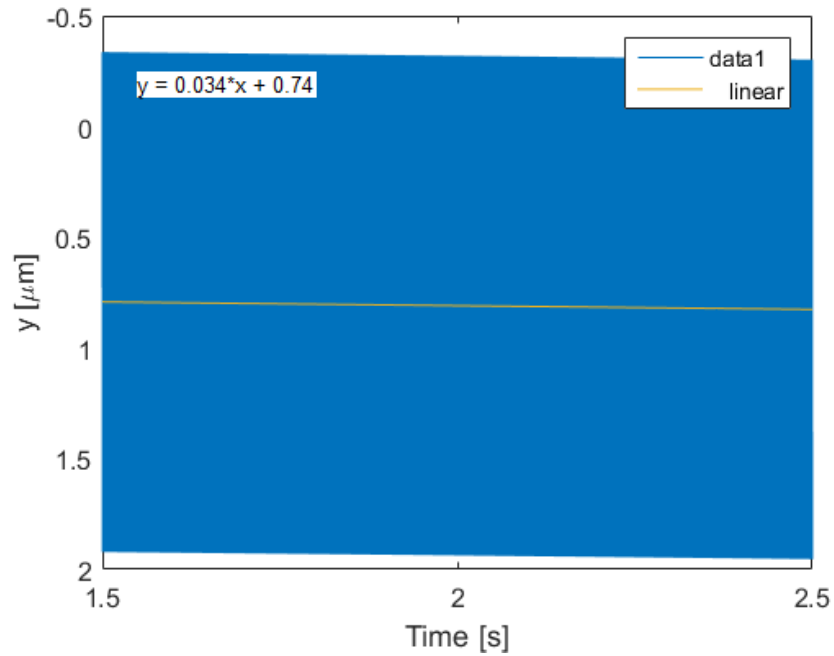
Figure 3.160: WFXLMS test 13: linear trend line for *y*-axis at bearing B.

While increasing the supply current did decrease the rate that the rotor drifts away from the bearing center to about 0.08 $\mu m/s$, it is still greater than was achieved with test 11, and test 11 used significantly less current. This indicates that the parameters used in test 11 could be the optimal configuration for this controller.

3.3.14   Test 14

The flywheel parameters used for this test are listed in Table 3.41. From these testing conditions, the average and maximum values for the current and position in Table 3.42 were determined.

The time domain response of the FES system at the three bearings are shown in Figures 3.161 through 3.163.

An instantaneous frequency (IF) plot of each temporal response was generated to

Table 3.41: WFXLMS test 14 conditions.

| Term	Value	Units
ω	200000	rpm
	3333	Hz
dt	1×10^{-5}	s
I_{0r}	4	A
I_{0z}	4	A
i_{supply}	100	A
$i_{supplyz}$	100	A
N	128	
eG	1	
eGz	1	
W1	0.5	
W1z	0.5	
μ_1	1×10^{-4}	
μ_2	1×10^{-4}	
μ_{1z}	1×10^{-4}	
μ_{2z}	1×10^{-4}	
t_{end}	2.5	

Figure 3.161: WFXLMS test 14: independent bearing A temporal responses.

Table 3.42: WFXLMS test 14 results.

Term	Axis	Average	Maximum
Current (A)	x	2.76×10^{-1}	2.64×10^{0}
	y	4.31×10^{-1}	2.97×10^{0}
	z	1.47×10^{-1}	4.00×10^{0}
Magnitude (m)	x	1.58×10^{-6}	1.51×10^{-5}
	y	2.50×10^{-6}	1.70×10^{-5}
	z	1.05×10^{-6}	2.87×10^{-5}
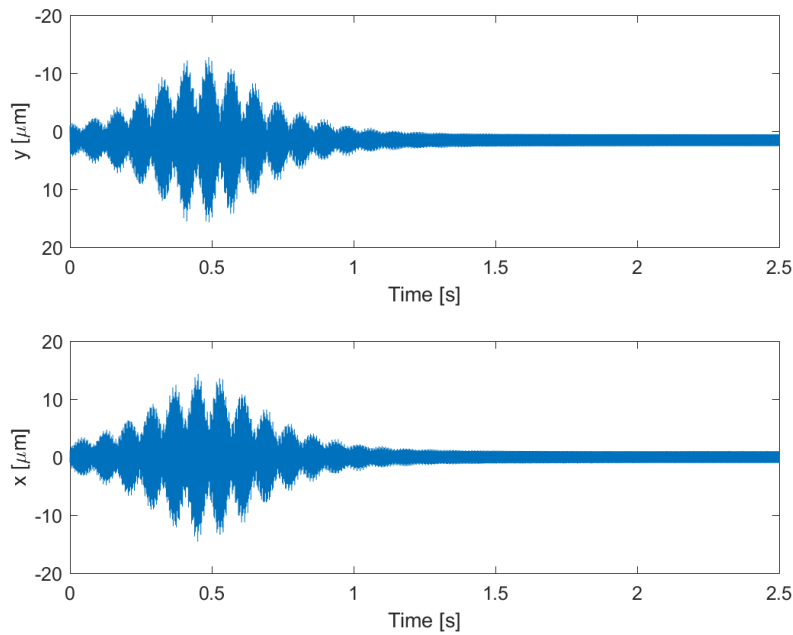
Figure 3.162: WFXLMS test 14: independent bearing B temporal responses.

evaluate the stability in the frequency domain and is shown in Figures 3.164 through 3.168.
The raw data generated for each bearing had significant signal processing noise due to the
nature of the IF calculations process. Therefore, a smoothing function was applied to this
data to reveal the frequency trends and omit unnecessary data outliers. When comparing
the raw plot with the smoothed plot, there was not a noticeable difference in the general
trend of the data. Therefore, it is reasonable to assume that these plots do an adequate job
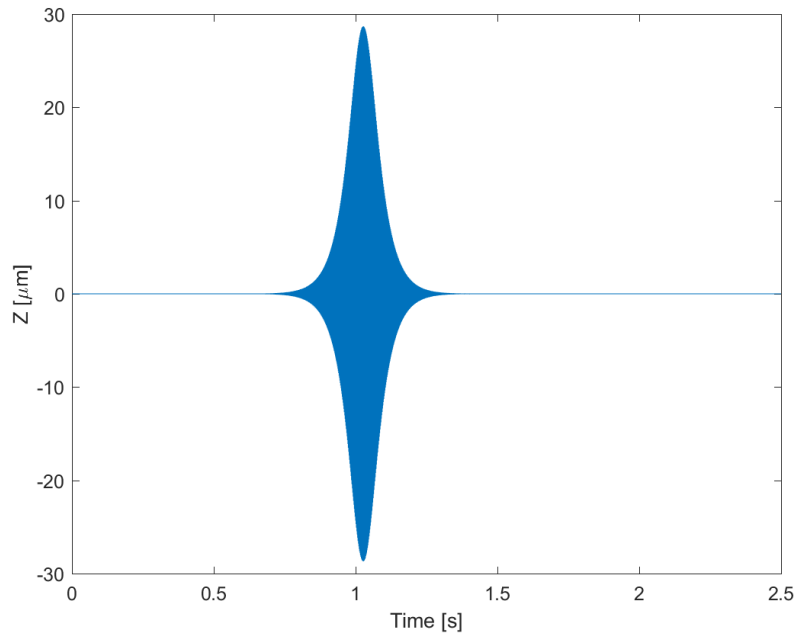
Figure 3.163: WFXLMS test 14: thrust bearing.

depicting the controller's stability in the frequency domain.

While this data looks like it converged, a linear trend line from 1.5 seconds to the end of the simulation was created for the *y*-axis at bearing A and B to quantify the drift away from 0 and is shown in Figures 3.169 and 3.170.

This test is really important because it took the ideal parameters established in test 11 and applied them to an identical system operating at 200,000 rpm. The dynamic behavior of this system in the time domain (Figures 3.161 through 3.163) follows a similar trend as seen in test 11. The *x*- and *y*-axis diverged for the first half a second before converging, but this time the low frequency oscillations are more prominent. Again, the *z*-axis diverged for the first second before returning to 0. Overall, the maximum displacement increased by about 2 μm and the average displacement increased by about 0.1 μm when compared
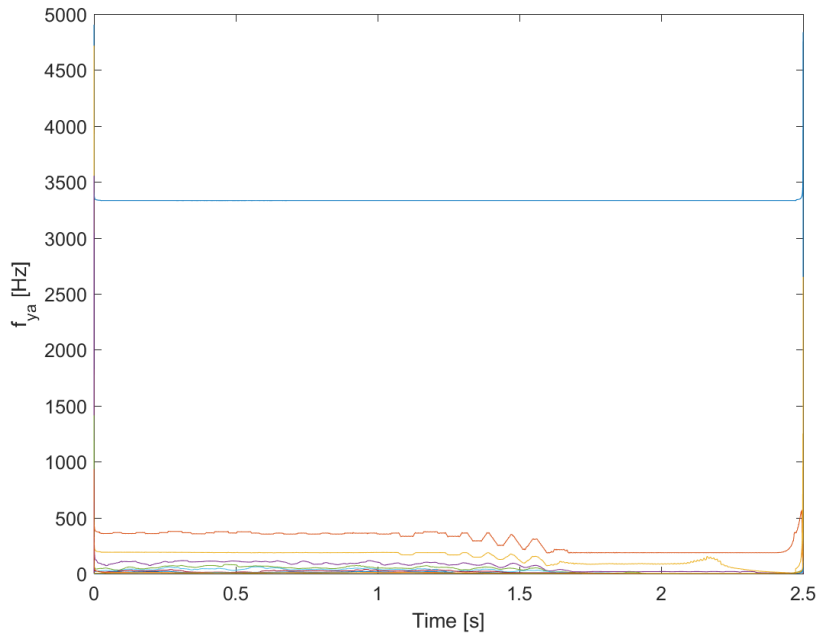
Figure 3.164: WFXLMS test 14: bearing A IF response for *y*-axis.
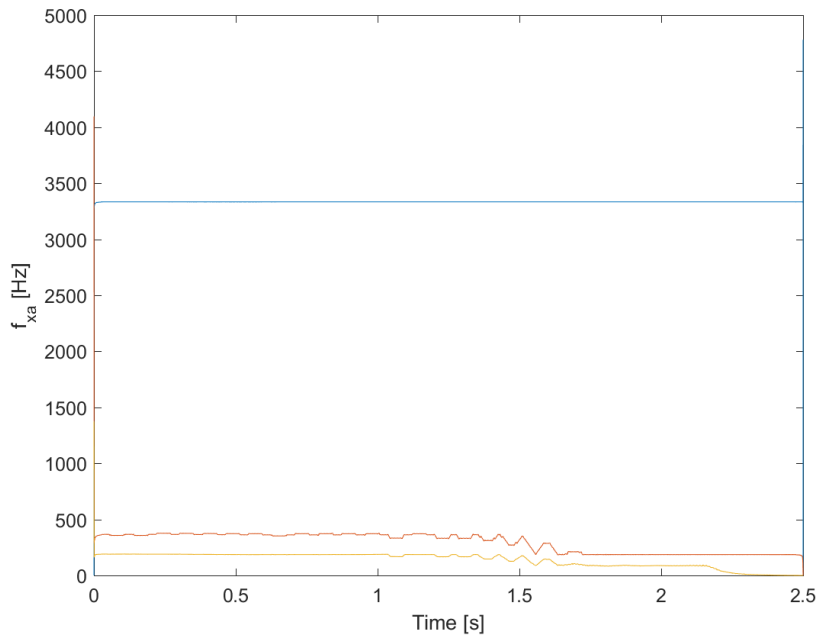
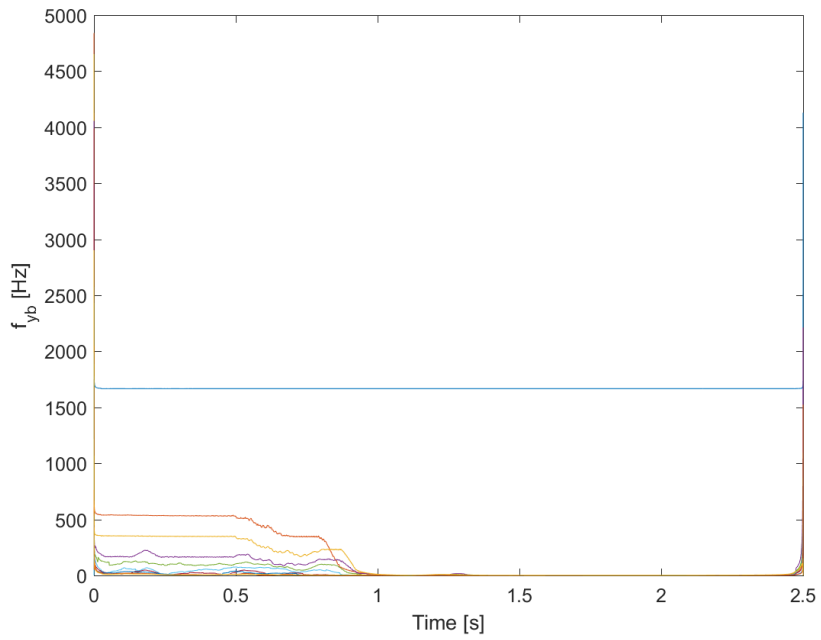Figure 3.165: WFXLMS test 14: bearing A IF response for *x*-axis.
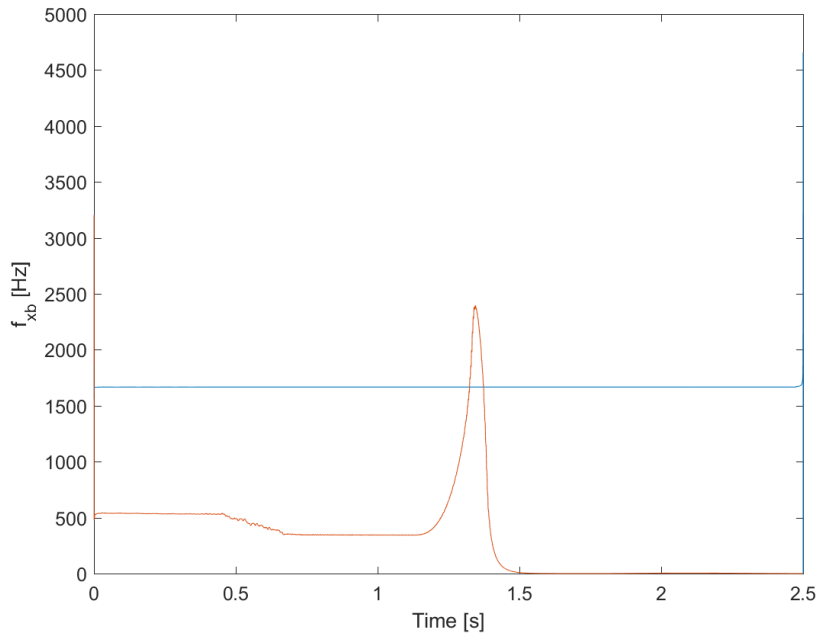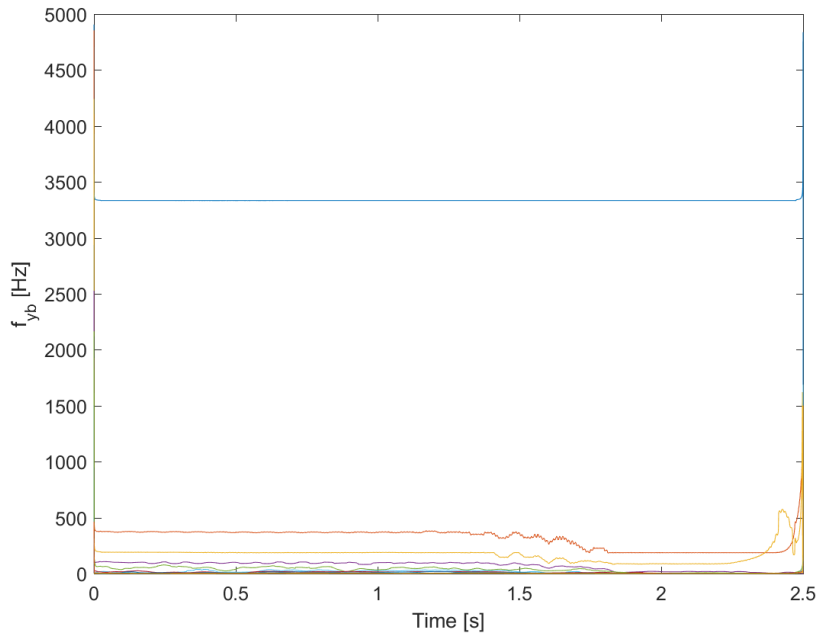
Figure 3.166: WFXLMS test 14: bearing B IF response for *y*-axis.

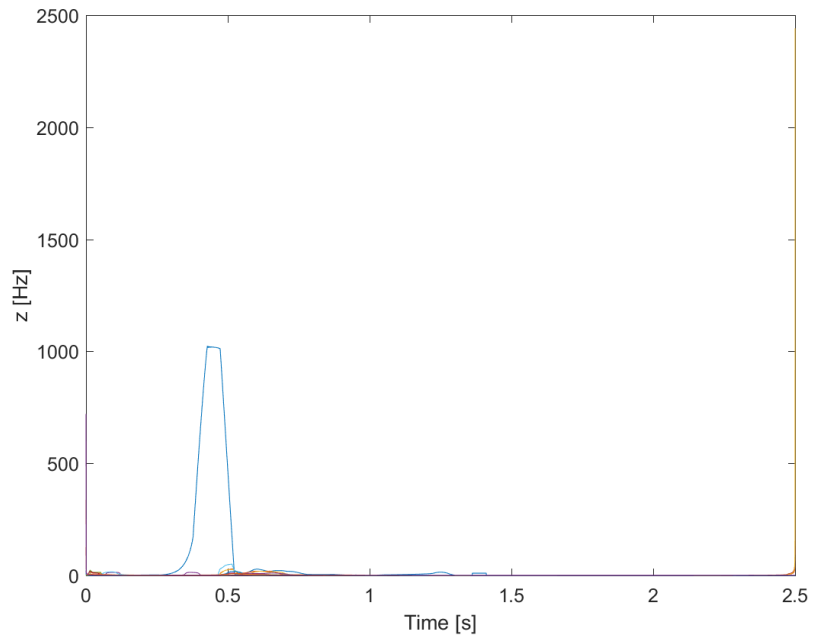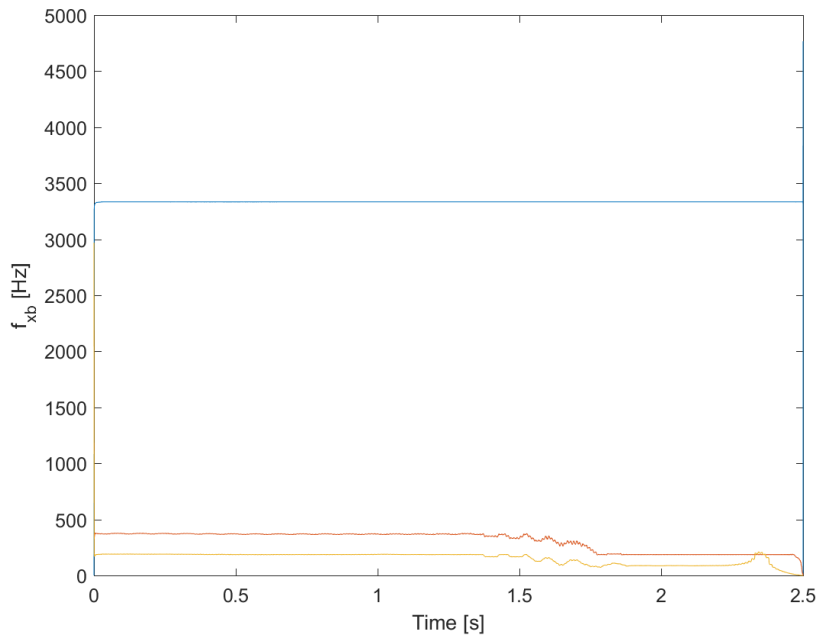Figure 3.167: WFXLMS test 14: bearing B IF response for *x*-axis.
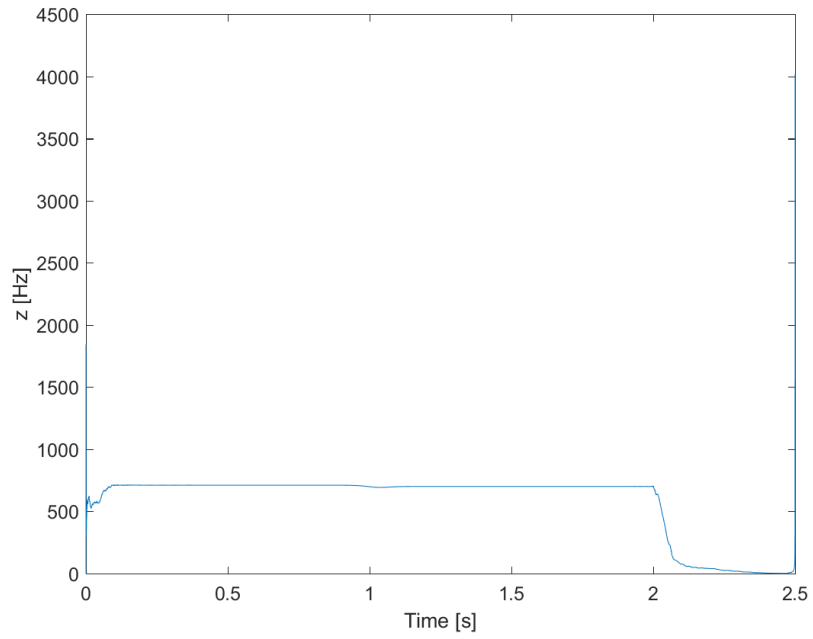
Figure 3.168: WFXLMS test 14: thrust bearing IF response.
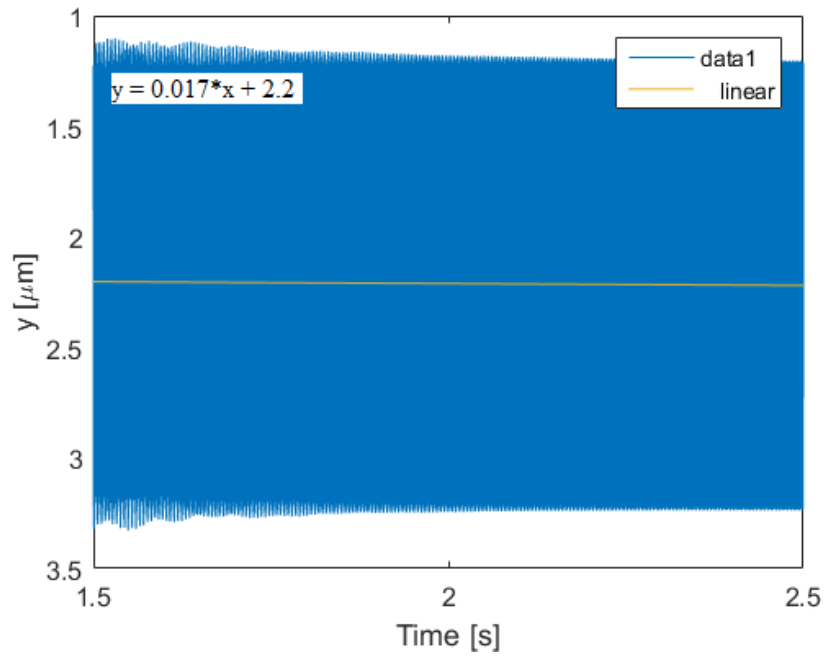
Figure 3.169: WFXLMS test 14: linear trend line for *y*-axis at bearing A.
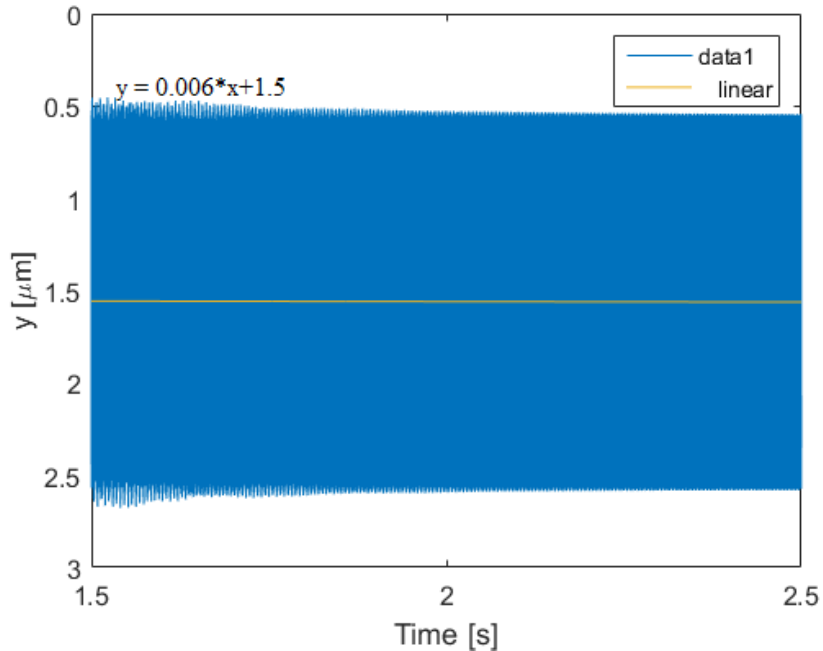
Figure 3.170: WFXLMS test 14: linear trend line for *y*-axis at bearing B.

with test 11. These small increases in amplitude are still well within the clearance gaps. In addition, the average drift away from 0 is less than in test 11 at 0.017 $\mu m/s$ (Figure 3.169).

In a similar manner, the average current increased from test 11 by about 0.02 Amps and the maximum current increased by 0.3 Amps. A steady state value of 0.4 Amps is still less than the fuzzy-logic or PID controllers at 100,000 and 200,000 rpm. This is a notable advantage for this controller over the others.

The IF plots (Figures 3.164 through 3.168) again depict steady control in the frequency domain. In fact, the frequency domain responses almost match test 11 exactly. This implies that the controller does not have any difficulty establishing a predictable flywheel response. Even the *z*-axis shows a single mode that is eventually reduced to 0. Clearly, this controller has no problem operating the FES system at 200,000 rpm.

3.4 Controller Comparison

The preceding WFXLMS optimization method is not necessarily complete but it is, however, relatively comprehensive. With this in mind, the ideal FES system response was created in test 11. The maximum drift away from 0 after the controller reached steady state in the frequency domain was about 0.023 $\mu m/s$ which can be treated as approximately 0. In addition, the frequency domain is steady throughout the entire simulation and even manages to completely eliminate oscillation in the z-axis after about 2 seconds. To get a better feel for how this controller compares to the PID and fuzzy-logic controllers at 100,000 rpm, the key data from the previous sections are compiled in Table 3.43.

Table 3.43: Controller comparison at 100,000 rpm.

Parameter	Axis	WFXLMS	PID	Fuzzy-Logic
Mean Current (A)	x	2.56×10^{-1}	6.79×10^{-1}	8.41×10^{-1}
	y	4.12×10^{-1}	6.89×10^{-1}	8.37×10^{-1}
	z	1.47×10^{-1}	2.54×10^{-9}	2.16×10^{-3}
Max Current (A)	x	2.29×10^{0}	1.80×10^{0}	1.92×10^{0}
	y	2.69×10^{0}	1.63×10^{0}	2.32×10^{0}
	z	4.00×10^{0}	1.41×10^{-8}	6.41×10^{-2}
Mean Magnitude (m)	x	1.46×10^{-6}	9.89×10^{-7}	4.13×10^{-7}
	y	2.39×10^{-6}	9.95×10^{-7}	4.15×10^{-7}
	z	1.05×10^{-6}	3.70×10^{-15}	2.68×10^{-7}
Max Magnitude (m)	x	1.32×10^{-5}	2.75×10^{-6}	1.07×10^{-6}
	y	1.54×10^{-5}	2.51×10^{-6}	1.49×10^{-6}
	z	2.87×10^{-5}	2.07×10^{-14}	2.68×10^{-7}

While the WFXLMS controller has the largest absolute maximum current draw, it still manages to run with a significantly smaller average value. In fact, the WFXLMS

162

controller runs with about half the average current draw compared to the PID and nearly a quarter of the fuzzy-logic controller. Comparing the average current draw in the z-axis can be a little misleading simply because the controller had a much larger absolute maximum value which increases the average. At the end of the WFXLMS simulation, the controller was only pulling about 4.13×10^{-6} Amps in the z-axis which is much less than the fuzzy-logic controller but much larger than the PID. This is really important for FES systems since active power consumption is the limiting factor when considering the length of time that energy can be stored. Consequently, if the ultimate design goal of a FES system is to increase energy storage duration, the WFXLMS controller is the best option.

Looking at the displacements for each controller is a different story. The WFXLMS controller had much larger average displacements than the other two controllers. While this may be worse for systems where the clearance gap is much smaller, recall that this system had a clearance gap of 400 μm for the journal bearings and 500 μm for the thrust bearing; much larger than the average and maximum displacements for all of the controllers. Therefore, all three of these controllers performed adequately in the time domain, but, if the maximum allowable displacement of the rotor is the most important design parameter, the best choice is the fuzzy-logic controller.

The time domain response for each of these controllers is unique. The PID controller (Figures 3.1 through 3.3) takes from 1 to 1.5 seconds to respond and achieve steady state in the y- and z-axis but it converges almost immediately in the x-aixs. The fuzzy-logic controller (Figures 3.27 through 3.29) reached steady state in all axis immediately, or at the

very least, the maximum amplitude of vibration never exceeded the initial values. Finally, the WFXLMS controller (Figures 3.131 through 3.133) took about the same time as the PID controller to reach steady state, but it displayed divergence in the *x*- and *y*-axis for the first 0.5 seconds and for about 1 second in the *z*-axis before converging. This diverging behavior subsequently generated the largest magnitude displacement of all the controllers and, consequently, it requires the largest clearance gap when it is designed. Again, the controller that did the best job in the time domain was the fuzzy-logic controller, but the PID controller actually did the best job controlling the thrust bearing by limiting its maximum displacement to 2×10^{-14} meters.

Finally, looking at the difference between the controllers in the frequency domain shows that the PID controller (Figures 3.4 through 3.8) completely eliminated all modes of vibration (besides the eccentric force) after about 0.25 seconds. A little bit of overshoot is detected in the thrust bearing, but it is well within the acceptable range. The fuzzy-logic controller (Figures 3.30 through 3.34) did not display any control for the duration of the test. This is where the fuzzy-logic controller could become a problem. If the frequency domain is not stable then it is possible that any number of natural vibration modes of a flexible rotor could be excited at any time and lead to sudden system failure. The WFXLMS controller (Figures 3.134 through 3.138) was very stable in the frequency domain. In fact, looking at all of the tests done in this chapter shows that this controller is capable of achieving steady and robust control of the system in the frequency domain regardless of controller or simulation parameters. This is definitely a strength of this controller. The ultimate

comparison, however, is at 200,000 rpm in Table 3.44.

Table 3.44: Controller comparison at 200,000 rpm.

Parameter	Axis	WFXLMS	PID	Fuzzy-Logic
Mean Current (A)	x	2.76×10^{-1}	4.8×10^{-1}	1.77×10^{0}
	y	4.31×10^{-1}	4.93×10^{-1}	1.84×10^{0}
	z	1.47×10^{-1}	6.79×10^{-11}	2.16×10^{-3}
Max Current (A)	x	2.64×10^{0}	1.01×10^{0}	2.55×10^{0}
	y	2.97×10^{0}	1.10×10^{0}	3.05×10^{0}
	z	4.00×10^{0}	8.17×10^{-10}	6.41×10^{-2}
Mean Magnitude (m)	x	1.58×10^{-6}	6.99×10^{-7}	6.61×10^{-7}
	y	2.50×10^{-6}	7.07×10^{-7}	1.14×10^{-6}
	z	1.05×10^{-6}	1.65×10^{-16}	2.68×10^{-7}
Max Magnitude (m)	x	1.51×10^{-5}	1.48×10^{-6}	1.39×10^{-6}
	y	1.70×10^{-5}	1.77×10^{-6}	2.63×10^{-6}
	z	2.87×10^{-5}	1.42×10^{-15}	2.69×10^{-7}

All three controllers had a similar dynamic response in the time domain for both the 100,000 and 200,000 rpm tests, but all of the magnitudes were exaggerated slightly. Again, the WFXLMS controller used less current than the other controllers except for the z-axis, but by the end of the simulation, the WFXLMS controller was only using an average of 7.31×10^{-6} Amps for the last second of the simulation and 2.02×10^{-9} Amps for the last 0.5 seconds; indicating that the average current draw is decreasing with time and approaching the same level as the PID controller.

Where the WFXLMS controller really shines again is in the IF response of the z-axis. The WFXLMS controller shows a singular frequency for a majority of the test, but eventually even reduces that mode to 0. This means that the controller stopped the z-

axis from moving. Both the fuzzy-logic and the PID controllers showed instability in the frequency domain. The fuzzy-logic had many modes that changed randomly between 0 and 500 Hz while the PID was worse. The PID controller did manage to eliminate some of the modes, but one mode drifted from 0 to 4,250 Hz for the entire simulation and seemed to have no periodicity. Simply comparing these responses demonstrates the more robust control created by the WFXLMS controller.

Considering the previous discussion, the WFXLMS controller is the best choice for a FES system if it needs to maintain its charge for a long duration. Clearly, the WFXLMS creates an environment where the dynamics are predictable since the frequency domain response is well controlled, but where the WFXLMS struggles when compared to the other controllers is in the time domain; specifically the amplitude of vibration. If the amplitude of vibration is a major design concern, the best solution is the PID controller, but for all other cases, the WFXLMS controller provides the ideal, low-power control for a FES system.

4   CONCLUSIONS AND FUTURE WORK

It appears that the PID and fuzzy-logic controllers both successfully controlled the FES system when operating at 100,000 rpm. However, since an important criteria for dynamic stability is fixed or predictable modes in the frequency domain, both of these controller should be considered unstable. This unstable frequency response requires erratic current from the controller with power spikes that could damage a real system. In contrast, the WFXLMS controller demonstrated stability and adaptability in the frequency domain; regardless of controller parameters. Parameter tuning to improve the response in the time domain revealed how complicated the relationships between controller parameters are. In other words, changing system parameters could result in drastically different converging and steady state behavior.

A lack of any mathematical model to determine the ideal controller parameters was a major issue because the only way to see if the controller works was to guess using a trial-and-error method with a little bit of intuition. Knowing how this controller worked did help with honing in on parameters, but finding the ideal combination relied almost entirely on luck. Changing certain parameters lead to results that conflicted with intuition and is likely due to system bifurcation. More research needs to be conducted to investigate the impact that these controller parameters have on system dynamics including how filter length, filter weights, the level of wavelet decomposition, and the selection of the reference signal all impact the performance of the controller. An ideal result from this research would be a

method for tuning the controller parameters.

Despite the lack of a controller tuning methodology, an ideal set of controller parameters was identified for 100,000 rpm in test 11 where the rate of drifting in the *y*-axis was limited to about 0.02 $\mu m/s$. This drifting primarily indicates the slow reaction that this controller has to a continuous force when it is simultaneously tuned to control a high-frequency input such as eccentricity. The contrast between the steady force of gravity and the periodic eccentric force play vastly different roles in the frequency domain and it is likely that this controller would eventually return the rotor to the origin and achieve 0 drifting provided a longer simulation time.

Comparing all of the results shows that the ideal controller for a FES system is WFXLMS; especially at 200,000 rpm. While it did draw the largest maximum current of any system, it used significantly less (half of PID and a quarter of fuzzy-logic's) steady state current, while also maintaining stability in the frequency domain. This would drastically improve the time that the controller could store energy; one of the main functions of a FES system. Comparing the average displacements shows that the WFXLMS controller had the loosest bounds (particularly in the *z*-axis), but the WFXLMS controller only used a fraction of the available clearance gap, and was still converging at the end of the simulation. If the FES system was used in an environment like space or a wind-farm where external excitations are limited, the WFXLMS controller is the clear choice. However, if external excitations are a real concern, the PID and fuzzy-logic controller demonstrated a much quicker reaction time and could be a better option; provided they ran at lower speeds.

In the future, research should be conducted where the FES system is controlled with a combination of a fuzzy-logic and WFXLMS controller. The fuzzy-logic controller had the best reaction time in the time domain, but demonstrated poor stability in the frequency domain. The frequency domain stability that the WFXLMS controller demonstrated could make the time domain response more predictable without sacrificing the fast reaction time of the fuzzy-logic controller.

This research should also be extended by conducting long-term simulations of the FES system. Simulations for a couple of minutes should include periodic impulse forces and examine the stability and power-draw over time. In particular, one of the major causes of FES system failure is Hopf bifurcation when the operating speed is variable. In essence, the behavior of the FES system is far less predictable when the frequency of the rotor changes and would challenge each of these controllers much more than they already have been.

REFERENCES

[1] C. D. Hall, "Integrated spacecraft power and attitude control systems using fly-wheels," *Airforce Institute of Technology, Tech. Rep. AFIT/ENY/TR-000*, 2000.

[2] M. Krack, M. Secanell, and P. Mertiny, *Energy Storage in the Emerging Era of Smart Grids*. InTech, 2011.

[3] M. Pichot, J. Kajs, B. Murphy, A. Ouroua, B. Rech, R. Hayes, J. Beno, G. Buckner, and A. Palazzolo, "Active magnetic bearings for energy storage systems for combat vehicles," *Magnetics, IEEE Transactions on*, vol. 37, no. 1, pp. 318–323, 2001.

[4] B. H. Kenny, P. E. Kascak, R. Jansen, T. Dever, and W. Santiago, "Control of a high-speed flywheel system for energy storage in space applications," *Industry Applications, IEEE Transactions on*, vol. 41, no. 4, pp. 1029–1038, 2005.

[5] K. Youcef-Toumi and S. Reddy, "Dynamic analysis and control of high speed and high precision active magnetic bearings," *Journal of Dynamic Systems, Measurement, and Control*, vol. 114, no. 4, pp. 623–633, 1992.

[6] A. M. Mohamed and F. P. Emad, "Nonlinear oscillations in magnetic bearing systems," *Decision and Control, 1989., Proceedings of the 28th IEEE Conference on*, pp. 548–553, 1989.

[7] L. N. Virgin, T. F. Walsh, and J. D. Knight, "Nonlinear behavior of a magnetic bearing system," *ASME Journal of Engineering for Gas Turbines and Power*, vol. 117, no. 3, pp. 582–588, 1995.

[8] U. Floegel-Delor, R. Rothfeld, D. Wippich, B. Goebel, T. Riedel, and F. N. Werfel, "Fabrication of hts bearings with ton load performance," *Applied Superconductivity, IEEE Transactions on*, vol. 17, no. 2, pp. 2142–2145, 2007.

[9] A. Charara, J. De Miras, and B. Caron, "Nonlinear control of a magnetic levitation system without premagnetization," *Control Systems Technology, IEEE Transactions on*, vol. 4, no. 5, pp. 513–523, 1996.

[10] B. C. Wilson, P. Tsiotras, and B. Heck-Ferri, "Control designs for low-loss active magnetic bearings," *Advanced Intelligent Mechatronics. Proceedings, 2005 IEEE/ASME International Conference on*, pp. 1097–1102, 2005.

[11] M. Chinta, *Steady State Nonlinear Rotordynamics and Modeling of Magnetic Bearings*. Ph.D. dissertation, Texas A&M University, College Station, December 1997.

[12] M. S. Sarma and A. Yamamura, "Nonlinear analysis of magnetic bearings for space technology," *Aerospace and Electronic Systems, IEEE Transactions on*, vol. AES-15, no. 1, pp. 134–140, 1979.

[13] H. Underbakke, "Operational experience with the world□s first offshore turboexpanders with magnetic bearings," *ASME 1996 International Gas Turbine and Aeroengine Congress and Exhibition*, vol. 117, no. 3, pp. 582–588, 1996.

[14] J. Fang, L. Lin, L. Yan, and L. Xiao, "A new flywheel energy storage system using hybrid superconducting magnetic bearings," *Applied Superconductivity, IEEE Transactions on*, vol. 11, no. 1, pp. 1657–1660, 2001.

[15] M. Liu, "Investigation on the applicability of active magnetic bearings to high speed spindle design," M.S. thesis, Texas A&M University, College Station, 2015.

[16] Y. Ho, H. Liu, and L. Yu, "Stability and bifurcation of a rigid rotor-magnetic bearing system equipped with a thrust magnetic bearing," *Proceedings of the Institution of Mechanical Engineers, Part J: Journal of Engineering Tribology*, vol. 215, no. 5, pp. 457–470, 2001.

[17] P. K. Agarwal and S. Chand, "Fuzzy logic control of four-pole active magnetic bearing system," *Modelling, Identification and Control (ICMIC), The 2010 International Conference on*, pp. 533–538, 2010.

APPENDIX A

SIMULINK MODELS

The figures in this chapter show the SIMULINK model configuration for the WFXLMS, PID, and fuzzy-logic controllers.
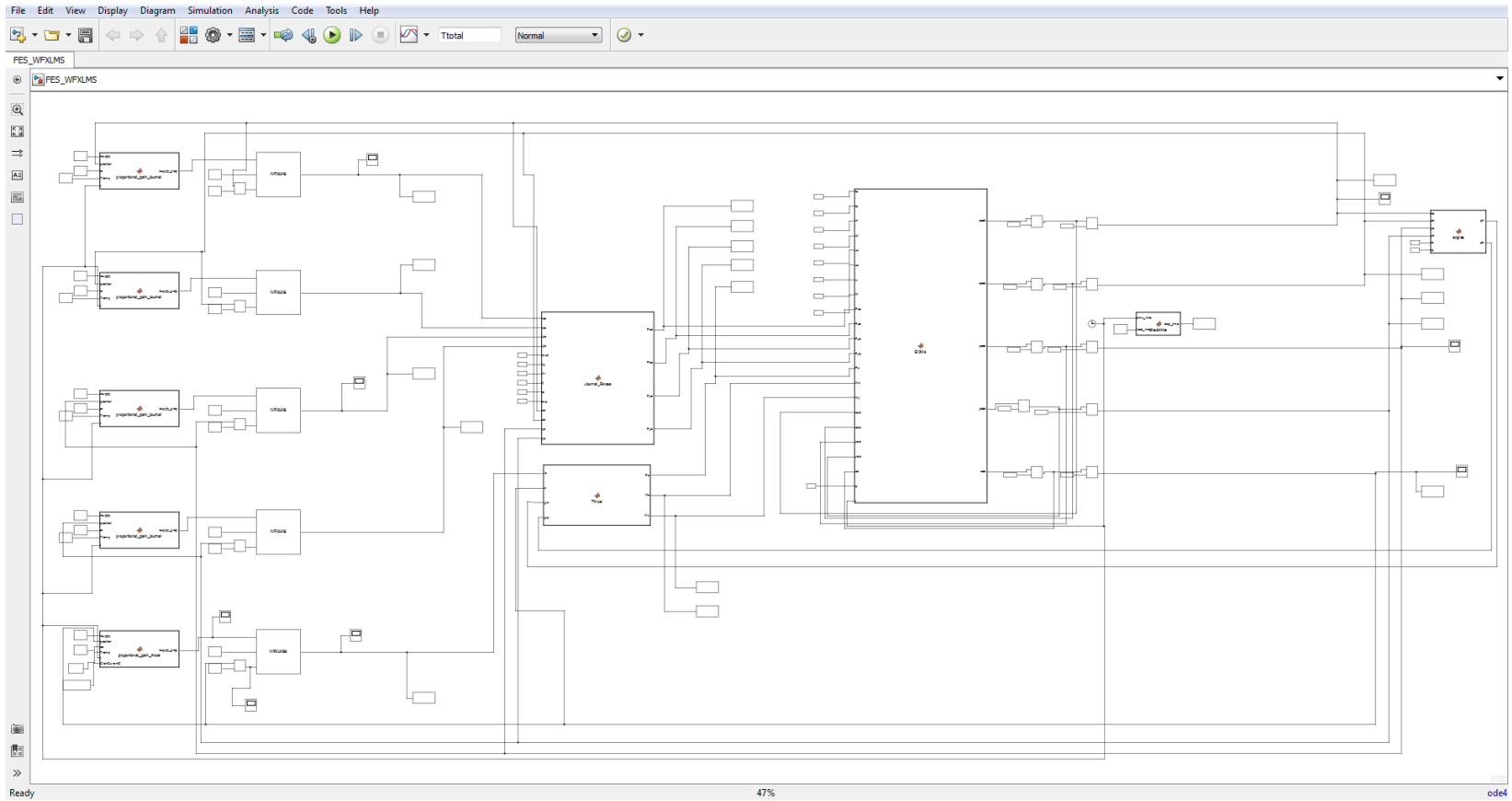
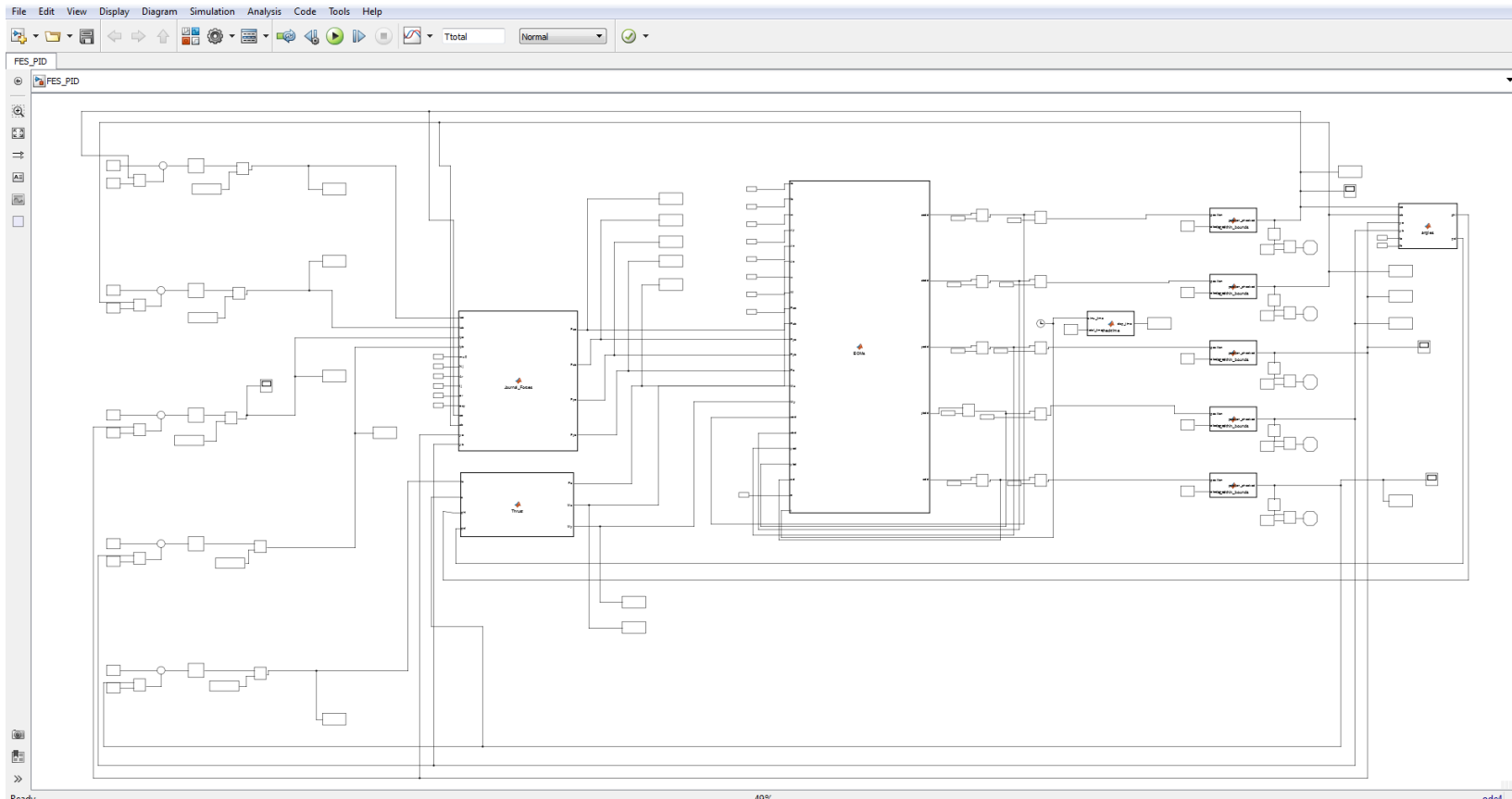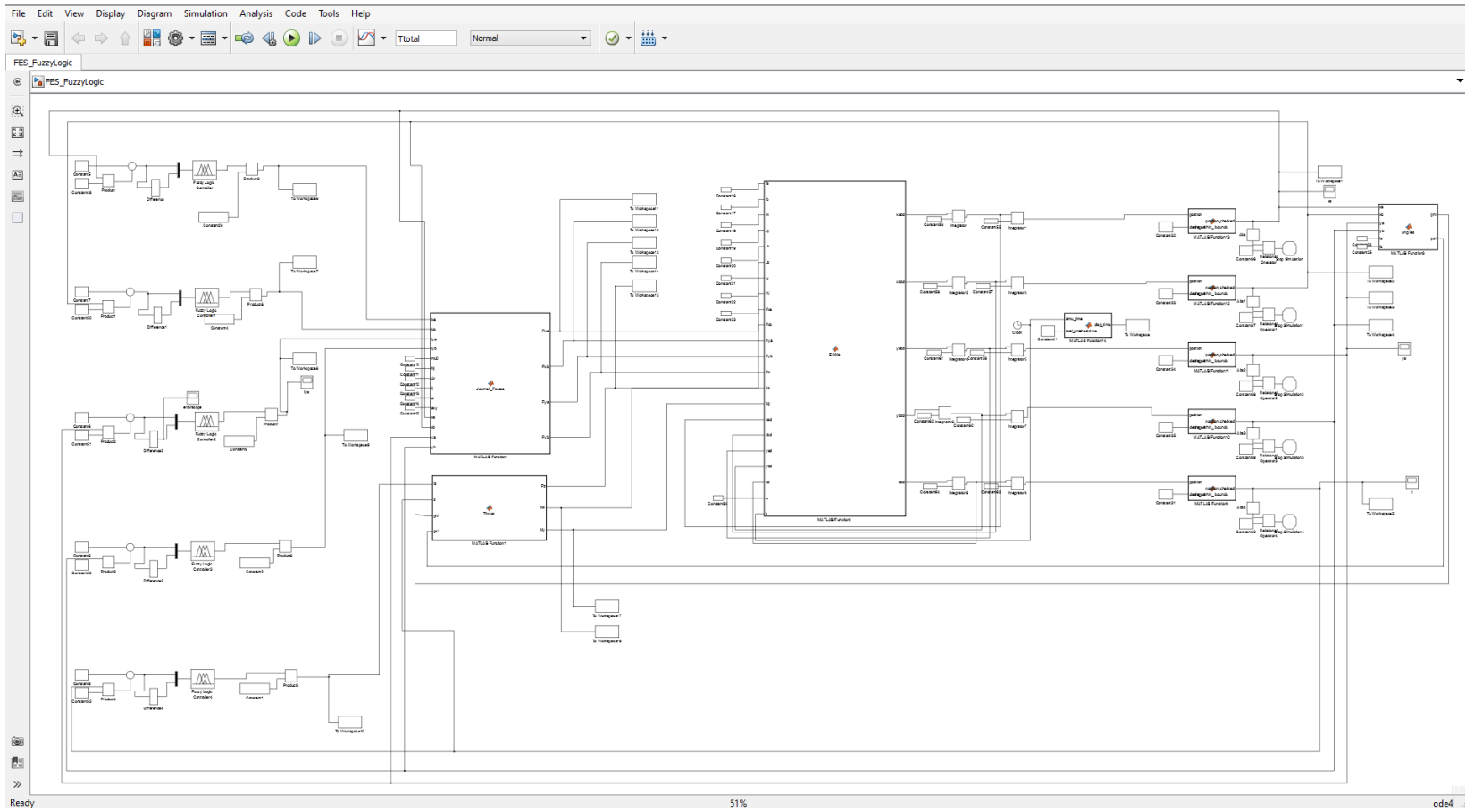Figure A.1: SIMULINK layout for WFXLMS controller.

Figure A.2: SIMULINK layout for PID controller.

Figure A.3: SIMULINK layout for FL controller.